SPECTROSCOPIC INVESTIGATIONS OF SURFACE-LIGAND BINDING DURING PEROVSKITE NANOCRYSTAL GROWTH

by

JAMES CHRISTOPHER SADIGHIAN

A DISSERTATION

Presented to the Department of Chemistry and Biochemistry
and the Division of Graduate Studies of the University of Oregon
in partial fulfillment of the requirements
for the degree of
Doctor of Philosophy

December 2021

DISSERTATION APPROVAL PAGE

Student: James Christopher Sadighian

Title: Spectroscopic Investigations of Surface-Ligand Binding During Perovskite Nanocrystal Growth

This dissertation has been accepted and approved in partial fulfillment of the requirements for the Doctor of Philosophy degree in the Department of Chemistry and Biochemistry by:

James S. Prell	Chair
Cathy Y. Wong	Advisor
Marina G. Guenza	Core Member
Benjamín J. Aleman	Institutional Representative

and

Krista Chronister	Vice Provost of Graduate Studies

Original approval signatures are on file with the University of Oregon Division of Graduate Studies.

Degree awarded December 2021

DISSERTATION ABSTRACT

James Christopher Sadighian

Doctor of Philosophy

Department of Chemistry and Biochemistry

December 2021

Title: Spectroscopic Investigations of Surface-Ligand Binding During Perovskite Nanocrystal Growth

Lead halide perovskite nanocrystals (NCs) are promising materials for a range of photovoltaic and optoelectronic applications due to their favorable properties and potential for low-cost, solution-based processing. The model of nucleation and growth proposed by Victor LaMer that is typically used to describe colloidal NC synthesis has guided our understanding of NC formation for over 70 years. However, LaMer's model does not account for the effects of surface-ligand interactions on the availability of precursor, the resulting burst nucleation, or the growth of the NC. The large surface-area-to-volume ratio means that NC properties are heavily influenced by the surface. Thus, accurate characterization of surface-ligand interactions is critical to better understand the mechanisms by which these nanocrystals nucleate and grow and how their electronic structure evolves during these processes so that better materials may be made through rational design. Photophysical characterization that can probe the electronic structure and dynamics of a material is typically limited to structurally stable NCs owing to the long timescales required, preventing the accurate measurement of NCs during growth. This is a particular challenge for non-linear spectroscopies such as transient absorption. Here we report on work done to spectroscopically investigate nucleation

and growth of methylammonium lead triiodide ($MAPbI_3$) perovskite nanocrystals to better understand the role of surface ligands. $MAPbI_3$ NCs are grown via a novel synthesis where reaction kinetics are mediated by the solubility of the solid precursors in a non-polar solvent. Use of a novel single-shot transient absorption spectrometer reveals that photogenerated charge carriers become localized at surface trap states during NC growth, producing a TA lineshape characteristic of the Stark effect. Observation of this Stark signal shows that the contribution of trapped carriers to the TA signal declines as growth continues, supporting a growth mechanism characterized by increased surface ligation toward the end of NC growth. This work opens the door to the application of time-resolved spectroscopies to NCs in situ during their synthesis, providing greater insight into their growth mechanisms and the evolution of their photophysical properties.

CURRICULUM VITAE

NAME OF AUTHOR: James Christopher Sadighian

GRADUATE AND UNDERGRADUATE SCHOOLS ATTENDED:

University of Oregon, Eugene, OR
George Mason University, Fairfax, VA

DEGREES AWARDED:

Doctor of Philosophy, Chemistry, 2021, University of Oregon
Master of Science, Chemistry, 2015, George Mason University
Bachelor of Science, Biochemistry, 2012, George Mason University

AREAS OF SPECIAL INTEREST:

Quantum-Confined Perovskites
Ultrafast Spectroscopy
Nucleation and Growth of Colloidal Nanoparticles

PROFESSIONAL EXPERIENCE:

Graduate Research Fellow, University of Oregon, 2016-present

Graduate Teaching Fellow, University of Oregon, 2015-present

Technical Intern, Noblis, 2015

Graduate Teaching Assistant, George Mason University, 2013, 2015

Graduate Research Assistant, George Mason University, 2014

Chemistry Stockroom Manager, George Mason University, 2014

GRANTS, AWARDS AND HONORS:

Graduate Student Award for Excellence in the Teaching of Chemistry, University of Oregon, AY2020-2021

Graduate Student Award for Excellence in the Teaching of Chemistry, University of Oregon, AY2018-2019

PUBLICATIONS:

Sadighian, J. C.; Wong, C. Y. Just scratching the surface: In situ and surface-specific characterization of perovskite nanocrystal growth. *Journal of Physical Chemistry C* **2021**, *125*, 20772-20782. [ACS Editors' Choice]

Hassan, Y.; Park, J. H.; Crawford, M. L.; Sadhanala, A.; Sadighian, J. C.; Mosconi, E.; Shivanna, R.; Jeong, M.; Yang, C.; Lee, J.; Choi, H.; Park, S. H.; Song, M. H.; De Angelis, F.; Wong, C. Y.; Friend, R. H.; Lee, B. R.; and Snaith, H. J. Ligand-engineered bandgap stability in mixed-halide perovskite LEDs. *Nature* **2021**, *591*, 72–77

Sadighian, J. C.; Wilson, K. S.; Crawford, M. L.; Wong, C. Y. Single-Shot Transient Absorption of Nascent Perovskite Nanocrystals. *The 22nd International Conference on Ultrafast Phenomena 2020* **2020**, Tu3A.6

Sadighian, J. C.; Wilson, K. S.; Crawford, M. L.; Wong, C. Y. Evolving Stark Effect During Growth of Perovskite Nanocrystals Measured Using Transient Absorption. *Frontiers in Chemistry* **2020**, *8*, 897.

Sadighian, J. C.; Wilson, K. S.; Crawford, M. L.; Wong, C. Y. Understanding perovskite nanocrystal growth using in situ transient absorption spectroscopy. *Proc. SPIE 11464* **2020**, *Physical Chemistry of Semiconductor Materials and Interfaces XIX*, 114640K.

Crawford, M. L.; Sadighian, J. C.; Hassan, Y.; Snaith, H. J.; Wong, C. Y. Spectral shifts upon halide segregation in perovskite nanocrystals observed via transient absorption spectroscopy. *MRS Advances* **2020**, *5*, 2613-2621.

Sadighian, J. C.; Crawford, M. L.; Suder, T. W.; Wong, C. Y. Surface ligation stage revealed through polarity-dependent fluorescence during perovskite nanocrystal growth. *Journal of Materials Chemistry C* **2020**, *8*, 7041–7050.

Sadighian, J. C.; Crawford, M. L.; Wong, C. Y. In situ transient absorption spectroscopy of organometal halide perovskite nanoparticles. *Contributed Papers from Materials Science I& Technology 2019* **2019** 960-963.

Sadighian, J. C.; Crawford, M. L.; Wong, C. Y. Rapid sampling during synthesis of lead halide perovskite nanocrystals for spectroscopic measurement. *MRS Advances* **2019**, *4*, 1957–1964.

Arya G.; Tadayon S.; Sadighian J.; Jones J.; de Mutsert K.; Huff T. B.; Foster, G. D. Pharmaceutical chemicals, steroids and xenoestrogens in water, sediments and fish from the tidal freshwater Potomac River (Virginia, USA). *Journal Environmental Science I& Health A* **2017**, *52*, 686-696.

ACKNOWLEDGEMENTS

First, I must thank my advisor, Cathy Wong, for her endless patience and unwavering optimistic outlook, even when faced with years of my unrelenting pessimism. I am eternally grateful for accepting me into her research group early in her career. She taught me how to think about and solve scientific problems, how to communicate science effectively, and how to stay positive as failed experiments pile up like tribbles. If I become a fraction of the scientist, and mentor, that she is then I will consider my time at Oregon a massive success.

To everyone in the Wong/Prell office for all the laughs, coffee breaks, and general camaraderie. You all made the long days and longer nights far more tolerable.

To the friends I made in Eugene, you all managed to make six and a half years of graduate school not just bearable, but outright enjoyable. From summer camping trips and Ems games to fall football tailgates and rainy winters spent indoors just trying to stay dry, it has been one of the greatest pleasures of my life knowing you all and being a part of your lives.

To my wife, Angela, who uprooted her life and moved across the country with me, I will spend the rest of my life trying to repay the support you have given me these past few years. I can confidently say that I would never have been able to accomplish this without you. And to Koda, who always waited by the door to greet me when I came home from lab, and who, every night, stoically napped at my feet well into the morning hours as I wrote this dissertation. I love you both.

This material is based upon work supported by the National Science Foundation under grants CHE-1659346 and CHE-1752129.

To my brother, who is smarter than me and pushes me to learn more and be a better scientist. To my mom, who the most caring person I know and who made sure my education was well-rounded. And to my dad, for all the nights staying up helping me with homework after a long day at work, for always pushing me to understand how things worked, and for never letting me believe something was too difficult to learn. You instilled in me a scientific curiosity from a young age. This is thesis is dedicated to you.

TABLE OF CONTENTS

Chapter Page

LIST OF FIGURES

Figure Page

LIST OF TABLES

CHAPTER I

INTRODUCTION

Includes co-authored material from:

> Sadighian, J.C.; Wong, C.Y. Just scratching the surface: In situ and surface-specific characterization of perovskite nanocrystal growth. *Journal of Physical Chemistry C* **2021**, *125*, 20772-20782.

1.1 Lead Halide Perovskite Nanocrystals

1.1.1 History of Perovskites

The name "Perovskite" was first used to describe samples of the mineral calcium titanium oxide ($CaTiO_3$) that were collected from the South Ural Mountains in Russia during the summer of 1839.[1] The Chief Mines Inspector of the Russian Empire, August Alexander Kämmerer, had these newly discovered samples sent to Berlin to be delivered to Gustav Rose, a German chemist and mineralogist. Rose had previously accompanied Alexander von Humboldt on a scientific expedition to explore Russia at the request of the Tsar, and would later be responsible for publishing a significant amount of the mineralogical discoveries.[2] Over the course of ten years Rose identified 117 different minerals collected from Russia and described several, such as concrinite, rhodizite, and chevkinite for the first time. After characterizing the physical and chemical properties of the novel $CaTiO_3$ mineral, he published it with the rest of his findings and, having been suggested to do so by Kämmerer, he named it after Russian politician and mineralogist Count Lev Aleksevich Perovski.[1,3–5] Today, the term perovskite extends to any material with the ABX_3 crystal structure.

While at the time the perovskite was a "minor accessory mineral, named after a minor dignitary",[2] the material has since proven to be far more. Studies of the perovskite crystal structure have helped geochemists and geophysicists better

understand the $MgSiO_3$ that makes up a significant percentage of the Earth's mantle.[2] Perovskite-type oxides, such as $SrTiO_3$ and $LaAlO_3$, were awarded the 1987 Nobel Prize for their application in high-T_c superconductors.[6] Most recently, lead halide perovskites (LHPs) have seen a surge in research interest for potential use in photovoltaic and optoelectronic applications.[7–9] While LHPs were studied as far back as the late 1970s,[10–12] they have experienced a revival as an exciting new class of semiconductor owing in part to their attractive electronic properties, such as low exciton binding energy, high carrier mobility, as well as the potential for low-cost, facile syntheses and solution processability. In these $APbX_3$ perovskites, the A-site is occupied by a monovalent cation, typically either an organic molecule such as methylammonium (MA^+), formamidinium (FA^+), or Cesium, and the X^- anion is iodide, bromide, or chloride. Since their debut, solar cells based on LHP films have seen an exponential rise in their power conversion efficiency (PCE), from 3.8%[13] in 2009 to 25.6%[14] in 2021. This has now exceeded the efficiency of Copper Indium Gallium Selenide (CIGS) solar cells, organic photovoltaics (PVs), quantum dot PVs, and dye-sensitized solar cells (DSSCs). The excellent photovoltaic performance of these materials is largely due to the low exciton binding energy[15] and large carrier diffusion lengths.[16] However, these same properties limit their performance as emitting devices. To overcome this, quantum-confined perovskite NCs have been synthesized to increase photoluminescence quantum yield (PLQY) and improve performance in emitting applications.

1.1.2 Properties of Perovskite Nanocrystals

The first solution-based synthesis of colloidal, perovskite NCs was published in 2014 by Schmidt et al.[17] These NCs used octylammonium bromide and octadecylammonium bromide as surface ligands to self-terminate crystallization

and stabilize the discrete nanoparticles in solution. Following this initial report, LHP NCs have have achieved high photoluminescence quantum yield (PLQY) with a narrow emission that is easily tunable throughout the visible spectrum, making these NCs promising candidates for applications in photoemission, photovoltaics, photocatalysis, and quantum information.[17–26] Their large absorption coefficients,[27] high defect tolerance,[28,29] excellent (PLQY),[30] and potential for low-cost, facile production[31] coupled with a narrow, tuneable emission spectrum[32] has driven a boom of research in the synthesis and characterization of these materials.

Despite the enormous progress that has been made in understanding these materials, several key questions still remain unanswered. The interaction of the NC surface with capping ligands can mediate nucleation and growth kinetics and modulate chemical and structural stability, electronic structure, and excited-state dynamics.[33–35] An understanding of how the surface evolves during NC growth, processing, and degradation will enhance our ability to rationally design NCs with targeted photophysics. The promise of rational materials design has driven significant research towards optimizing the optoelectronic properties of these NCs by changing precursors or adjusting initial reaction conditions to yield NCs with different electronic properties or morphologies.[32,36–42] A mechanistic understanding of nucleation and growth in these NCs would aid in this effort, however this will require further development and application of instrumentation and techniques specifically designed to study NC surfaces such that measurement timescales can be short, enabling accurate in situ measurement.

1.1.2.1 Defect Tolerance & Quantum Yield

One of the most important properties of LHPs for optoelectronic applications is their robust defect tolerance.[29] Defects are interruptions in the

crystal lattice, such as interstitials or point vacancies, that can modulate the electronic structure. If these defects create states that lie within the band gap they can trap charge carriers, leading to non-radiative recombination events that suppress PLQY. LHP NCs are considered "defect tolerant" compared to more traditional nanomaterials, such as CdSe. LHP NCs demonstrate optoelectronic properties that frequently appear as if no electronic traps are present. In fact, LHP NCs have achieved PLQYs of ≈100%.[43] This is due in part to the fact that many defects create states that likely lie inside the valence and conduction band, or lead to shallow trap states.[29,44] Additionally, DFT calculations of bulk $MAPbI_3$ indicate that some defect species with low formation energies, such as methylammonium and iodine interstitials, and lead vacancies, either do not form midgap states or only form shallow electronic traps.[45,46] As a result, LHP NCs have the potential to act as excellent emitters.

1.1.2.2 Tuneable Bandgap

In addition to a highly efficient emissive yield, optoelectronic applications such as display technologies require materials with a narrow emission bandwidth and a tunable bandgap. The emission full width at half-maximum (FWHM) of LHP NCs is narrow, and the bandgap can be tuned throughout the visible spectrum by adjusting the size of the NC or the halide composition.[47] Methylammonium lead triiodide ($MAPbI_3$) or mixed-halide $MAPbBr_xI_{1-x}$ NCs are used to emit red light, pure-Br containing NCs emit green light, and Cl or mixed-Br/Cl NCs can emit in the blue part of the visible spectrum.[47–51] Recent development of a novel anion-exchange allowed the use of blue (FWHM = 16 nm), green (FWHM = 18 nm), and red (FWHM = 18.5 nm) LHP NCs to create full-color emitters,[52] demonstrating the commercial potential of these materials.

1.1.3 Stability of Perovskite Nanocrystals

While the electronic properties of LHP NCs are highly desirable, they are currently limited by major stability issues. These materials are highly susceptible to water and other highly polar solvents, and are prone to chemical decomposition as a function of temperature, oxygen, and photoexcitation.[29,53–56] They are also susceptible to a phase transition to the non-emissive "yellow" phase.[57] The combination of chemical instability of $MAPbI_3$ NCs and phase instability of $CsPbI_3$ NCs has led some researchers to term the challenges associated with stable red emission the "perovskite red wall."[58] Additionally, mixed-halide perovskites of bromide and iodide have been found to undergo ion segregation during prolonged excitation, leading to instability in the bandgap and, thus, the emission.[51] These challenges will need to be overcome for LHP NCs to be successful optoelectronic and photovoltaic materials.

1.1.4 The Role of Surface-Ligand Interactions on Nanocrystal Properties

The large surface-area-to-volume ratio of NCs means that the surface, and its interactions with ligand molecules, can dictate the characteristics of the overall particle.[33,34] These interactions have been shown to determine morphology, electronic structure, and excited state dynamics. Surface-ligand adsorption can be highly dynamic, with ligands rapidly adsorbing and desorbing from the NC surface, necessitating stoichiometries that can drive this equilibrium toward sufficient ligand coverage.[59] These ligands play a vital role in the acid-base chemistry that solvates the ionic precursors and drives nucleation and surface binding.[60,61] Surface ligation may also occur as its own distinct stage of growth once the NCs are near their final size.[62,63] Additionally, experimental evidence

suggests growth processes in perovskite NCs are controlled by ligand binding.[64] Thus, understanding how ligands affect the growth mechanism is critical for producing NCs with targeted properties. However, a mechanistic picture of the evolving surface has been elusive owing to the inherent difficulty in quantifying the unstable NC surface during growth. The most basic mechanistic model of NC formation is that of LaMer nucleation and subsequent growth through addition of monomer.[65] In this model, burst nucleation occurs from a supersaturated precursor solution followed by diffusion-mediated growth of the NC. LaMer's mechanism has guided our understanding of NC growth for decades; however, this is not the only mechanism by which colloidal NCs can form in solution. Alternative mechanisms, such as heterogenous nucleation, aggregative growth, or oriented attachment can occur under certain reaction conditions and have critical implications for the resulting NC surface.[66] LaMer's model relies on the existence of unligated monomer and utilizes multiple simplifications regarding how monomer diffuses and adds to growing nuclei. These assumptions do not hold true for the synthesis of perovskite NCs.[67] Because this model does not account for the role of the surface-ligand interactions, it fails to guide our understanding of perovskite NC growth. Perovskite NCs are commonly synthesized through either a hot-injection or ligand-assisted reprecipitation (LARP) technique. These reactions have short timescales, producing fully-grown NCs in only a few minutes, which limits the number of characterization techniques that can be utilized for in situ measurement to study the mechanisms of nucleation and growth. As a result, perovskite NCs are typically only characterized once fully grown and after multiple purification steps, limiting our understanding of how they form. Alternative syntheses have utilized creative solvent-precursor interactions or activation pathways to slow down NC synthesis

to timescales of tens of minutes to hours, permitting the use of some traditional, steady-state characterization techniques.[48,63,68] However, there are tremendous opportunities for advancement if additional rapid-acquisition characterization techniques capable of reporting on NC surfaces in situ during growth can be brought online. NC surfaces have typically been studied using characterization techniques that either measure chemical structure or probe electronic structure that is sensitive to NC surface trap states. This section will discuss various structural and spectroscopic characterization modalities that each provide a great deal of useful information but require measurement timescales or measurement conditions that make investigation of perovskite NCs growth challenging. Recent advances to some of the characterization techniques I discuss have shortened the timescales necessary for data acquisition, and for some modalities the development of specialized sample cells and probes have allowed typical synthetic conditions to be mimicked during measurement. Here, I highlight some of these advancements, the new insights they have enabled, and assert that further advancement of this kind is critical towards a complete understanding of perovskite NC growth. The next section discusses how ligands impact the nucleation and growth of perovskite NCs, how they contribute to NC photophysics, and recent work done to identify the precise nature of these complex interactions. I will then review work that leverages different characterization techniques to elucidate the NC surface and in situ measurements that have provided insight into perovskite NCs. I emphasize significant gains in understanding that could be achieved through the further development of in situ characterization modalities. Establishing an updated, surface-inclusive model of perovskite NC growth hinges on the advancement of in situ instrumental techniques capable of observing changes in morphology,

electronic structure, and ligand binding during NC synthesis. Moreover, such advancements would permit observation of the NC surface during other important non-equilibrium processes such as ligand-exchange, ion migration in mixed-halide perovskite NCs, and photodegradation. While this work emphasizes the need for a better understanding of the surface during NC growth, the advancements suggested in this section would be broadly applicable to the entire life cycle of perovskite NCs.

1.1.4.1 Surface Ligands in Perovskite Nanocrystals

Ligands play multiple roles for NCs; they can modulate NC nucleation and growth, stabilize NCs by preventing degradation and agglomeration, mediate charge transfer to other species, and affect NC electronic structure. Perovskite NCs are typically synthesized with one-electron donating (X-type) ligands. This is usually a pair of ligands, an amine and an organic acid, that either ionically bind to the A or B site cation or substitute in the A site position and complex with the halide ions.[69,70] Oleylamine (OAm) and oleic acid (OA) are frequently used to synthesize perovskite NCs because they are liquid at room temperature and can form oleylammonium halide, oleylammonium carboxylate, and lead oleate complexes at the surface. The binding of these complexes at the NC surface is highly dynamic, however, requiring high concentrations of ligand in solution to yield NCs with substantial surface coverage.[59,61,71–73] Ligand exchange can be performed either during or after synthesis to replace the original surface species with ligands that modify NC behavior, such as by arresting growth or stabilizing the crystal structure. This can also affect NC photophysics, for example by improving PLQY or by suppressing halide segregation.[51,74,75] Contradicting reports exist in the literature regarding the precise binding of amine and acid ligands.

Some evidence suggests that only carboxylates bind to the NC surface, whereas other experiments suggest that the surface binds a combination of ammonium-halides and ammonium-oleate ion pairs.[59] Nuclear magnetic resonance (NMR) and energy-dispersive X-ray spectroscopy (EDS) studies of bare and ligated perovskite NCs suggest a synergistic binding effect between octylamine and OA, where OA acts to protonate octylamine and drive its binding to the NC surface, which in turn attracts OA into the ligand sphere.[76] Additional research has shown that, following ligand exchange, cooperative binding effects between ligands can also improve surface passivation.[51] A more complete understanding of ligand-ligand and ligand-surface binding would aid efforts towards ligand-engineering of NCs for specific applications.

1.1.4.2 Ligands and Nanocrystal Growth

The classical model of colloidal nucleation and growth, as first described by LaMer and Dinegar in their seminal manuscript, does not include the participation of surface ligands in the synthetic process (Figure 1a).[65] In general, the LARP or injection-based synthetic methods through which perovskite NCs are frequently grown contrast significantly to the conditions LaMer's model described (Figure 1b). In LaMer's study of sulfur sol growth, nucleation occurred in a single solvent with only one precursor species. A typical perovskite synthesis utilizes at least two different solutions, with two dissolved ionic precursor salts and two different ligands, and nucleation happens after the two solvents are rapidly mixed. As a result, LaMer's approximations are inappropriate for modeling perovskite NC growth.

The complex ligand-NC and ligand-ligand interactions during NC growth have been investigated using a number of strategies. The synthesis of $MAPbBr_3$

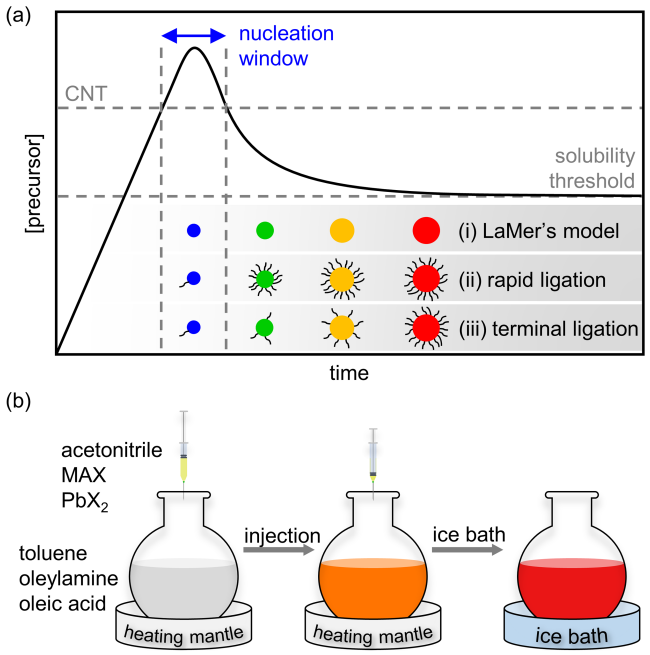

Figure 1. (a) LaMer's model of colloidal nucleation and growth, wherein the precursor concentration increases until the critical nucleation threshold (CNT) is reached, causing a rapid burst of nucleation until the precursor concentration drops below this threshold. Colloids then grow as precursor diffuses to the surface. LaMer's model (inset cartoon (i)) does not address the role of ligands. Perovskite NC surfaces may become rapidly ligated after nucleation ends (ii) or not until the terminal stage of NC growth (iii), each with unique consequences for growth kinetics. (b) Illustration of an injection-based perovskite NC synthesis. A room-temperature precursor solution is rapidly injected into a hot antisolvent, sometimes containing ligands and other precursor species. Nucleation is quenched by moving the reaction mixture to an ice bath, rapidly changing the CNT. Concentration and temperature gradients are not considered in LaMer's model. Reprinted with permission from ref. 32 © The American Chemical Society.

NCs, where MA denotes the methylammonium cation, was demonstrated to slow in the presence of high ligand concentrations, suggesting decreased reactivity of the precursors and nuclei surfaces.[77] OAm and OA were found to act on both the Pb precursor and surface sites via three proposed interactions: 1) formation of a Pb^{2+}-OAm complex through donation of the amine lone pair, 2) protonation of OAm by OA, with deprotonated OA coordinating to Pb^{2+}, and 3) formation of Pb-oleate

without assistance from OAm.[77] In a synthesis of $CsPbBr_3$ NCs, OAm was shown to solvate the $PbBr_2$ following protonation by OA.[78] NMR measurements found that $Cs_2AgBiBr_6$ double-perovskite NCs synthesized with OA and OAm only have OAm bound to their surface, although an acid such as OA or diisooctylphosphinic acid was critical for achieving high NC yields.[79] The identity of the amine is also important: attempts to substitute OAm for secondary or tertiary amines resulted in the formation of undesirable and inseparable side-products along with the desired NCs. In addition to simply adsorbing to the surface, some ligands exfoliate the NC surface, removing or replacing atoms in the crystal structure during either growth or a post-synthetic ligand treatment.[51,71] The more ionic nature of this substitution would strongly influence growth by affecting the kinetics, as well as the particular facets over which growth and ligation occur. This would affect NC growth regardless of the mechanistic pathway, whether it occurs through diffusive growth as predicted by LaMer's theory, or during a non-classical growth process such as Ostwald ripening, which has been observed to be ligand-mediated in ZnO NCs.[80] Conclusive descriptions of surface-ligand binding and how interactions between each of the various species impacts nucleation and growth has not yet been achieved.

1.1.4.3 Impact of Surface Ligands on Electronic Structure and Dynamics

Ligand binding can alter the electronic structure of NCs through a variety of means. NC emission has been found to red shift and narrow solely due to increased binding of surface ligands.[62,63] Ligand exchange has been used to tune the band gap of perovskite NCs by introducing functionalized ligands that adjust halide composition or degree of quantum confinement.[51,81,82] Electron-phonon

coupling in perovskite NCs, which can be a significant source of emission linewidth broadening at operational temperatures, can also be suppressed by a judicious choice of ligands.[83] Surface ligands also influence excited state dynamics, as they can bind under-coordinated surface atoms housing local electronic states that energetically lie within the bandgap.[33,34] These under-coordinated surface sites can trap electrons or holes, promoting non-radiative recombination and hampering the performance of emissive devices. For example, $MAPbBr_3$ NCs that were synthesized with a bare surface via a ligand-free technique were found to have a PLQY of only 0.05% and a short PL lifetime, indicating an abundance of electronic traps arising from unpassivated surface sites. After addition of octylamine, the PL spectrum remained unchanged while the PLQY increased by a factor of 20 and PL lifetime increased by an order of magnitude.[76] There are indications that the diverse species of ligands used in perovskite NC syntheses and post-synthetic treatments may act cooperatively to cap the surface, but this is not yet precisely understood. In the example above, addition of OA alone did not change the PLQY, however the addition of OA with even small amounts of octylamine was found to provide a PLQY increase on par with large amounts of just the amine.[76] The difference in binding behavior of these ligands alone and in the presence of one another suggests that they work in conjunction to passivate NC surfaces.
The precise structure and composition of the electronic traps created by under-coordinated surface atoms is also not clear. Surface traps have been suggested to arise from halide anions that are in a dynamic equilibrium between the NC surface and solvated as a halide salt. This results in the formation of halide vacancies within the perovskite lattice, creating under-coordinated Pb^{2+} ions that can trap electrons to become Pb^0 (Figure2a).[76] Other reports have suggested that, in mixed-

halide perovskite NCs, electronic traps most likely arise from interstitial iodide defects that trap holes.[51] It has been proposed that these interstitial iodides can migrate to the surface, deleteriously effecting NC structural and spectral stability. Better control of synthetic parameters and the equilibria that affect the NC surface would help identify and control the origin of detrimental electronic carrier traps.

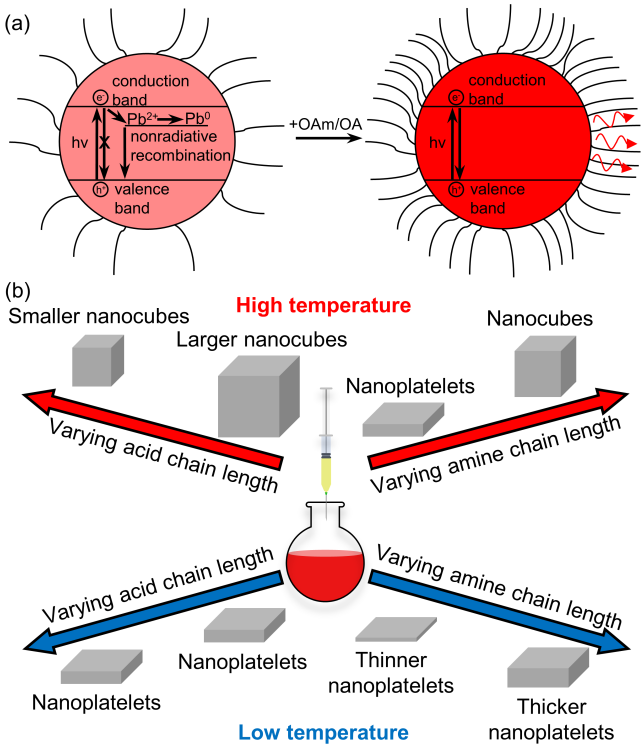

Figure 2. (a) Perovskite NCs with poor surface ligand coverage have surface Pb2+ atoms that form carrier trap states that lie within the bandgap. Ligating these undercoordinated atoms with OAm and OA increases PLQY. (b) Effect of ligand chain length and temperature on morphology of perovskite NCs. Reprinted with permission from ref. 32 © The American Chemical Society.

While binding under-coordinated surface sites with a ligand can passivate a local trap state, raising its energy above the bandgap, ligands can also be used as electron or hole acceptors to aid in light harvesting or photocatalysis applications. Azzaro et al. demonstrated that CdSe NC films functionalized

with exciton-delocalizing ligands exhibited increased exciton transport rates and diffusion lengths, while Wang et al. showed that increasing the length of the alkylammonium ligand can decrease the rate of energy transfer between perovskite NCs in solution.[84,85] Potential photocatalytic activity is also strongly dependent on the NC surface, as different facets can exhibit different activities for processes such as CO_2 reduction.[86] Functionalizing the surface with electron-donating or electron-withdrawing ligands has been proposed to improve photocatalytic efficiency. Additionally, one of the major limitations of perovskite NCs for photocatalytic applications is their stability, which is tied to surface-ligand interactions.[87]

1.1.4.4 Structural Transformation by Surface Ligands

Surface ligands can significantly affect the morphology of perovskite NCs, altering both the shape and crystal structure. While perovskites tend to form cubic nanostructures, varying the length and functional group of NC surface ligands has been shown to modulate their final size and drive the NCs towards different morphologies.[70] Additionally, the perovskite crystal structure can exist in either a cubic, tetragonal, or orthorhombic crystal phase, each with distinct properties.[88] While a review of this field is outside the scope of this chapter, I will briefly discuss a few results that address the role of surface ligands in structural transformation. The chain length of both the amine and acid has been shown to play a role in NC size, with experiments showing that increasing the length of the organic acid results in smaller nanocube structures. Inversely, increasing the length of the amine increases the size of the resulting cubic NCs (Figure 2b).[36,89] Short-chain amines have been shown to promote the formation of nanoplatelets of various thickness, with increasing amine chain length reducing the lateral dimension of nanoplatelets, eventually returning to the formation of cubic shapes.[90] These

observations are attributed to a Van der Waals interaction between the amine ligands and a tendency for preferential binding to certain facets of the NC surface, altering growth kinetics. The acid:amine ratio has also been shown to play a role in mediating the structure of perovskite NCs; higher ratios of acid produce perovskite microsheets, while 1:1 or larger ratios of the amine produce cubic NCs. Continuing to increase the relative amount of the amine produces larger nanocubes. In addition to guiding morphology, surface ligand ratios have been shown to mediate phase transitions in perovskite NCs. Excess OA can cause formation of the tetragonal perovskite phase, whereas excess OAm induces degradation and some transformation to a hexagonal phase.[78,91,92] Substitution of OA and OAm with cross-linking ligands prevented this phase transition, and increased the stability and device efficiency of NC film photovoltaics.[93] The nature of this phenomenon is still poorly understood, and a greater understanding of how the surface regulates these non-equilibrium processes will aid in the development of better nanomaterials.

1.1.5 Common Methods of Surface Characterization

A complete understanding of NC nucleation and growth remains an elusive objective. Attaining this ambitious goal requires further development of true in situ characterization techniques. These types of measurements must overcome several challenges. NC surfaces are dynamic during growth, so nascent NCs are difficult to isolate for characterization modalities that require extended periods of time. The timescales associated with common perovskite NC syntheses are short, so measurements must be acquired within seconds to be able to resolve changes occurring in growing NCs. If the goal is to provide insights that are useful to synthetic chemists, it is also important that the in situ characterization occur during syntheses that closely mimic those in a typical wet-laboratory environment.

Below, I highlight a small selection of common NC characterization techniques and their application to investigate perovskite NC growth, with a particular focus on the NC surface, and discuss recent progress in adapting these techniques to in situ characterization. I assert that further development of in situ characterization techniques is critical to the goal of deepening our understanding of perovskite NC surfaces and their influence on nucleation, growth, and the emergence of NC photophysics during these processes.

1.1.5.1 Nuclear Magnetic Resonance (NMR)

NMR is a powerful spectroscopy that can probe the local environment of both ligands and the NC surface.[94] These experiments can give detailed, atomistic information on the terminating surface layer and ligand binding motifs, as well as information about A-site cation rotation in certain perovskites. Their high resolution can provide information about both the ligands and core atoms and can probe NCs in solution, permitting measurement in conditions much closer to that of actual synthesis. For example, NMR has shown that the concentration of ligand determines the lead-halide intermediate present in solution during a hot-injection synthesis.[95]

Line broadening and chemical shifts in ^{1}H-NMR spectra are frequently used to detect changes in the alkene proton and methyl resonances that arise from organic ligand adsorption to the NC surface. For alternative ligand moieties, such as trioctylphosphine oxide, ^{31}P-NMR can be employed. While these techniques can provide evidence of bound ligand, they cannot conclusively determine that the ligand is bound to a NC. Diffusion-ordered NMR spectroscopy (DOSY) and nuclear Overhauser effect spectroscopy (NOESY), however, can provide conclusive proof of ligand-NC binding. In DOSY, a translational diffusion coefficient is established

for each resonance signature, allowing determination of resonances originating from ligand that is tumbling along with the NC. NOESY can report on through-space interactions within a sample, enabling the identification of resonances originating from ligand that is spatially proximal to a NC (Figure 3a). These techniques have provided useful insights into the surface of stable perovskite NCs. A study utilizing ^{1}H-NMR, NOESY, and DOSY elucidated the dynamic surface-ligand interactions of $CsPbX_3$ perovskite NCs, finding oleate bound strongly to under-coordinated Pb and Cs while OAm bound weakly, perhaps through protonation of halides on the NC surface.[96]

While NMR is an incredibly powerful structural characterization tool, it is difficult to adapt this technique for in situ measurements as lengthy observation times and low temperatures typically aid in the acquisition of high-quality measurements. Long sample preparation times can also hinder the measurement of unstable samples, though the development of specialized probes that allow reactions to occur inside the instrument can overcome this issue.[97] A recent experiment utilizing in situ NMR revealed the reorientation of the MA cation in $MAPbBr_3$ perovskite NCs upon photoexcitation (Figure 3b).[98] This work used solid-state ^{2}H NMR, which cannot easily be applied to solution-based NC syntheses, but future efforts may enable new insights into perovskite NCs during growth. For example, Mashiach et al. studied the growth of CaF_2 and SrF_2 NCs in situ using liquid-state ^{19}F NMR, showing that the growth mechanism could be controlled by altering the species of ligand present in the reaction mixture.[99] While these experiments show what can be accomplished with in situ liquid-state NMR, the interpretation of measurements during perovskite NC growth may be challenging, as these reactions involve a greater number of species which yields interspecies interactions with

greater complexity. Additionally, the NMR methods that yield the most detailed and conclusive information about ligand–NC binding, DOSY and NOESY, are not easily adapted to in situ study because of their low sensitivity and lengthy measurement times. Although a significant technological advance would likely be needed, the payoff would be large: the ability to achieve quantitative information about the evolving ligand–NC binding interactions and the ligand conformations during perovskite NC growth would have a dramatic impact on our ability to rationally design these NCs.

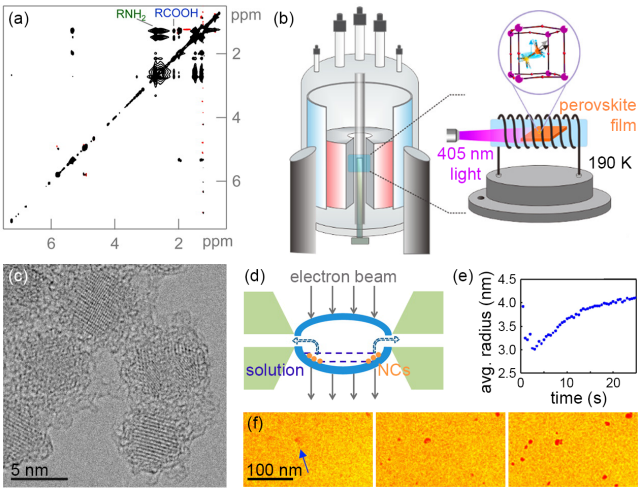

Figure 3. (a) 2D-NOESY spectrum of perovskite NCs. The negative (black) cross peaks assigned to the amine group of OAm and the carboxylic acid group of OA show that a fraction of both ligand species bind to the NC surface. (b) NMR apparatus used to observe cation rotation in situ during photoillumination of $MAPbBr_3$ NCs. (c) HR-TEM of alkene-passivated Si NCs deposited on atomically precise graphene substrate. This technique requires sophisticated sample preparation procedures that preclude in situ measurement. (d) Schematic of liquid flow cell TEM used to study formation of perovskite NCs in situ during growth. (e) Change in average radius of perovskite NCs calculated from (f) TEM images collected in situ during e-beam-induced solvent vaporization and NC growth in TEM flow cell. Reprinted with permission from ref. 32 © The American Chemical Society.

1.1.5.2 Transmission Electron Microscopy (TEM)

TEM is one of the most common techniques for determining NC size and shape.[100,101] In this technique, a high energy electron beam interacts with the sample, typically mounted on a carbon substrate, and the transmitted electron beam is detected. Some TEM instruments have additional characterization modalities, such as energy dispersive spectroscopy and electron energy loss spectroscopy, which allow investigation of chemical composition and bonding and can provide an enormous trove of information. However, it is difficult for TEM to inform on surface-ligand binding because of the low Z (atomic mass) contrast between the ligand and the amorphous carbon substrates that are typically used, so creative experiments are needed to improve this contrast (Figure 3c).[102] There are significant challenges that make in situ TEM measurements difficult, particularly for perovskite NCs. The high energy electron beam can induce degradation and can unintentionally alter the sample by heating, atom displacement (knock-on damage), defect formation, and radiolysis.[100,101,103] Organic-inorganic perovskites are known to be particularly sensitive to damage from electron beams.[104,105] It has been hypothesized that electron-beam damage may be somewhat mitigated by self-healing effects reported in perovskite materials, but this would also suggest that the electron beam is still altering the growth mechanism.[105] In situ TEM was recently used to observe that electron beam-induced degradation of $CsPbI_3$ NCs initiates at surface defects.[106] Electron beam-induced effects can be reduced by using low-energy electron beams and accelerating voltages, however this also negatively impacts resolution.[107] While the overall electron dose can be lowered, the development of more advanced detectors is critical to offset the resulting loss in image quality. It is also challenging to design in situ TEM measurements that

are easily relatable to a typical wet-laboratory synthesis, as the high-vacuum conditions necessary for typical TEM measurements do not mimic those in a chemical flask. Attempts to perform true in situ TEM measurements have led to the development of innovative liquid- and gas-cells. For example, liquid-cell TEM was used to observe Ag NC growth by oriented attachment.[108] Nucleation and growth of $MAPbI_3$ perovskite NCs has also been observed in situ using liquid-cell TEM, revealing growth that could neither be explained by diffusion-limited or reaction-limited mechanisms (Figure 3d-f).[109] In these experiments, however, nucleation was induced via solvent evaporation resulting from the electron beam. The design of specialized cells that aim to mimic wet-lab conditions can be highly challenging as they can introduce new chemistry or bias the occurrence of various processes when compared to a wet-laboratory synthesis. For example, the threshold for heterogeneous nucleation may shift owing to changes in the relative amount of surface area or the energy of the liquid-cell surface. As discussed in a recent perspective, it is critical that the mechanistic difference between reactions run in a flask and those run under electron-beam conditions be better understood so that in situ TEM measurements can be interpreted correctly in the broader context of perovskite NC growth.[110] Again, however, overcoming these obstacles would have a huge payoff, as a truly atomistic picture of ligand binding and conformation during NC growth would revolutionize our ability to control NC syntheses.

1.1.5.3 X-Ray Photoelectron Spectroscopy (XPS)

XPS can selectively probe elemental composition at different depths within a material. This technique has been successfully used to better understand functionalized interfaces in bulk perovskite films.[111] Compositional analysis of perovskite NC surfaces, however, requires a depth resolution of nm or better, which

is only achievable using synchrotron-radiation (SR)-excited depth-profiling XPS. This technique has been successfully used to study ion exchange occurring at the surface of metal NCs as small as 3 nm in diameter.[112] When used in conjunction with other characterization techniques, such as those that can determine precise NC diameter, SR-XPS can provide information on the ligand shell and the number of unpassivated surface sites.[113] This would be incredibly useful information for understanding the evolving NC surface during synthesis. In situ SR-XPS has already provided insight into perovskite interfaces; measurements during the thermal deposition of Al onto a perovskite film revealed the migration of Al ions into the perovskite lattice, and multiple resulting chemical reactions.[114] Unfortunately, SR-XPS measurements are difficult to perform with a solution-based sample, so truly in situ measurements during a synthesis may not be possible. However, the development of creative rapid samplers at beamline facilities may allow this technique to provide significant insight into NC surfaces.

1.1.5.4 Modulating Reaction Kinetics

One of the largest hurdles in the development of in situ techniques for investigating perovskite NC growth is the time scale over which nucleation and growth occurs. LARP and hot-injection syntheses involve significant engineered temperature and concentration gradients, orchestrated to minimize the time over which nucleation occurs. The entire synthesis is typically complete within a few minutes, hindering attempts to sample the reaction mixture or apply techniques that lack short acquisition times. A potential strategy to circumvent this problem and address the steep gradients associated with traditional syntheses is to slow down the reaction kinetics. Li et al. accomplished this using a microwave-assisted synthesis that extends the reaction time scale to several tens of minutes.[68] The

ability to sample the reaction mixture allowed the intermediates present at different growth times to be characterized, revealing the formation of a bromoplumbate complex with lagging Cs diffusion into the existing lattice. Another alternative synthesis utilizes a nonpolar solvent and relies on the solvation kinetics of the ligand–precursor complexes to drive nucleation and growth.[48] This technique slows NC growth even further to several hours, permitting rapid sampling and spectroscopic investigation using a combination of linear and nonlinear spectroscopies.[63,63,115] These slower syntheses have advantages beyond their convenience for in situ measurements. The environment in which the nuclei form and grow is necessarily not uniform when concentration and temperature gradients are present within the reaction vessel. Thus, faster syntheses that utilize these gradients can be highly sensitive to the reaction conditions such as the exact speed and nature of stirring and injection. This makes them poorly suited for use at an industrial scale. Slower syntheses that allow nucleation to occur in a controlled and uniform environment are thus of great interest, making them useful and convenient targets for investigation using in situ characterization techniques.

1.1.5.5 Multimodal Characterization

Multimodal instrumentation that can concurrently measure NCs using multiple characterization tools can provide complementary datasets that yield a deeper understanding of the chemical and electronic structure of NCs. Multiple characterization techniques can often be sequentially applied to a single, stable sample. Fiducial markers can be used to ensure that the same NC is measured using different techniques, and for ensemble NC measurements even this complication is removed. However, perovskite materials are structurally unstable and evolve quickly during their formation, complicating the sequential

use of characterization tools. It is particularly important to use multimodal in situ characterization techniques to advance our understanding of perovskite formation.[116] For example, a multimodal instrument that measured in situ X-ray diffraction, optical microscopy, and PL of bulk perovskite revealed unique morphological features of the perovskite precursor phase, and spectral changes could be assigned to the nucleation and growth of a perovskite film.[117] These results uncovered a previously unknown dependence of nucleation and growth rates on the identity of the lead-halide precursor salt, and this new insight may enhance film coverage.

Compared to the study of perovskite film formation, concurrent measurements using different characterization tools are arguably even more critical for the study of perovskite NC growth in situ. Perovskite NCs can be highly sensitive to reaction parameters and environmental conditions during synthesis. Thus, if multiple characterization techniques are to be used to understand NC growth, it is imperative that the growth process reported on by each technique be identical, without the environmental conditions required by each measurement influencing or changing the reaction. This can be ensured by conducting each measurement on the same sample, at the same time, in the same instrument. A few examples of this have already been reported for perovskite NCs. Darmawan et al. combined atomic force microscopy with a single molecule time-resolved photoluminescence (TRPL) instrument that allowed them to simultaneously measure perovskite NC size, emission spectra, and PL dynamics during degradation (Figure 4).[118,119] This combination of techniques allowed changes in the NC size that coincided with photodegradation to be correlated to NC surface quality as determined by PL decay dynamics. Others have combined electrochemistry with

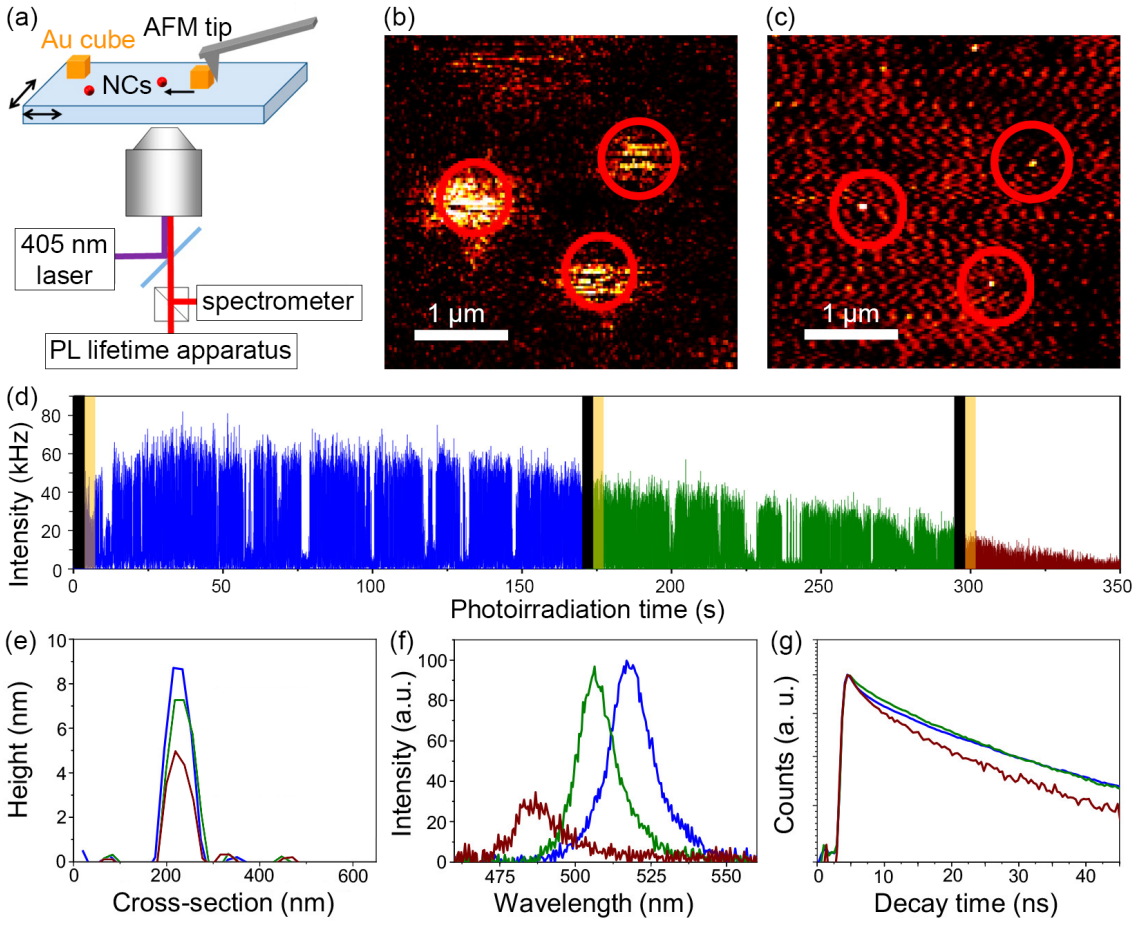

Figure 4. (a) Multimodal instrument used to simultaneously measure height and PL of $CsPbBr_3$ NCs during photoinduced degradation. Simultaneous (b) PL and (c) AFM measurements of $CsPbBr_3$ NCs. (d) PL intensity of an individual NC during photoillumination. Evolution of (e) AFM cross section, (f) PL spectrum, and (g) PL lifetime of the single NC from (d) before (blue), after 170 s (green), and after 300 s (red) of illumination. Reprinted with permission from ref. 32 © The American Chemical Society.

both linear and non-linear optical spectroscopies to study the electronic structure of quantum dots.[120] This enables the study of optical transitions as a function of applied potential, differentiating between intrinsic electronic states and surface traps. While individually these techniques are already useful characterization tools, concurrent investigation was critical for these important conclusions to be drawn.

The pairing of in situ structural characterization modalities with spectroscopic modalities would be of particular utility, as this could allow the structural evolution of NCs to be directly correlated to changes to electronic structure and excited state dynamics. Further development of multimodal instrumentation for in situ measurements will increase our understanding of how NC surfaces evolve during nucleation and growth, and how ligands can be used to engineer these surfaces to yield tailored electronic and chemical properties.

1.1.6 Outlook

The lack of a mechanistic understanding of how perovskite NC surfaces evolve during growth, post-processing, and degradation limits our ability to tailor the photophysics of these materials. It is difficult to measure NC surfaces using either structural or electronic probes, and this difficulty is exacerbated when the surface is evolving. In situ measurement techniques have begun to shed light on unstable NCs and their interactions with ligands during growth, but further development of these techniques is needed. In situ measurements present some unique challenges: they must be rapid relative to the rate of NC growth, must not interfere with or alter the growth process, and should be performed during growth under typical reaction conditions to yield maximally useful insights to the synthetic community. As with all samples, deeper insight can be gained by using multiple characterization techniques, but again, complexity is introduced when measuring perovskite NCs during growth. Perovskite NC growth can be quite sensitive to reaction conditions, so instruments that can perform multiple types of measurements concurrently on the same sample are of particular utility. While there are significant challenges to overcome, the rewards of gaining a deeper

understanding of perovskite NC surfaces during growth would be significant given the impact of the NC surface on photophysics.

1.2 Ultrafast Transient Absorption Spectroscopy

1.2.1 Electronic and Vibrational Spectroscopy for Investigation of Perovskite Nanocrystals

Electronic spectroscopy probes transitions between electronic states in NCs, which can be affected by surface–ligand interactions. In addition to modulating electronic structure, ligands can also influence excited-state dynamics if they passivate surface trap states or introduce new charge transfer pathways. The presence of unpassivated surface states is often associated with lower PLQY since photogenerated excitons that undergo carrier trapping are less likely to recombine radiatively. Scatter and inner-filter effects must be considered and overcome, but in general, photoluminescence (PL) is relatively easy to measure in situ during a typical wet-laboratory synthesis since the measurement time is short and probes for this purpose have become commercially available. In situ PL measurements were recently reported during a hot injection synthesis of $CsPbBr_3$ NCs,[121] revealing discrete stages during the hot-injection growth process whereby nucleation results in perovskite nanocubes within seconds. These nanocubes then cluster together to form larger "supercrystals" during the remaining growth period. TRPL spectroscopy can also report on the surface, as nonradiative recombination via unpassivated surface states manifest as changes in the PL dynamics. The increased number of nonradiative recombination centers can act to decrease PL lifetimes.[118] These traps can also manifest as additional components in the dynamics, such as the presence of a picosecond time scale process in the PL decay of $CsPbCl_3$ NCs that disappears after surface treatment to fill surface vacancies.[122] In situ TRPL

measurements would provide useful insight into the evolving NC surface, but this is made difficult by lengthy measurement times.

Carrier trapping at the NC surface or carrier transfer to a ligand also results in transient changes to electronic structure and thus NC absorbance. Measuring these changes by using time-resolved differential absorbance spectroscopies such as transient absorption (TA) can indirectly provide insight into the NC surface. However, acquisition times for time-resolved measurements are typically on the order of several minutes to hours, too long for in situ measurement during NC growth. As a result of this difficulty, time-resolved optical spectroscopies are rarely performed in situ on unstable samples, and there is tremendous potential for advancements in this area. For example, single-shot TA methods can reduce measurement times down to seconds, which permits the acquisition of broadband TA spectra during the nucleation and growth of perovskite NCs.[115] This technique has been used to observe a pump-induced Stark shift in perovskite NCs during growth, ascribed to trapped carriers at the NC surface (Figure 5a,b), as will be demonstrated in Chapter 4. This provides a metric by which surface passivation can be tracked in real time. The data from these TA measurements suggest that perovskite NC surfaces are poorly passivated until late in their growth. In general, compared to the structural characterization techniques detailed above, in situ time-resolved electronic spectroscopies are underdeveloped. Further advancements in rapid-acquisition optical spectroscopies may provide avenues for understanding NC growth that have thus far been unexplored. This may require some creativity, particularly for spectroscopies that are not inherently surface-specific, but utilizing the effect of the surface on the behavior of excitons is a novel strategy for interrogating NC samples in situ during growth and provides a fresh perspective.

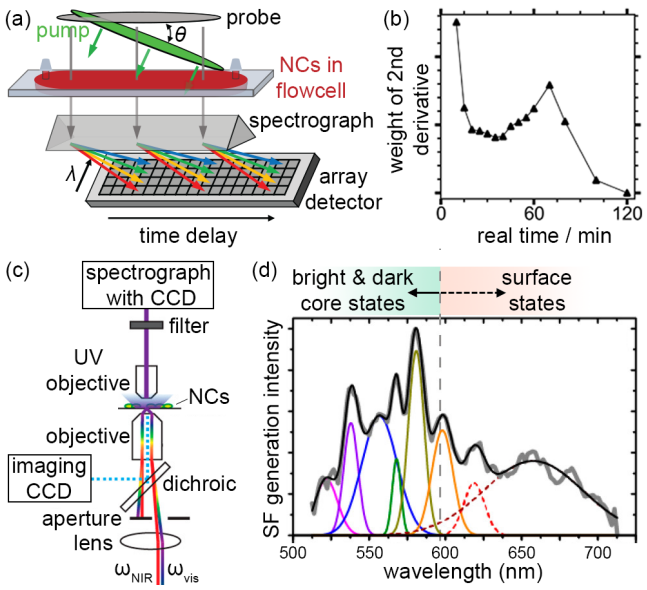

Figure 5. (a) Tilted pulses can spatially encode a pump–probe time delay enabling rapid, broadband, transient absorption (TA) measurements in situ during NC growth. (b) Evolving contribution of second derivative of the absorption spectrum to TA spectra reports on the changing surface passivation during growth. (c) Ex situ electronic sum-frequency (SF) generation spectroscopy used to probe CdSe NCs. (d) NC surface and core states can be individually resolved in electronic SF spectrum. Reprinted with permission from ref. 32 © The American Chemical Society.

While in situ time-resolved electronic spectroscopies may offer unique insight into NC surfaces during growth, these techniques also face significant limitations. Optical probes are diffraction-limited, typically relegating them to ensemble measurements of NC populations unless the NC sample is significantly diluted, which is incompatible with in situ measurement. The broad line widths and range of defect-dependent behavior may result in measurements biased toward the most resonant subpopulations. Furthermore, single-shot techniques that rely on tilted-pulse geometries, such as the technique described above, require spatially uniform beam intensities at the sample plane and careful correction of spatial chirp for accurate measurement, and may be hindered by spatially heterogeneous

samples. Additionally, this technique can only probe the NC surface indirectly, and other non-surface-related properties such as the biexciton binding energy could be involved.

A family of spectroscopies that is particularly well-suited to inspecting NC surfaces is sum frequency (SF) spectroscopy, which is capable of selectively probing molecules and states at interfaces and surfaces with high selectivity.[123] SF techniques can utilize transmitted, reflected, or scattered light, depending on the size of the particles being measured and the wavelength of light used.[124] Generation of an SF signal is only possible in structures that lack inversion symmetry, therefore this technique is considered "surface specific" as it leverages the immediate break in symmetry that occurs at interfaces such as the NC surface or at defects. In situations where symmetry breaking also occurs in the bulk of a sample, such as the interior of small NCs, and where the coherence length is much longer than the width of the interfacial layer, it is possible that signal from the bulk will also be present in the SF spectrum.[125] Use of reflective experimental geometries can significantly reduce or eliminate contributions to the SFG signal from the bulk.[126,127] Vibrational SF generation spectroscopy was used in a reflective geometry with perovskite films to study molecular orientations of MA at interfaces with layers of other materials.[128] Similar measurements of NCs may be able to report on the identity and orientation of capping ligands at the NC surface. Vibrational SF measurements were shown to be sensitive to changes in ligand coverage and ordering that result after washing CdSe NCs with antisolvent, and this type of measurement should also work for perovskite NCs.[129] SF can also isolate signal generated by the electronic structure present at the surface. SF generation microspectroscopy was used to directly observe changes to the number

of sub-bandgap surface trap states following oxidative degradation of CdSe NCs (Figure 5c,d).[130] Similar studies of perovskite NCs would provide insight into the distribution of surface trap states.

The development of in situ SF spectroscopies has provided new insight into the structure of evolving interfaces, for example, buried interfaces in electrochemical cells.[131] However, difficulties may be encountered when performing vibrational SF spectroscopies on solvated, reacting, colloidal NCs, as the vibrational resonances of the solvent itself may attenuate the IR input. This would impede rapid signal acquisition because of the low efficiency of the second-order SF process. Thin sample cells can be used, but this may also result in the detection of signals originating from the sample–cell interface. Creative strategies can enhance signal from the interface of interest, and further development of these methods may allow for the rapid acquisition of SF signals in liquid samples.[132,133] In situ SF techniques could enable surface-specific measurements of NCs during their nucleation and growth, representing another significant opportunity for advancement.

1.2.2 "Traditional" Transient Absorption Spectroscopy

1.2.2.1 Introduction to "Traditional" Transient Absorption Spectroscopy

Transient absorption is a pump-probe technique in which one pulse of light, termed the pump pulse, creates a photoexcited population in a sample and the subsequent transmission of a second pulse, termed the probe, is measured. The probe transmission is compared to itself in the absence of any "pump" excitation and the difference in this transmission is reported. By varying the arrival time between the pump and a broadband probe pulse, this technique can provide a

time-resolved picture of the excited state and how it evolves energetically following photoexcitation.

1.2.2.2 Observable Processes in Transient Absorption

The differential measurement described in a TA spectrum is composed of up to three different processes, ground state bleach (GSB), stimulated emission (SE), and photoinduced absorption (PIA). When ground state bleach and stimulated emission occur, the presence of a pump-generated excited population causes an increase in the detected transmission of the probe pulse, appearing as a negative ΔOD signal in the TA spectrum. Ground state bleach occurs when the pump pulse creates an excited population and, as a result of depopulation in the ground state, there are fewer chances for absorption of the probe pulse. As a result, more probe pulse in transmitted through to the detector. Stimulated emission results in the same thing, only the increase in detected transmission occurs when a component of the probe pulse, following pump generated photoexcitation, interacts with the excited state population causing those electrons to fall back to the ground state, emitting photons. These emitted photons, combined with the original incident photons in the probe beam, are detected as an increase in transmission. While there is no way to know whether the negative ΔOD signal originated from GSB or SE just by looking at the TA spectrum, comparison to the linear absorbance and photoluminescence spectra, along with analysis of the decay dynamics, can assist in the assignment of these features. The positive ΔOD signal caused by PIA occurs when absorption of some resonant component of the probe pulse allows the photoexcited population to access even higher energy electronic states. Thus, the presence of the pump pulse causes additional absorption events when the probe

interacts with the sample, transmitting fewer photons than when no pump pulse is present.

1.2.2.3 Limitations of "Traditional" Transient Absorption Spectroscopy

Despite the wealth of important information on excited state dynamics that TA is capable of reporting on, the technique also suffers from limitations that are particularly highlighted when attempting to study samples that are changing in situ. It is critically important to be mindful of the pump fluence used in TA experiments. If the pump pulse energy is too high, this pulse will create too great an excitation density in the sample. Typical experiments attempt to electronically excite between .1% and 1% of molecules in the sample, however this is heavily dependent on the sample response.[134] Too high an excitation density can lead to multiexciton effects such as Auger recombination. In Auger recombination, carriers interact with and can annihilate each other, changing the measured dynamics and obscuring information about other processes. As a result, it is important to keep excitation density below this threshold. Dynamics are extracted from TA data by fitting the decays of individual transients to functions, typically a sum of exponentials. In order to assure quality fits, it is important to have enough data points in the transient to allow for accurate calculation of dynamics. Each data point requires a retroreflecting mirror be moved so that a new time delay can be measured. This process adds significant time to TA experiments. Finally, as previously explained the reported signal from a TA experiment is the difference between transmission of the excited state and that of the ground state. The overall magnitude of this difference in absorbance can be very small; in the case of experiments reported here, on the order of 10^{-3}. As a result, achieving

acceptable signal to noise while maintaining pulse energies below the threshold for multiexciton effects can require collecting multiple on-off pulse pairs at each time delay position and averaging a large number of complete scans through the time delay range. As a result of all of these factors, TA experiments can require tens of minutes to several hours depending on the response of the sample being studied.

1.2.3 Single-Shot Transient Absorption Spectroscopy

To overcome the limitations associated with TA spectroscopy that restrict its application to non-equilibrium systems, here I employ a novel single shot transient absorption spectrometer (SSTA) that has been developed by our research group. This SSTA spectrometer permits collection of TA spectra of NC samples with good signal-to-noise within one minute, allowing the technique to be applied to systems that are changing on significantly faster timescales than was previously possible. This is possible through several key changes to the instrumental set up. Whereas in a "traditional" TA spectrometer pulses are focused down to spots through use of spherical lenses, in SSTA the pump and probe beams are focused to lines through the use of cylindrical lenses. The spatially elongated probe pulse is incident normal to the sample plane, while the pump pulse is tilted relative to the sample plane. This spatially encodes the pump-probe time delay along the length of the probe, allowing entire TA spectra to be collected with a single pump on-pump off pulse pair. Spatially dispersing the probe pulse over the sample through the use of the cylindrical mirrors requires that our probe beam possess significantly more energy than in a traditional TA experiment, where the tight focal points lend themselves to high energy densities. As a result, typical methods for supercontinuum generation of broadband light fail to provide adequate energy. The most common method to generate a broadband probe is the use of a sapphire

crystal. Use of a solid medium for supercontinuum generation limits the usable energy to the damage threshold of the particular crystal, setting an upper limit on the energy of the broadband probe that can be generated. To circumvent this, an argon cell was employed to permit supercontinuum generation with enough output power to maintain sufficient excitation density without risk of damage to the nonlinear medium. The last major difference between TA and SSTA is the use of a spatial light modulator (SLM) to adjust the beam profile. Each pulse generated by the laser is approximately Gaussian in its intensity profile, however achieving the nearly 60 ps time delay I report with SSTA requires that the beam intensity be spatially uniform.[135,136] This is achieved through the use of a phase-only SLM that is capable of spatially reshaping the beam to any input by redistributing the incoming intensity. This can be used to make the beam more Gaussian and improve the M^2, or in the case of this work used to flatten the spatial intensity profile of the pump and probe beams. The flattened beam profile generated with the SLM is used to excite the sample uniformly in the linear regime.

CHAPTER II

RAPID SAMPLING OF PEROVSKITE NANOCRYSTALS FOR SPECTROSCOPIC INVESTIGATION

Includes co-authored material from:

Sadighian, J. C.; Crawford, M. L.; Wong, C. Y. Rapid sampling during synthesis of lead halide perovskite nanocrystals for spectroscopic measurement. *MRS Advances* **2019**, *4*, 1957–1964.

2.1 Introduction

An understanding of the link between the synthetic route and the photophysics of the product will provide valuable feedback for the rational design of NCs with targeted photophysical properties. In situ spectroscopic measurements may be able to link the evolving photophysical properties of NCs to the structural changes that occur during synthesis. However, spectroscopic measurements such as absorbance, fluorescence, and transient absorption are usually only conducted ex situ on NCs that are at a structural equilibrium after the synthesis has been completed. It is significantly more difficult to measure these properties during NC synthesis when the structure of the NC may still be evolving. The reaction is typically quenched by centrifuging the reaction mixture for several minutes to remove any remaining solid precursor prior to measurement. This is additionally beneficial for spectroscopic measurements since these solid components scatter light and interfere with optical interrogation. Centrifugation is typically performed for many minutes, and since the mixture may continue to react during this process, measurements of centrifuged reaction mixture do not accurately report on the photophysics of NCs in the reaction mixture during growth. As a result, in situ measurements of NCs have largely been limited to steady-state measurements during NC growth[137,138] or time-resolved measurements only during the slower

process of NC degradation.[103,139–141] This chapter describes a technique to rapidly sample perovskite NCs during synthesis, enabling the in situ measurement of electronic structure and excited state dynamics during NC nucleation and growth. In situ measurements during NC growth are only achievable when the reaction proceeds on a timescale significantly slower than that required for data acquisition. Hot-injection[31,142] and ligand-assisted reprecipitation[30,32] are currently the most prevalent techniques for the synthesis of organic-inorganic lead halide perovskite NCs. Since nucleation and growth occur very quickly in both techniques, the synthesis necessarily proceeds amidst concentration gradients. This can result in growth that depends on the exact nature of the injection and mixing of reagents, and limits the scalability of the reaction. To this end, a room-temperature, ambient air synthesis is adopted where NC nucleation and growth kinetics are rate-limited by the solution equilibria.[48] The kinetics of this reaction are more accommodating to in situ measurements, allowing the evolving electronic structure during NC formation to be monitored. The use of a filtration-based reaction quenching technique permits use of a homemade spectrometer capable of simultaneously collecting absorbance and fluorescence spectra to observe how $MAPbI_3$ NCs grow in solution. Following nucleation, NC growth proceeds through a series of decreasingly quantum-confined intermediates that form full NCs on the timescale of several hours. It is shown that the species present in the reaction mixture during NC growth are unstable and continue to evolve after filtration. These species must be measured in the first few seconds after filtration to accurately capture the photophysics during NC growth.

2.2 Methods

$MAPbI_3$ NCs were prepared by a method similar to that described by Wang et al.[48] 55 μL of octylamine and 110 μL of oleic acid were mixed in a scintillation vial containing 22 mL of hexane. The reaction was initiated by adding 191 mg of lead iodide (PbI_2) and 52 mg of methylammonium iodide (CH_3NH_3I) and the reaction vessel was sonicated to induce homogenous mixing. The color of the reaction mixture changed from yellow to red to brown over the first 45 min, after which it was dark brown in color for the remainder of the reaction. 0.5 mL aliquots were periodically withdrawn without interrupting the sonication and filtered through a 13 mm diameter, 0.45 μm pore, PTFE syringe filter into a 1 mm path length quartz cuvette. This removed the solid precursor, quenching the reaction in a similar fashion to centrifugation. The absorbance and fluorescence of these filtered aliquots were measured immediately following filtration unless otherwise noted. The aliquot extracted at 18 min contained too much solid particulate to pass through a syringe filter. This and all subsequent aliquots were first centrifuged for 10 s at 7227 rcf, and the resulting supernatant was filtered into the cuvette.

Absorbance and fluorescence measurements were collected simultaneously using the apparatus illustrated in Figure 6. A xenon arc lamp illuminated the sample for absorbance measurements and a laser diode emitting 405 nm light served as the excitation source for the fluorescence measurements. These two light sources were focused to two non-overlapping spots on the cuvette. Transmitted light was collected using an optical fiber (Thorlabs M92L01) for the absorbance measurement. A second fiber (Thorlabs M53L01) was placed near the cuvette to capture fluorescence emitted from the sample. Both fibers were carefully placed to avoid the transmitted light from the 405 nm laser. Each fiber was directed to a

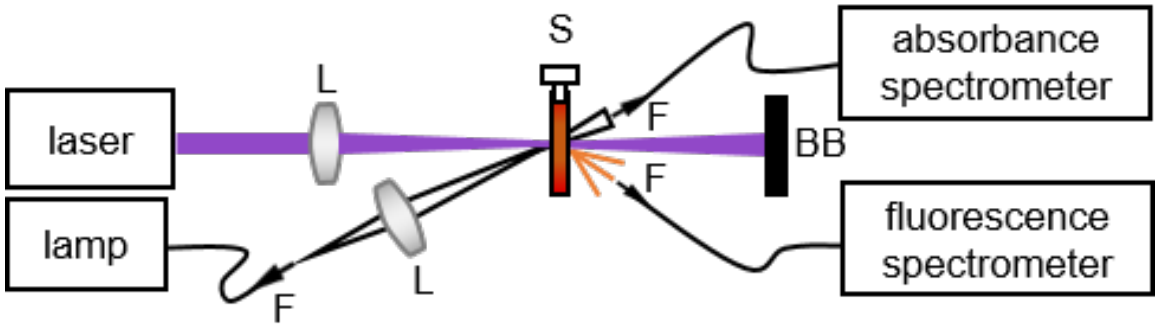

Figure 6. Schematic of apparatus used to simultaneously measure absorbance and fluorescence of sample (S). A lens (L) focuses light from a xenon arc lamp onto the sample and transmitted light is collected using an optical fiber (F). A 405 nm laser serves as the excitation source for fluorescence measurements and is incident on a beam block (BB) after the sample. Emitted photons are captured using an optical fiber.

separate Ocean Optics Flame-T spectrometer for data acquisition. Aliquots were also remeasured periodically after filtering to determine the stability of the NCs. These samples were not exposed to the light sources between measurements.

2.3 Results

Absorbance and fluorescence measurements of aliquots from a NC reaction mixture, collected simultaneously at 23 discrete time points during the synthesis, are shown in Figure 7. In the first few minutes after the reaction is initiated two features are observed in the absorbance spectra, a peak at 375 nm and another peak near the limit of our spectral range at 350 nm (Figure 7a). These features can be assigned to plumbate complexes that have been previously reported in $MAPbI_3$ precursor solutions.[143] The concentration of solvated precursors appears to reach the critical nucleation threshold within 4 min, as indicated by the detection of a weakly emissive feature from 600 nm to 650 nm. Although fluorescence can be detected in the filtered reaction mixture, the absorbance in the visible wavelength

region is negligible at this point in the synthesis. A rapid increase in absorbance and fluorescence is observed in the following minutes. The absorbance spectra show a sharp feature at 550 nm that is consistent with absorption at the excitonic band edge of quantum-confined NCs and this feature continues to gain intensity as the NCs grow. By 11 min and 18 min new peaks appear at 592 nm and 630 nm, respectively. While the absorbance spectra exhibit sharp features with rapid growth between 6 min and 18 min, the change in the fluorescence spectra during the same period is more subtle, Figure 7c. At early reaction times fluorescence spectra have a feature at 600 nm and a slightly smaller peak at 636 nm. These peaks grow in tandem until 11 min when the blue edge of the fluorescence spectrum recedes and the 636 nm peak becomes the dominant feature. By 18 min the fluorescence spectrum redshifts such that the emission is now centered at 647 nm. This coincides with the emergence of the absorbance feature at 630 nm.

After the synthesis has progressed for 30 min the amount of suspended particulate exceeds the capability of the syringe filters, so aliquots withdrawn from the reaction mixture were centrifuged for 10 s prior to filtration. Although the aliquot is only centrifuged briefly, these samples show significantly lower optical density than those that are not centrifuged, yet the fluorescence increases in intensity. This is attributed to components of the reaction mixture that can absorb the 405 nm excitation source but do not fluoresce. The removal of these components from the reaction mixture by centrifugation increases the number of excitation photons incident on NCs that are stable enough in solution to persist in the supernatant. Since NCs that are well-capped by organic ligands are more stable than those that are poorly capped, it is reasonable that the NCs in the supernatant have, on average, less exposed surface and fewer trap states, and thus exhibit

stronger fluorescence. This demonstrates how centrifuging a reaction mixture, even for only 10 s, can dramatically change the photophysics of the resulting NC population. Conclusions that are drawn regarding the properties of NCs during growth will be significantly different if the reaction mixture is centrifuged prior to measurement.

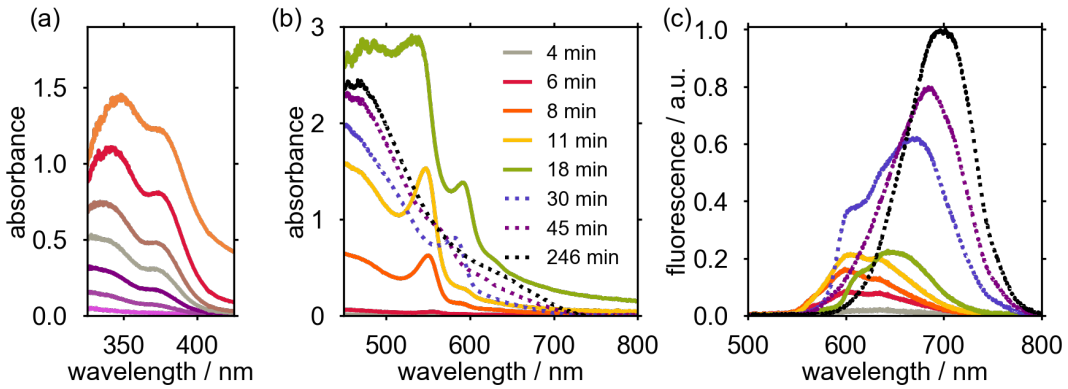

Figure 7. (a,b) Absorbance and (c) fluorescence measured during NC synthesis. The UV absorbance of early-forming lead species is shown in (a) from 1 min reaction time (pink) to 7 min reaction time (orange), in 1 min increments. Dashed lines indicate that the sample was centrifuged before measurement.

The centrifuged sample collected after 30 min of reaction time still exhibits a sharp excitonic-like absorption feature near 590 nm, but this feature becomes less distinct as the NCs continue to grow and the absorbance increases at longer wavelengths. When the NCs have grown for 1 hr sharp features are no longer observed, and following 4 hr of growth the absorbance spectrum exhibits a shoulder at 650 nm that is characteristic of $MAPbI_3$ NCs with weakly-confined excitons. As the synthesis continues the fluorescence spectrum loses the higher energy shoulder at 550 nm and continues to narrow, redshift, and increase in intensity, in agreement

with the self-sharpening regime that has been reported during classical nanoparticle growth.[144]

Tracking the fluorescence intensity as a function of reaction time shows the wavelength dependent growth rates of different features in the observed spectra, Figure 8. At early stages of the NC synthesis the intensity of the two higher energy fluorescence peaks at 600 nm and 636 nm (vide supra) grow at nearly identical rates. After 11 min of reaction time the intensity of the peak at 600 nm begins to decline while emission continues to increase at longer wavelengths. The rate of growth in fluorescence intensity decreases with increasing wavelength, with negligible intensity measured at 733 nm until reaction times exceeding 20 min. During this stage of the synthesis, the centrifuged and filtered reaction volumes exhibit receding fluorescence features at 600 nm and 636 nm while the rest of the spectrum continues to rise in intensity. Sharp features are not observed in the fluorescence spectra above 636 nm, indicating that photogenerated excitons are no longer strongly confined by the NC. Smaller NCs within the measured population contribute to the blue edge of the fluorescence feature, while larger NCs contribute to the red edge. As the average NC size continues to increase the confinement of excitons continue to weaken, causing the fluorescence spectrum to continue to redshift. Traces of the intensity at three wavelengths within this fluorescence feature show that the population of smaller NCs declines during this stage of the synthesis with concomitant growth in the population of larger NCs.

Measurements of aliquots extracted from the reaction mixture were repeated for several hours to determine the stability of the filtered reaction mixture. The results demonstrate the importance of measuring the reaction mixture within seconds of filtration, particularly during the beginning of the synthesis. The

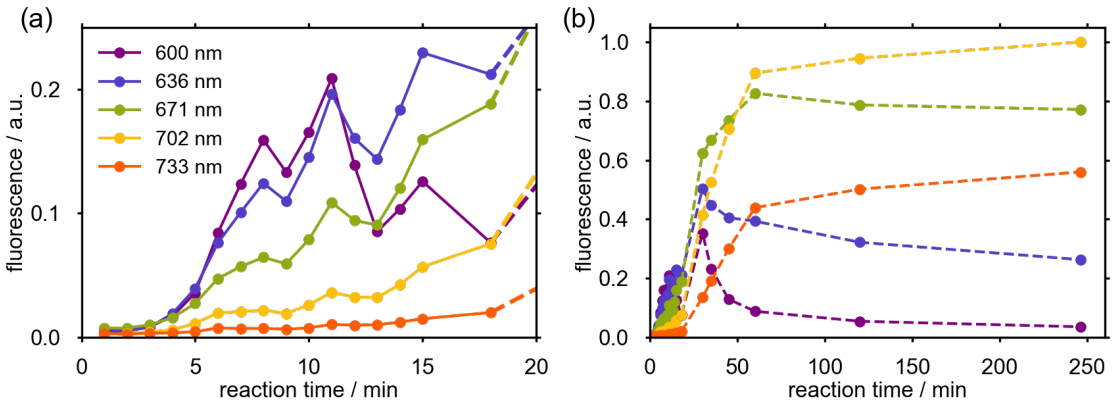

Figure 8. Growth of fluorescence features during synthesis. (a) The fluorescence intensity at 600 nm reaches a maximum after 11 min of reaction time. (b) The fluorescence at longer wavelengths continues to grow for the duration of the synthesis. Dotted lines indicate that the sample was centrifuged prior to measurement.

absorbance and emission spectra for the aliquots sampled after 7 min and 18 min of reaction time, Figure 9a and 9b, respectively, change significantly in the two hours after the reaction is 'quenched' by filtration. The aliquot filtered after 7 min of reaction time initially exhibits a single excitonic peak at 550 nm in the absorbance spectrum, but 10 min after filtering this peak starts to lose intensity and a peak at 592 nm begins to form. After two hours the 592 nm peak continues to grow and there is no longer any evidence of a peak at 550 nm. The overall optical density of the sample decreases, though in the same timeframe the fluorescence intensity nearly doubles.

Similar behavior is observed in the aliquot extracted and filtered after 18 min of growth. The initial absorbance shows a strong peak at 550 nm that disappears and a peak forms at 592 nm as the NCs continue to evolve after filtration. The fluorescence spectrum immediately following filtration exhibits features of similar intensity at 601 nm and 634 nm. Interestingly, while both

features grow after filtration, the higher energy peak becomes significantly larger. The emission spectrum also broadens to the red between the 40 and 120 min measurements. The negligible effect of the absorbance feature on overall NC fluorescence in these first two timepoints is most likely resulting from poor surface passivation by capping ligands. Excitons in these NCs recombine through predominantly non-radiative pathways owing to mid-gap trap states on surface atoms. Filtration does not remove the organic ligands or solid precursors that have already been solvated, hence NCs experience a small amount of continued growth and passivation after filtration.

The aliquot extracted, centrifuged, and filtered after 35 min of reaction time exhibits a strong peak at 592 nm with a shoulder near 630 nm, Figure 9c. The evolution of the absorbance and fluorescence spectra for this aliquot is more subtle than in earlier samples. The changes are even smaller for an aliquot extracted, centrifuged, and filtered after 4 h of reaction time, indicating that the species in this aliquot are the most persistent, Figure 9d. The decreasing spectral change as a function of reaction time can be rationalized as follows. It is likely that the species in the reaction mixture are inherently unstable at the beginning of a synthesis, since it is known that smaller NCs are more likely to dissolve back into precursor.[145] They may also not be as well capped by ligands. For the photophysics of these species to be accurately captured it is imperative that the measurement be conducted rapidly after filtration. The NCs in the reaction mixture at later stages of the synthesis are likely more stable. Smaller or poorly capped components of the reaction mixture may decrease in population during the brief time that the aliquot spends in the centrifuge prior to measurement. Additionally, the well-capped and more stable NCs are more likely to survive centrifugation and remain in the

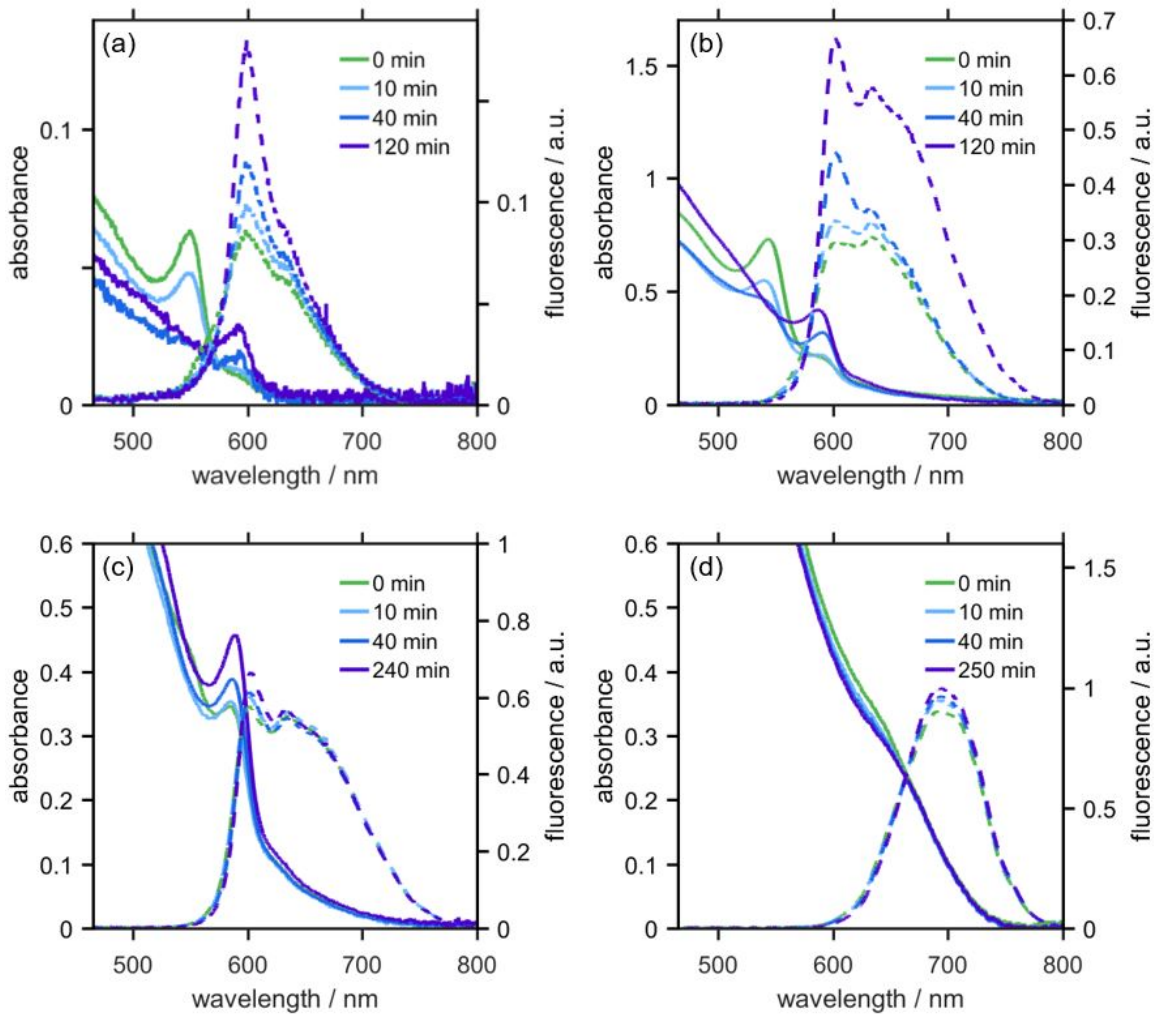

Figure 9. Absorption (solid) and fluorescence (dashed) of reaction mixture after growth for (a) 7 min, (b) 18 min, (c) 35 min, and (d) 4 hr. Spectra are collected at the indicated time after filtering (a,b) or centrifuging and filtering (c,d).

supernatant. It is likely that both the time spent in and action of the centrifuge bias the population towards more stable NC species. Aliquots that have been centrifuged, even if only for a short period of time, may no longer accurately reflect the full population of NCs that comprised the reaction mixture. This observation is of importance if an understanding of the photophysics during NC synthesis is sought, since quenching techniques that involve centrifuging are likely

to underrepresent the population of small and poorly capped NCs. The instability of nascent NCs is also likely to stymie attempts at structural characterization using transmission electron microscopy (TEM). Exposure to electron irradiation is known to cause structural damage to perovskite NCs, particularly for smaller NCs with a large surface-to-volume ratio.[103] In summary, I have adopted a solvation-mediated synthesis capable of manufacturing $MAPbI_3$ NCs on timescales more favorable to spectroscopic investigation than traditional methods. Modification of this technique to accommodate rapid sampling and filtration to quench the reaction allowed us to utilize a homebuilt spectrometer to simultaneously record absorption and fluorescence of NCs during nucleation and growth. The results show that synthesis occurs through a series of decreasingly quantum-confined, unstable intermediates that ultimately form fully grown NCs. The success of these experiments suggest any spectroscopic measurement, such as time-resolved electronic spectroscopy, must be completed in seconds to ensure the accurate measurement of the unstable species in the reaction mixture.

CHAPTER III

SURFACE LIGATION STAGE OF PEROVSKITE NANOCRYSTAL GROWTH REVEALED THROUGH POLARITY-DEPENDENT FILTRATION

Includes co-authored material from:

Sadighian, J. C.; Crawford, M. L.; Suder, T. W.; Wong, C. Y. Surface ligation stage revealed through polarity-dependent fluorescence during perovskite nanocrystal growth. *Journal of Materials Chemistry C* **2020**, *8*, 7041–7050.

3.1 Introduction

In the previous chapter I presented a kinetically favorable method for synthesizing $MAPbI_3$ on a timescale that permits spectroscopic investigation. I also described a rapid sampling technique that allows quick extraction and purification of NC aliquots, enabling absorbance and fluorescence measurements to be collected during growth. In this chapter I apply these to begin studying the mechanism by which perovskite NC surfaces become bound by ligands during growth. The classic model of NC formation proposed by LaMer comprises three discrete stages.[65,144,146,147] The precursor concentration must first increase until a critical supersaturation point has been reached. Self-nucleation then occurs until the precursor concentration has dropped below the critical nucleation concentration, at which point the newly-formed nuclei begin growing to form NCs. The duration of the self-nucleation stage is a key factor in determining the size distribution of the resulting NCs. Syntheses that follow a 'burst nucleation' mechanism aim to rapidly exceed the critical supersaturation point. Strategies include the rapid injection of a solution containing a high concentration of one of the precursors, rapidly lowering the temperature of the reaction, or adding a co-solvent in which the precursor is less soluble.[30,31,39,142,148–151] Following nucleation,

the rate of growth for some NCs can be described as a function of precursor diffusion,[144,147] but for other NCs the growth stage may be more complicated. Recent work suggests that the perovskite crystal structure is not fully formed at the beginning of this growth period, instead existing as a plumbate complex with cations (methylammonium, formamadinium, cesium, etc.) still diffusing into the lattice.[68,143,152,153] Additionally, Ostwald ripening, where smaller NCs are re-solubilized and consumed by more stable, larger NCs, can cause defocusing of the size distribution.[154–157] The surface plays a significant role in the nucleation and growth of NCs.[158–162] Understanding the surface is key for understanding the electronic structure, function, and growth of NCs owing to their large surface-to-volume ratios. Surface ligands are commonly used to prevent aggregation and passivate electronic trap states that arise from dangling bonds at unoccupied surface sites.[33,34,162] These trap states occupy energy levels between the HOMO and LUMO bands and significantly reduce NC fluorescence quantum yield. One possible model of NC surface evolution during formation is illustrated in Figure 10a, where the NCs after the nucleation event are well-passivated while they continue to grow. During this process, the decreasing quantum confinement causes a redshift in the fluorescence spectrum. Recently, a terminal stage of colloidal NC formation has been proposed after the NCs have completed their growth.[62] The redshift of the fluorescence spectrum and the increase in fluorescence intensity typically ascribed to the growth stage are instead shown to result from increased passivation of NCs by ligands attaching to dangling bonds on the NC surface, Figure 10b. Classical nucleation and growth can also be followed by a secondary nucleation event wherein small, poorly-capped NCs from the first growth stage aggregate, Figure 10c.[66] For NCs that exhibit aggregative nucleation and growth

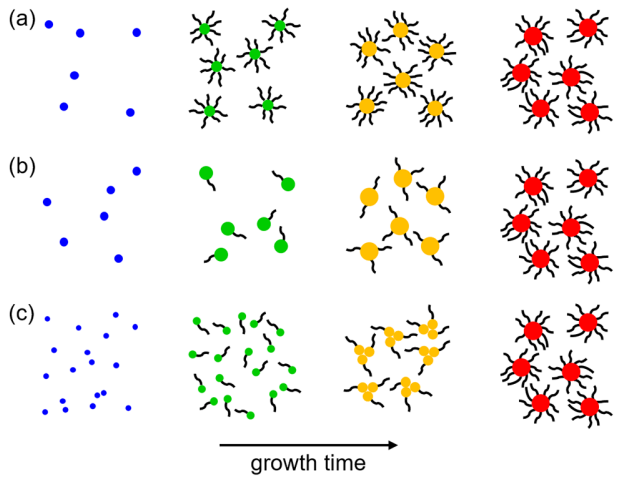

Figure 10. Models of the NC surface during growth. (a) The surfaces of nascent NCs are well-capped throughout growth. (b) Nascent NCs are poorly-capped during growth, only becoming well-capped in a distinct surface ligation stage near the end of NC formation. (c) Aggregative nanocrystal growth wherein smaller, poorly-capped NCs aggregate to form a larger NC. © The Royal Society of Chemistry.

following classical nucleation and growth, it is the aggregative nucleation stage that determines the final nanocrystal size distribution. While these mechanisms have been observed and rigorously studied in chalcogenide NCs[163–169] and other systems,[170–174] additional measurements are required to determine which, if any, of these models can be used to accurately describe the surface during the formation of hybrid perovskite NCs. Tracking NC absorbance and emission spectra is a quick, simple, and effective way to monitor NC growth and passivation.[175] The decrease in quantum confinement as the NC diameter increases causes a red shift in their band edge absorbance and fluorescence. Additionally, increased emission intensity indicates the passivation of surface trap states by capping ligands.[34,62,176,177] The most common method of sampling NCs during growth involves sequentially extracting aliquots of the reaction mixture and centrifuging each sample for several minutes to remove solid reactants, quenching the reaction and minimizing

sources of scatter. The absorbance and fluorescence of these samples can then be measured.[30,31,36,42,48,152,153,178] However, during centrifugation individual NCs can continue to grow or dissolve back into precursors, and the fractional passivation of their surface by ligands can change. As a result, this sampling method fails to provide an accurate snapshot of the NCs and their surface during growth.
In situ spectroscopic measurements of CdSe NCs have been conducted using a transmission-reflectance dip probe, removing the sampling problem.[137] This technique is most effective when measuring reaction mixtures without an excess of solid precursor so scatter at the tip of the probe is minimal. Fluorescence measurements during growth require that the reaction mixture be sequentially sampled, and for a typical fluorimeter configuration the sample must be diluted to prevent inner-filter effects. While this may not negatively affect NCs with a stronger lattice, such as CdSe NCs, dilution causes hybrid perovskite NCs to exfoliate into nanoplatelets, radically altering their electronic properties.[179] The soft lattice of hybrid perovskites also limits the utility of in situ TEM measurements during NC growth, as even fully grown, stable perovskite films and NCs may be damaged by the electron beam during TEM.[103,180,181] In situ measurements of absorbance, fluorescence, and small-angle X-ray scattering (SAXS) using microfluidic reactors[182–184] also provide insight, but these measurements occur under conditions that do not represent those found in a typical wet-lab synthesis.
Perovskite NCs are typically synthesized using either ligand-assisted reprecipitation (LARP)[30–32] or hot-injection[149] techniques, where nuclei are produced rapidly via burst nucleation[65,66,144,185] and subsequent NC growth can be complete in a matter of seconds to minutes. In these conventional synthetic methods, nucleation occurs in an environment that includes extreme temperature and/or concentration

gradients, introducing sources of inhomogeneity to the nuclei and resulting NCs, limiting the scalability of the reaction. A non-polar solvent that reduces the solubility of the polar precursor salts can be used to increase homogeneity in the reaction mixture during nucleation and growth. Small amounts of organic ligand can then serve to mediate the synthesis by solvating the precursor, making it available for nucleation. This solvation step limits the rate of the reaction, allowing the reaction to be well-mixed during the formation process. This increases the homogeneity of the reaction environment, improves reaction scalability, and substantially increases the number of measurements that can be made during NC growth.[186] In this chapter, I measure absorbance and fluorescence of the reaction mixture during a ligand-mediated synthesis of $MAPbI_3$ NCs. Since the lead iodide and methylammonium iodide precursors are insoluble in the non-polar solvent, aliquots of the reaction mixture contain suspended solids that can scatter light and interfere with spectroscopic measurement. Centrifugation can remove these solids, but the species in the sample may evolve during this procedure. To decrease the delay time between aliquot removal and measurement, I use syringe filters to quickly remove solid components from the reaction mixture. The absorbance and fluorescence of sequentially extracted aliquots of the reaction mixture show the evolution of the species within the mixture and their dynamic electronic structure. Additional insight into the physical and electronic structure of the nuclei and growing NCs is gained by comparing measurements of the reaction mixture after it passes through filters of different polarities. These experiments show that the formation of hybrid perovskite NCs includes a surface ligation stage that increases NC stability and photoluminescence.

3.2 Methods

3.2.1 Materials

All reagents were used as received: lead iodide (99.999%, trace metals basis, Sigma-Aldrich), methylammonium iodide (MAI, ≥99%, anhydrous, Sigma-Aldrich), octylamine (99%, Sigma- Aldrich), oleic acid (90%, technical grade, Sigma-Aldrich), and hexane (≥95%, laboratory reagent grade, Sigma-Aldrich).

3.2.2 Synthesis

350 mg of PbI_2 and 95 mg of MAI were combined with 40 mL of hexane in a glass test tube and suspended in an ultrasonication bath to provide constant mixing of the precursors. The reaction was initiated with the addition of 100 μL octylamine and 200 μL oleic acid. A recirculating chiller in a closed-loop configuration with an aluminum block was used to maintain a temperature of 22 ℃ in the ultrasonication bath.

3.2.3 Sampling and Characterization

HDPE syringes were used to withdraw two separate 0.6 mL aliquots of reaction mixture at discrete time points. One of each aliquot was filtered through a 0.45 μm syringe filter (VWR) with either a polytetrafluoroethylene (PTFE) or nylon membrane and into a 1 mm path length quartz cuvette (Starna Cells, 1-Q-1). Following the 25 minute mark a 1.0 μm PTFE pre-filter (Whatman Rezist) was used in conjunction with the 0.45 μm filter. Following 60 minutes an additional 5.0 μm filter (Whatman Rezist) was also added. 2 mL of reaction mixture was used for these aliquots.

3.2.4 Absorbance and Fluorescence Measurements

$MAPbI_3$ NCs were synthesized via a solvation-mediated synthesis previously reported.[48,187] Two aliquots of the reaction mixture were extracted at 16 discrete

time points during five separate syntheses. Each aliquot was filtered through either a PTFE or nylon membrane syringe filter into a 1 mm path length cuvette. This removed solid precursors that cause scatter, enabling nearly in situ absorbance and fluorescence measurements using a homebuilt instrument, Figure 6. Spectra measured for aliquots extracted at the same time points during the five separate syntheses were averaged, shown in Figure 13. The standard deviation in the spectra at four selected time points is indicated by the shaded region. The standard deviation for all time points is shown in Figure 14. Further information regarding the reagents, synthesis, and sampling may be found in the supplemental information.

3.2.5 Transmission Electron Microscopy

TEM images were obtained with an FEI Titan 80-300 kV STEM equipped with a Cs image corrector operating at 300 kV. NCs were grown for 120 minutes and then filtered through either PTFE or nylon filters into HDPE centrifuge tubes for transport. Sample preparation involved diluting by a factor of 2x with hexane before being immediately drop-cast onto lacey carbon TEM grids with an ultrathin carbon support film. No additional sample preparation was used prior to imaging. 540 particles were counted and used for statistics on PTFE-filtered NCs, while 592 particles were counted for nylon-filtered NCs.

3.3 Results and Discussion

3.3.1 Transmission Electron Microscopy

Figure 11 shows TEM characterization of NCs grown for 120 minutes, equalling the longest reaction time used in any of our experiments. A high-angle annular dark-field scanning transmission electron microscopy (HAADF-STEM) image of NCs filtered through PTFE is shown in Figure 11a, whereas a bright-field

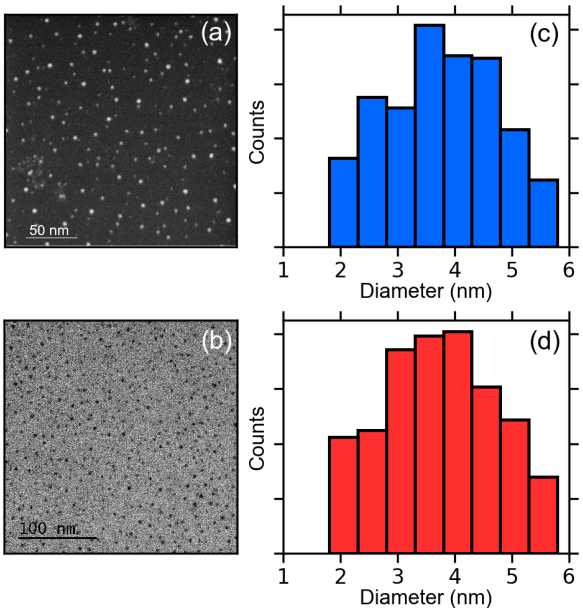

Figure 11. TEM characterization of PTFE-filtered (a,c) and nylon-filtered (b,d) NCs after 120 minutes of growth. Image of PTFE-filtered NCs was taken in HAADF-STEM (a), nylon-filtered NCs were imaged in bright-field TEM (b). Size distribution information shows both NC populations have an average size of 3.7 nm (nPTFE=540, nnylon=592). © The Royal Society of Chemistry.

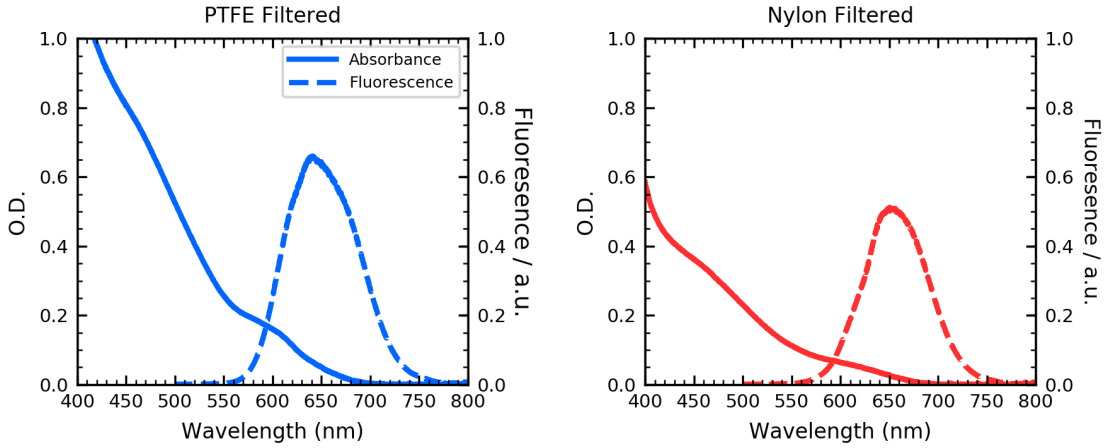

Figure 12. Absorbance (solid) and fluorescence (dashed) of NCs grown for 120 minutes and analyzed with TEM. © The Royal Society of Chemistry.

image of NCs filtered through nylon is shown in Figure 11b. The two samples of NCs exhibit similar circularities of 0.92±0.20 and 0.93±0.03 for PTFE- and nylon-filtered NCs, respectively. This is in agreement with previous literature reports that this synthesis produces highly spherical nanoparticles.[48] Filter material is shown to have little effect on the size of particles in the filtrate, Figure 11c,d, as filtration through PTFE and nylon each result in NCs with an average size of 3.7 nm ± 1 nm. While TEM is commonly used to characterize NCs, rinses with anti-solvent and centrifugation are typically required to remove superfluous organic ligand before imaging, particularly at the high magnifications necessary for accurate size quantification. Without these steps, images suffer from poor contrast and uneven background intensity as the ligands polymerize under the high energy beam and deposit onto the TEM grid. The perovskite NC solutions may change as a result of these preparatory procedures, yielding TEM images that may not accurately reflect the original population.[188] Further, it is known that TEM causes irreversible damage to perovskite thin films.[180,189,190] Since the surface plays a central role in degradation,[191,192] the large surface-to-volume ratio of perovskite NCs renders them highly susceptible to damage during TEM measurements.[103,180,181] Consequently, unstable nascent NCs may degrade too quickly for reliable imaging and characterization. Rapid, non-destructive characterization techniques, such as optical spectroscopies, are necessary to study NCs sampled and filtered during early stages of nucleation and growth, when nascent, growing NCs are unstable.

3.3.2 Absorbance and Fluorescence Measurements

Aliquots filtered through the PTFE filters exhibit absorbance at 375 nm after 3 minutes (Figure 13). This is attributed to plumbate complexes that form at the beginning of $MAPbI_3$ syntheses.[143] The solution appeared to reach

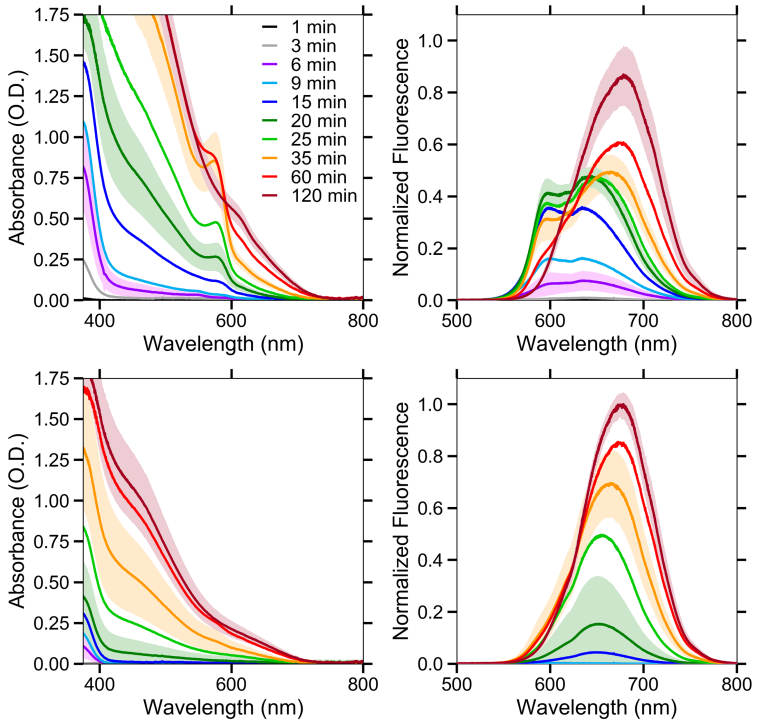

Figure 13. Absorbance (left) and fluorescence (right) of reaction mixture filtered through PTFE (top) or nylon (bottom). Traces represent an average of 5 syntheses with shaded areas showing standard deviations for selected time points. © The Royal Society of Chemistry.

the critical nucleation threshold within the first 3 minutes, as indicated by the appearance of a broad fluorescence feature centered near 640 nm. The fluorescence intensity continued to grow over the first few minutes, alongside the onset of broad absorbance extending to 600 nm. After nine minutes of reaction time, two distinct peaks at 545 and 585 nm appeared in the absorbance spectrum and at 600 and 650 nm in the fluorescence spectrum. The fluorescence intensity continued to increase until 20 minutes of reaction time, at which point the 600 nm peak began to lose intensity and the spectrum started to redshift. This corresponded with the disappearance of the absorbance feature at 545 nm and a rapid increase in absorbance at 585 nm. The intensity of the 585 nm absorbance reached a

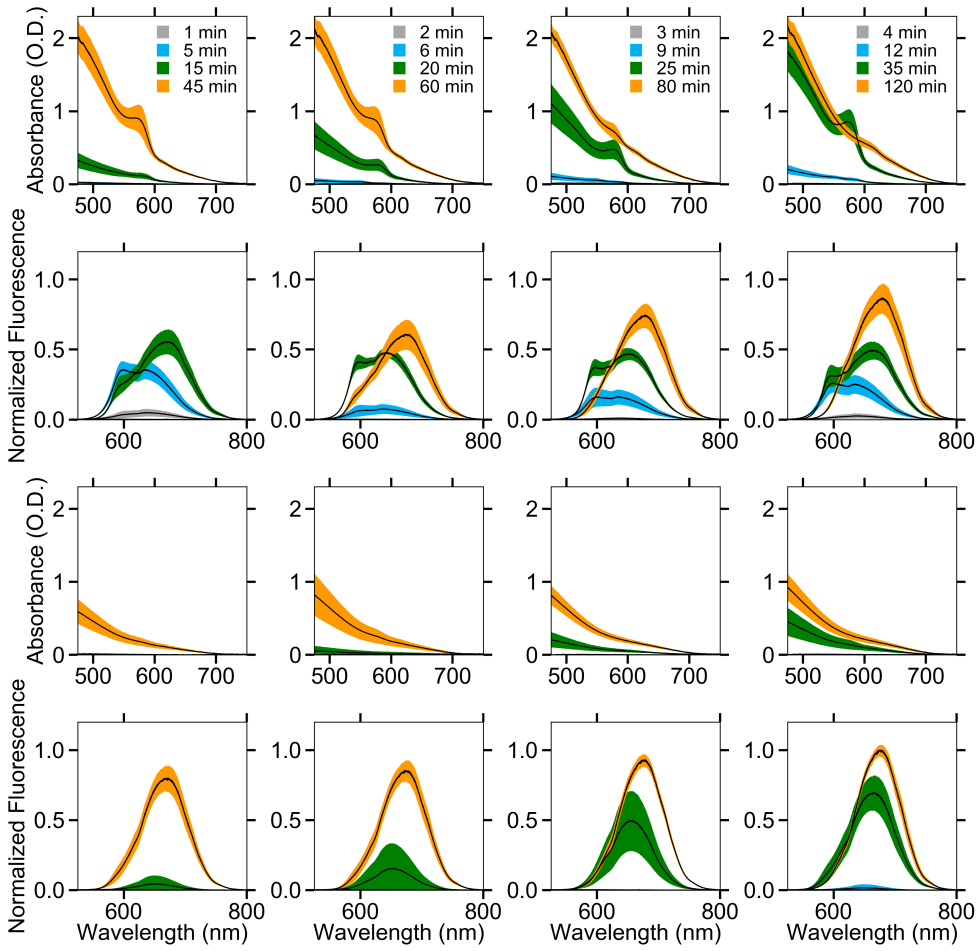

Figure 14. Average absorbance and fluorescence of five syntheses (lines) and their standard deviations (shaded), analogous to Figure 13. Absorbance and fluorescence of PTFE-filtered NCs shown in rows 1 and 2, respectively, absorbance and fluorescence of nylon-filtered NCs shown in rows 3 and 4, respectively.

maximum after 35 minutes of growth, then began to lose intensity while the band-edge absorbance shoulder at 635 nm exhibited significant growth. I attribute the absorbance at 635 nm to larger NCs that only weakly confine an exciton.

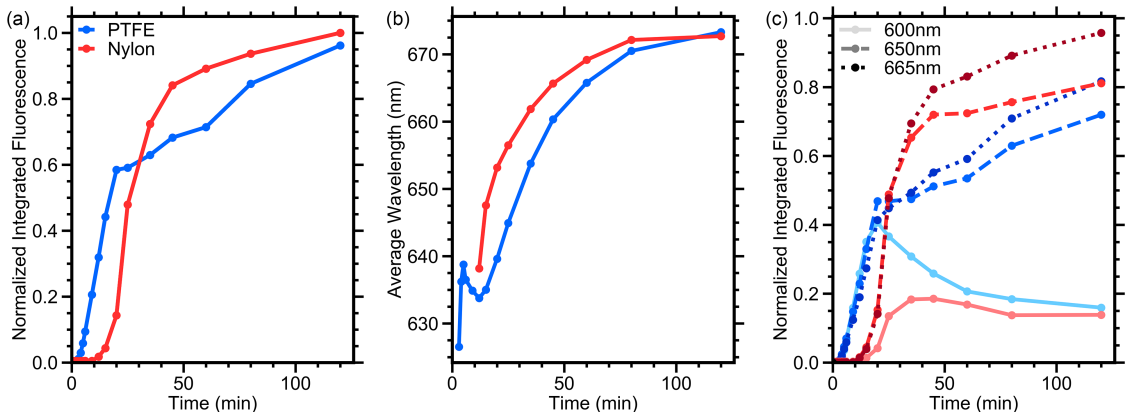

Figure 15. Comparison of fluorescence spectra for perovskite NCs during formation after filtering through PTFE (blue) or nylon (red). (a) Integrated fluorescence intensity. (b) Average emission wavelength. (c) Normalized fluorescence intensity at 600 nm (solid), 650 nm (dashed), and 665 nm (dotted).

Meanwhile, the fluorescence peak at 600 nm weakened substantially and the overall spectrum became significantly more unimodal. The spectrum continued to redshift and increase in intensity during the final hour of the synthesis. NC samples filtered through polar nylon membranes produced starkly different absorbance and fluorescence spectra, particularly during the beginning of NC formation. At early reaction times there was significantly less absorbance from plumbates, as these were more effectively removed by the polar nylon membrane. Emission was not detected until after 15 minutes of growth, when a weak and broad peak centered close to 650 nm was detected, characteristic of $MAPbI_3$ NCs that are only weakly confining the exciton, as opposed to the two peaks observed at 600 nm and 650 nm for NCs filtered through PTFE after an equivalent growth time. This suggests that the polar nylon filter removed the smaller NCs that would exhibit fluorescence at shorter wavelengths. Thus, I conclude that the smaller NCs must be poorly-capped by organic ligands. The exposed NC surface is polar and more likely to be adsorbed

to the nylon filter. The intensity of the fluorescence spectrum grew rapidly and redshifted slightly between 15 and 35 minutes for the nylon-filtered samples. This corresponded to the beginning of the redshift observed in the fluorescence of PTFE-filtered NCs, although those spectra showed little change in overall intensity during the same time period. Following 35 minutes, the fluorescence of nylon-filtered NCs continued to gain intensity and redshift. The absorbance tail at 635 nm, which I ascribe to larger NCs, first appeared in nylon-filtered NCs after 20 minutes of growth and proceeded to slowly increase for the rest of the synthesis. Although this feature increased in intensity throughout the experiment, up to the last measurement at 120 minutes, the optical density was still much lower than in the NCs filtered through PTFE. However, despite the weaker absorbance, NCs filtered through nylon exhibit much stronger fluorescence with a narrower line shape than those filtered through PTFE. This is further evidence that filtration by a nylon membrane removes poorly-capped NCs that contribute to absorbance but not fluorescence. Plotting the integrated fluorescence at each time point revealed stark differences in the rate of intensity increase for NCs filtered through either PTFE or nylon, Figure 15a. PTFE-filtered NCs showed a sharp, linear increase in integrated fluorescence during the first 20 minutes of the reaction. Following 20 minutes there was a distinct change in the rate of intensity increase, though it remained linear. The change in integrated fluorescence intensity of nylon-filtered NCs during growth was sigmoidal, with an onset that was delayed until 15 minutes. The integrated fluorescence intensity of the nylon-filtered NCs increased rapidly and exceeded that of the NCs filtered through PTFE after 30 minutes. The rate of increase in fluorescence intensity slowed significantly after 50 minutes. Figure 15b shows the average fluorescence wavelength at each time point during NC growth. Immediately

after fluorescence was detected from the PTFE-filtered sample the spectrum began to redshift. As the 600 nm peak reached its maximum intensity after 20 minutes of growth, a slight blueshift in the average wavelength was observed as the intensity of the 600 nm peak overtook that of the lower energy 650 nm peak. This suggests that during this early stage of NC formation the population of small NCs that fluoresce at 600 nm grew faster than the population of larger NCs that fluoresce at 650 nm. Concurrently, the nylon-filtered sample began to exhibit detectable fluorescence after 15 minutes of growth that was redder than that of the PTFE-filtered sample. As the reaction proceeded until the final measurement at 120 minutes, the average emission wavelength for both samples approached 675 nm, typical for weakly-confined excitons in $MAPbI_3$ NCs. Figure 15c shows the increase in fluorescence intensity during NC growth for the features at 600 nm, 650 nm, and 665 nm. The fluorescence of the PTFE-filtered samples at these three wavelengths increased initially at a similar rate. After 20 minutes of growth the fluorescence intensity at the three wavelengths began to diverge, providing insight into the source of the inflection point shown in 15a. The peak at 600 nm reached its maximum at 20 minutes before it started to decay, indicating that this species is being consumed by the formation of new, redder emissive nanoparticles. This could be due to aggregative growth or a coalescence/ripening process wherein particles dissolve and are consumed by larger particles that continue to grow. The fluorescence intensity measured at 650 nm most closely mimicked the integrated fluorescence intensity in the PTFE-filtered sample, Figure 15a, and continued to increase linearly, though at a slower rate than during the first 20 minutes of NC growth. The rate of increase in the fluorescence intensity at 665 nm slowed after 20 minutes of growth, but the intensity grew faster at 665 nm than at 650 nm, since

the broad feature that spanned this wavelength range redshifted as its intensity increased. In contrast to the linear increase in fluorescence intensity measured in the PTFE-filtered NCs, the fluorescence intensity of NCs filtered through nylon did not begin to increase significantly until after 10 minutes of NC growth, and then increased sigmoidally. The fluorescence line shape of NCs filtered through nylon did not include a peak at 600 nm, so the increase in fluorescence intensity measured at this wavelength was instead a result of the broad feature centered at 650 nm. The rate of increase in fluorescence intensity at 650 nm and 665 nm was similar to that measured in PTFE-filtered NCs, with the fluorescence intensity at the redder wavelength increasing faster, again indicating that the fluorescence feature spanning this wavelength range was redshifting as it increased in intensity.

3.3.3 Nanocrystal Aging and Degradation

Analyzing the stability of the nascent NCs at different stages of growth provides deeper insight into the composition of these transient species. Aliquots of the reaction solution were extracted after 15, 35, and 120 minutes of growth and immediately filtered through a PTFE or nylon filter, Figure 16 and Figure 17, respectively. I measured the absorbance and fluorescence spectra of each solution at a series of time points after filtration, which are termed the 'age' of the NCs post-filtration. Figure 16a,c,e shows the fluorescence of PTFE-filtered NC solutions as they aged. After 15 minutes of growth the emission spectrum measured immediately after filtration exhibited two peaks. Six minutes after filtration, the intensity of the blue edge of the fluorescence spectrum (<580 nm) had decreased. As the solution continued to age, the portion of the blue edge of the spectrum that decreased in intensity widened, up to 585 nm after 40 minutes and up to 590 nm after 120 minutes of aging. This is more clearly visualized by plotting the difference

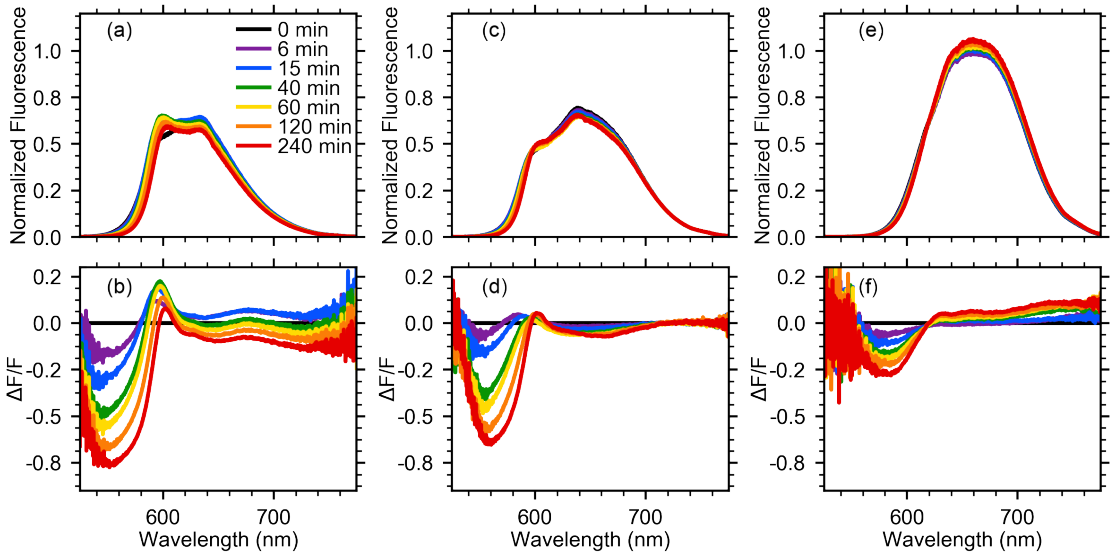

Figure 16. Aging of perovskite NCs grown for 15 (a,b), 35 (c,d), and 120 (e,f) minutes after filtering through PTFE, monitored by fluorescence (a,c,e) and normalized differential fluorescence (b,d,f). Fluorescence of filtered reaction mixture was re-measured at several ages post-filtration to observe how the NCs changed over time. Differential fluorescence spectra are the difference between the emission spectrum at each post-filtration time point and the spectrum recorded immediately following filtration, normalized by the intensity of the fluorescence spectrum immediately following filtration.

between the fluorescence spectra collected during aging and the spectrum measured immediately after filtration, Figure 16b. This plot indicates that the smallest NCs in the solution were the least stable and dissolved back into precursors. While the blue-edge of the spectrum receded, the red-edge of the fluorescence feature centered at 600 nm and the broader fluorescence peak at 635 nm grew. I ascribe these spectral changes to Ostwald ripening, whereby the precursor and ligand that are liberated when the smaller NCs dissolve are recruited into the larger NCs, enabling them to grow and become better passivated. However, all of these features eventually receded as the NCs continued to age, indicating that after only 15 minutes of growth even the largest NCs in the reaction mixture were unstable.

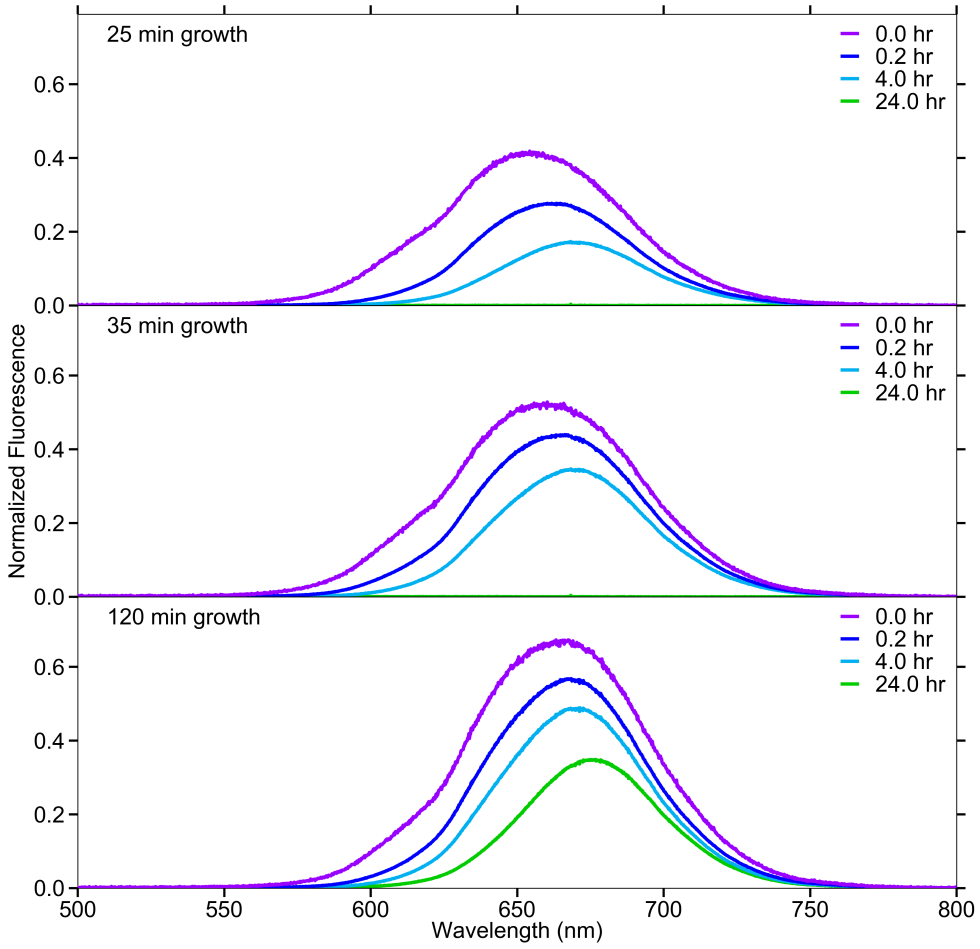

Figure 17. Fluorescence spectra measured during aging of NCs filtered through nylon after 25 minutes (top), 35 minutes (middle), and 120 minutes (bottom) of growth. Unlike NCs filtered through PTFE, all samples filtered through nylon exhibit similar aging regardless of growth time. We attribute this to the polar nylon filter removing significant amounts of free organic ligand, disturbing the equilibrium and causing weakly bound octylamine to detach from the surface over time, destabilizing the NCs.

In addition to the higher solubility of small NCs, these nascent NCs are likely also poorly-capped by organic ligands, as suggested by the lack of detectable

emission from these samples after filtration with a polar nylon filter, Figure 13. There was markedly less change in the fluorescence spectrum during the aging of NCs grown for 35 minutes, Figure 16c,d compared to that of NCs isolated after only 15 minutes of growth, indicating that the more mature NCs exhibited increased stability. The primary fluorescence peak was slightly redshifted to 638 nm owing to the longer growth time. The fluorescence spectrum was more stable and did not lose as much intensity over the 240 minutes of aging. The shoulder on the high-energy side of the spectrum redshifted as the NCs aged and underwent Ostwald ripening. However, unlike the spectrum in Figure 16a, the intensity of this fluorescence peak did not decrease. The spectral changes during aging of the NCs following 35 minutes of growth were smaller than those during the aging of the NCs grown for only 15 minutes, since fewer unstable small and poorly-capped NCs remained after the increased growth time. The increased stability of NCs that have grown to be larger and better capped is supported by the observation of emission in the nylon-filtered reaction solution after 35 minutes of growth. NCs that have grown for 120 minutes, the full length of our experiment, are significantly more stable than earlier NC samples, Figure 16e,f. Over the first two hours of aging the spectrum lost intensity on the high energy shoulder and the primary peak continued to grow in intensity and redshift slightly, which are again ascribed to Ostwald ripening. During the four hours of aging the NC fluorescence continued to gain intensity, which I interpret as continued improvement in NC passivation by organic capping ligands. Comparing the magnitude of the fluorescence changes during aging in Figure 16b,d,f, clearly indicates that the NCs continued to become more stable during growth. Two stages of NC formation, each with a distinct rate of increase in fluorescence intensity, are shown in Figure 13a. The measurements

during the aging of the sample extracted after 15 minutes of growth indicate that NCs were unstable during the first stage of growth, Figure 16a,b. After proceeding to the second stage of formation, the NCs were more stable, as demonstrated in the fluorescence spectra measured during the aging of NCs after 35 and 120 minutes of growth, Figure 16c-f. This suggests that the structural changes during the second stage of formation, after 20 minutes in the case of this particular reaction, result in a dramatic improvement in stability. This could be owing to the NCs exceeding a size threshold beyond which they were insoluble, or that the surface ligation of the NCs was increasing. The rapid increase in fluorescence intensity measured in samples that can pass a polar nylon filter during the second formation stage suggests a change in the polarity of the NC surface. Thus, surface ligation is likely occurring during the second stage of NC formation. This may also be accompanied by continued NC growth, as suggested by the continuing redshift of the primary fluorescence feature. TEM characterization in Figure 11 supports this final ligation process, as there is no difference in the average size of the NCs that pass through either PTFE or nylon filters. Thus, any difference in the fluorescence must be owing to changes in surface passivation. The distinct change in the rate of fluorescence intensity increase after 20 minutes of growth in the PTFE-filtered NCs and the simultaneous appearance of detectable fluorescence intensity in the nylon-filtered samples suggests that the beginning of the surface ligation stage was a distinct point in the reaction at which some threshold was crossed. It is possible that the free energy of the NC surface depends on its curvature, changing the equilibrium between bound and unbound ligands as the NCs grow. Further experiments will be needed to validate this hypothesis.

3.3.4 Dilution Studies of NC Aggregation

As illustrated in Figure 10c, one possible mechanism for NC formation is aggregative growth. In this mechanism small, poorly-capped NCs nucleate to form NC aggregates, and these aggregates then undergo rearrangement to fuse into one larger NC. To determine if the second stage of NC formation observed in this reaction is aggregative nucleation and growth I diluted NC samples filtered at various stages of growth. If aggregative nucleation occurred at 20 minutes, initiating the second growth stage, dilution of a sample filtered after 20 minutes of growth would cause these newly formed aggregates to break apart into the smaller precursor NCs that existed at the end of the first stage of formation. The fluorescence spectrum of the PTFE-filtered sample grown for 20 minutes did change upon dilution, Figure 18a. The intensity ratio of the shoulder at 600 nm to the main peak increased, indicating a shift back to the NC species dominant at shorter reaction times. This was not observed in the PTFE-filtered samples grown for 35 minutes, suggesting increased stability, Figure 18b. This could either indicate that the measured species after 20 minutes of growth were NC aggregates that were broken apart by dilution, or that the NCs were poorly-capped, unstable, and susceptible to Ostwald ripening, particularly after dilution changed the ratio of bound:unbound ligand to remove even more ligands from the NC surfaces. If the distinct growth stage observed 20 minutes into the reaction was indeed aggregative nucleation, an aliquot filtered through nylon at that time would consist of newly formed aggregates with capped surfaces. Dilution of this sample should then exhibit the fluorescence features of NCs during the first stage of formation after filtration through PTFE, since the newly exposed NC surfaces would be poorly-capped. The emission spectra in Figure 18c exhibited neither a blueshift nor the

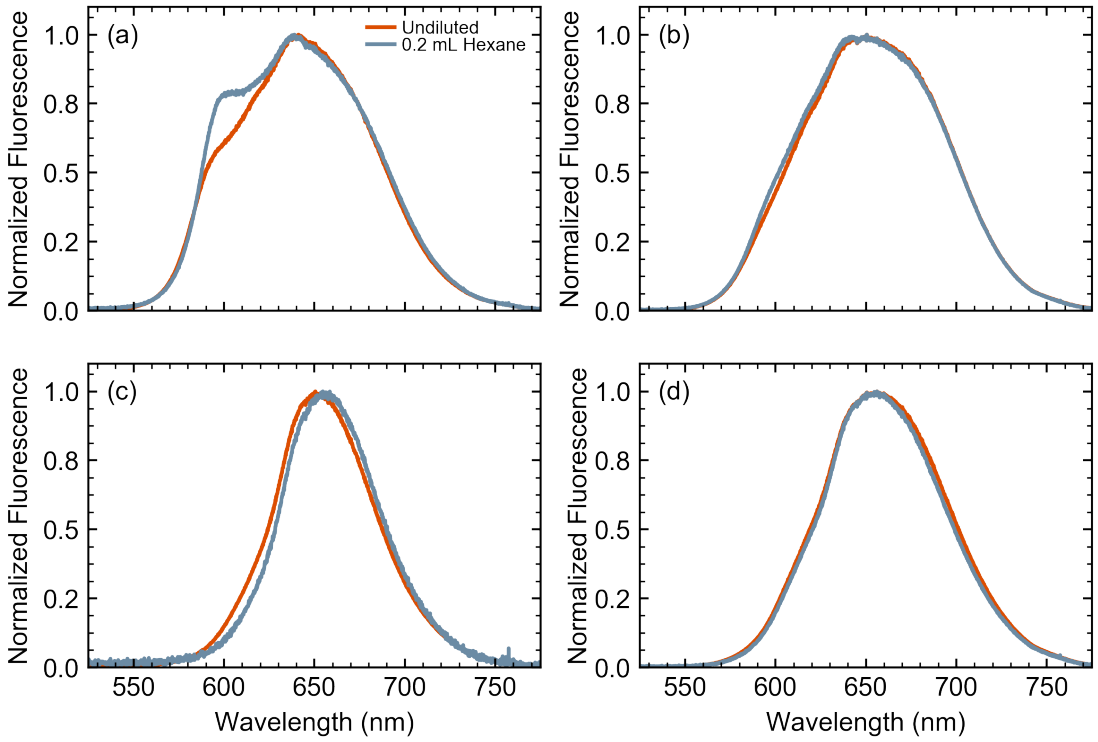

Figure 18. Spectra before (orange) and 1 minute after (blue) diluting 0.07 mL of filtered reaction mixture with 2 mL of hexane. PTFE-filtered NCs grown for 20 minutes (a) and 35 minutes (b) pictured at top. Nylon-filtered NCs grown for the same time points (c,d) shown at bottom. The absence of a feature at 600 nm after dilution of nylon-filtered NCs indicates that the change in rate of fluorescence intensity increase after 20 minutes of growth is not the result of an aggregative nucleation process.

reappearance of the 600 nm peak. This indicates that aggregative nucleation was not responsible for the observed second stage of NC formation. A previous fluorescence study of formamidinium lead halide NCs showed that NCs during the early stages of growth exhibit sharp, high energy fluorescence peaks attributed to formation of nanoplatelets (NPTs) as intermediates.[184] These spectral features are very similar in nature to the fluorescence I observed during our reactions. It is possible that the species I observed during the first stage of NC formation are

poorly-capped NPTs that can be adsorbed to nylon filters. If NCs were formed by the aggregation of these NPTs, I would expect dilution to break the aggregates back into NPTs, which was not observed.

3.4 Conclusion

Our results demonstrate that sub-populations of NCs can be selected based on their surface properties through choice of filter material. Applying this to a solvation-mediated synthesis has enabled spectroscopic investigation of nucleation and growth during a perovskite NC synthesis. The data suggest that in this type of reaction NCs exhibit classical, non-aggregative growth, potentially via a series of NPT intermediates, with a final surface ligation phase where poorly-capped NCs become well-passivated by surface ligands. TEM images that show NC populations with identical size and morphology distributions but different fluorescence intensities lend further evidence to the existence of this final ligation stage. The presented approach to sampling a reaction mixture during a NC synthesis opens the door for the application of time-resolved spectroscopies to the study of perovskite NCs during synthesis, which will provide further insight into the mechanism by which these NCs form. Future work will involve examining how NC electronic structure is affected by changing reaction conditions during different stages of NC formation, providing a deeper understanding of the emergence of NC photophysics.

CHAPTER IV

EVOLVING STARK EFFECT DURING GROWTH OF PEROVSKITE NANOCRYSTALS MEASURED USING TRANSIENT ABSORPTION

Includes co-authored material from:

Sadighian, J. C.; Wilson, K. S.; Crawford, M. L.; Wong, C. Y. Evolving Stark Effect During Growth of Perovskite Nanocrystals Measured Using Transient Absorption. *Frontiers in Chemistry* **2020**, *8*, 897.

4.1 Introduction

The quality of the NC surface during growth is still poorly understood and the timescales of nucleation and growth are prohibitively short for investigation using typical surface-specific characterization techniques, such as X-ray photoelectron spectroscopy[193], electron energy loss spectroscopy[194], small-angle X-ray scattering[195], and 2D nuclear magnetic resonance techniques[59]. The previous chapter used linear spectroscopic measurements to provide evidence for a discrete surface-ligation stage in the growth of $MAPbI_3$. These experiments revealed that NCs initially grow in size while their surfaces remain poorly-capped by passivating ligands, and do not become well-capped until they are almost fully grown (Figure 19).[63] These visible absorbance and fluorescence measurements report on transitions from the ground and emissive band-edge states, respectively. The peak positions and lineshapes can provide insight into the NC size distribution, and fluorescence intensity is often used to infer the degree of NC surface passivation. However, these spectroscopies are insensitive to other important transitions, such as carrier trapping and non-radiative recombination, and the dynamics of the excited carriers. Here, I use SSTA to confirm this process by probing the presence of electronic traps on the NC surface during growth. Surface atoms lacking bonds to

capping ligands exhibit localized electronic states with energies that can lie within the band gap. These mid-gap states act as traps for excited electrons or holes, suppressing radiative recombination and hampering performance in light emitting devices[34]. Time-resolved non-linear spectroscopy provides a way to confirm the proposed surface ligation stage by observing photophysical signatures indicative of charge carriers becoming trapped in these surface states. A comprehensive understanding of how NC photophysics evolves during synthesis may provide deeper insights into NC growth mechanisms, the nature of the NC surface, and how a synthesis can be tuned to achieve desired morphologies and optoelectronic properties.

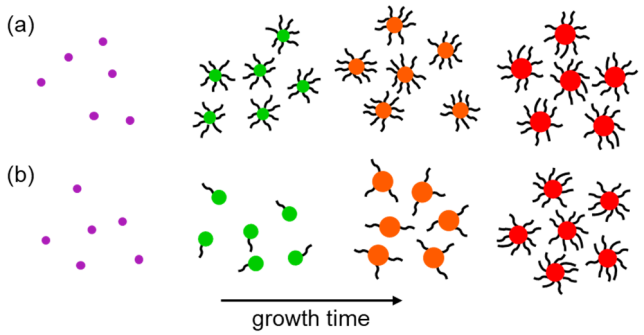

Figure 19. Schematic of NC growth. (a) Following LaMer nucleation the immature NCs are well-capped by surface ligands throughout most of their subsequent growth. (b) Nascent NCs nucleate following the same LaMer-type mechanism, but surface ligation occurs primarily after NC growth. A terminal ligation stage is proposed in literature for CdSe and $MAPbI_3$ NCs and is supported by the measurements in this work. © Sadighian, Wilson, Crawford, and Wong.

In this chapter, I demonstrate a technique that can provide further insight into the evolving NC surface by probing the electric field generated by carriers localized at surface traps. Photogenerated electron-hole pairs become spatially separated when a carrier is trapped at these surface sites, creating an electric field inside the NC. The presence of an electric field can modulate the optical transitions

of an NC *via* the Stark effect[196–199]. Analysis of the modulated absorbance spectrum lineshape can provide insight into the electric fields in the NCs[200]. The quantum-confined Stark effect (QCSE) changes the bandgap transition energy by shifting the electron and hole energy levels[201]. This typically redshifts the bandedge absorption and causes the differential absorbance spectrum to exhibit the lineshape of the first derivative of the linear absorbance. In systems that lack any specific orientation, such as randomly distributed surface traps on NCs, the internal electric field generated by spatially separated, trapped carriers results in a population of randomly oriented dipoles in the sample. This would act to inhomogenously broaden the overall transition, and as a result the differential absorbance spectrum would resemble the second derivative of the linear absorbance[202,203].

Electroabsorbance measurements of 2D hybrid perovskites have exhibited lineshapes that could be fit to a weighted sum of first and second derivatives of the absorbance spectrum[203]. These two components were assigned to a spectral redshift arising from a QCSE and broadening due to loosely-bound, screened electron-hole pairs, respectively. This same lineshape was observed upon photogeneration of charge carriers in these perovskites during transient absorption (TA) measurements. This indicates that the presence of spatially separated electrons and holes in surface traps can cause internal electric fields that yield lineshapes characteristic of the Stark effect. Thus, the Stark lineshape measured by TA can report on the surface quality of NCs.

TA is a powerful time-resolved spectroscopy that has been used to understand excited state processes such as Auger recombination[204,205], energy transfer to phonons[206] or ligands[207,208], and carrier trapping[209] in NCs. Typically, this pump-probe technique is performed by varying the path length of one pulse

relative to the other by use of a retroreflector on a motorized translation stage. The transmission of many successive laser pulses is recorded at each pump-probe time delay in series. This technique typically requires measurement timescales on the order of tens of minutes to several hours, depending on factors such as sample response and laser noise. As a result, in its typical implementations TA fails to accurately report on excited state dynamics in non-equilibrium systems that are chemically changing on timescales shorter than a few hours, such as growing NCs.

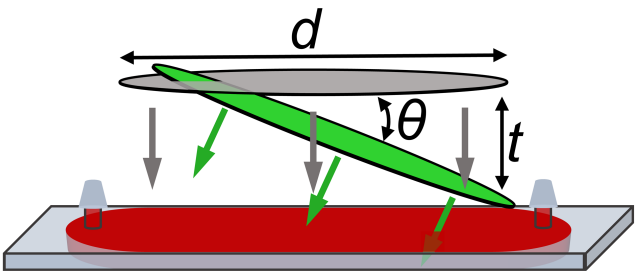

Figure 20. Sample plane in SSTA instrument showing pump (green) and probe (grey) focused to lines of length d. Probe pulse is incident normal to the cuvette. Spatially encoded time delay, t, is generated by the angle of the pump pulse relative to the probe pulse, θ, and the length of overlap between the two pulses d. Sample is injected into the flow-cell cuvette through septa to prevent solvent evaporation during the measurement. © Sadighian, Wilson, Crawford, and Wong.

TA measurements can be conducted more rapidly by using a single-shot transient absorption (SSTA) spectrometer that enables an entire transient to be recorded from a single pump-probe pulse pair. This can be achieved by tilting the wavefront of the pump pulse relative to the probe[210,211]. In this case, the time delay range is determined by Equation 1:

$$t_{range} = \frac{dsin(\theta)}{c} \tag{4.1}$$

where d is the length of overlap between pump and probe pulses, θ is the angle between the tilted pump pulse and the probe pulse, and c is the speed of light

(Figure 20). Here, I use a recently developed broadband SSTA spectrometer[136,212] to track the evolution of exciton dynamics in $MAPbI_3$ perovskite NCs as they nucleate and grow and as their surfaces are passivated with ligands. A complete TA spectrum with excellent signal to noise can be collected using this instrument in less than one minute, allowing us to accurately measure immature NCs before they degrade[187]. As a result, I am able to observe the surface of NCs being capped in real time by monitoring the evolving Stark lineshape. A carrier that has been photoexcited by the pump may localize on a surface trap state, creating an electric field within the NC. Using differential measurement, the probe then reports the effect of an ensemble of these electric fields on the absorption of the NC sample. These findings agree with previous reports of the growth mechanism of CdSe[62] and $MAPbI_3$[63] NCs, and open up a new avenue for studying the surface of these materials during growth.

4.2 Methods

4.2.1 Materials

All reagents were used as received: lead iodide (99.999%, trace metals basis, Sigma-Aldrich), methylammonium iodide (MAI, ≥99%, anhydrous, Sigma-Aldrich), octylamine (99%, Sigma-Aldrich), oleic acid (90%, technical grade, Sigma-Aldrich), and hexane (≥95%, laboratory reagent grade, Sigma-Aldrich). Cresyl violet (62%, J.T. Baker) in methanol (99.8%, Certified ACS, Fisher) was used to calibrate the beam profile and spatially encoded time delay of the SSTA spectrometer.

4.2.2 Nanocrystal Synthesis

$MAPbI_3$ NCs were synthesized using a previously reported solvation-limited synthesis[63,187]. 460 mg of PbI_2 and 127 mg of MAI were combined with 40 mL of hexane in a glass test tube and suspended in an ultrasonication bath

(VWR, 97043-992) to provide constant mixing. The reaction was initiated with the simultaneous introduction of 150 µL octylamine and 300 µL oleic acid, and the recorded reaction time is in reference to this addition. These organic ligands act to solubilize PbI_2 and MAI, which are otherwise insoluble in hexane[48]. A recirculating chiller (VWR, 1165) in a closed-loop configuration with an aluminum block was used to maintain a temperature of 22 in the ultrasonication bath. An HDPE syringe was used to withdraw aliquots of the reaction mixture at selected time points. Each aliquot was filtered through a syringe filter (VWR) with a 0.45 µm pore polytetrafluoroethylene (PTFE) membrane and into a 0.2 mm path length quartz flow cell cuvette (Starna Cells, 48-Q-0.2). Following the 15 minute mark a 1.0 µm PTFE pre-filter (Whatman Rezist) was used in conjunction with the 0.45 µm filter to compensate for increased suspended particulate. An additional 5.0 µm filter (Whatman Rezist) was added after 60 minutes. The flow cell was emptied, rinsed with acetone and hexane, and dried with a stream of nitrogen before each successive measurement.

4.2.3 Absorbance and Fluoresence

Absorbance and fluorescence of the filtered NC aliquots were simultaneously recorded on a homebuilt spectrometer (Figure 21) using the same cuvette and sample described above. To measure absorbance, light from a tungsten-halogen lamp (Thorlabs, SLS201) was directed into the sample using a fiber optic cable (Thorlabs, M28L01) and the resulting transmission collected using a second fiber. A 405 nm laser (Thorlabs, CPS405) was used as the fluorescence excitation source. Emitted light was collected using a fiber optic cable (Thorlabs, M95L01) directed to the spot upon which the laser was incident on the cuvette and angled to avoid the specular reflection of the excitation source. Absorbance and fluorescence

spectra were recorded using an Ocean Optics Flame-T-VIS-NIR and Flame-T-UV-VIS spectrometer, respectively. The spectrometers were operated using a homebuilt Python software package. Absorbance and fluorescence were recorded immediately before and after collecting SSTA measurements of each aliquot to make sure the spectra did not change significantly during the measurement. The pairs of spectra were then averaged together for analysis.

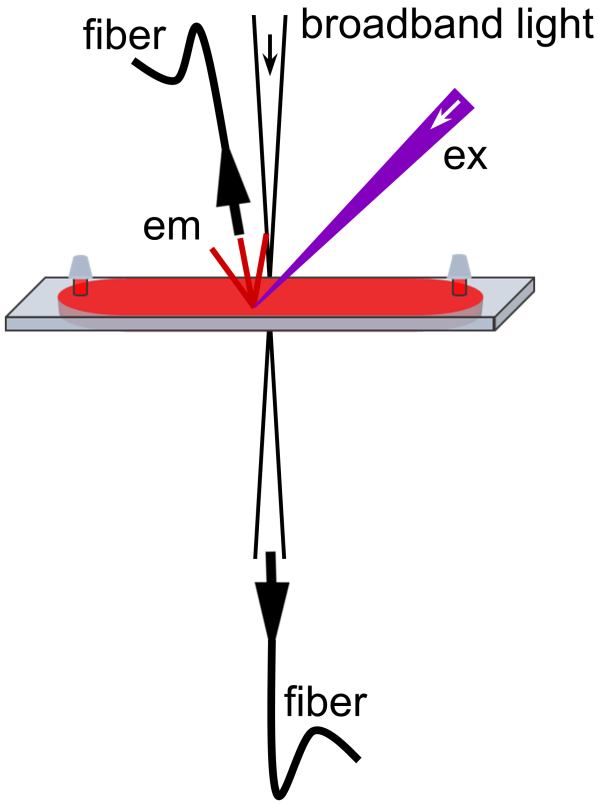

Figure 21. Schematic showing arrangement of light sources and collection fibers for absorbance and fluorescence measurements. Broadband light from a tungsten-halogen lamp (Thorlabs, SLS201) was focused into the sample cuvette and the transmission collected using a fiber optic cable (Thorlabs, M28L01). A 405 nm laser (Thorlabs, CPS405) was used as the fluorescence excitation source (ex). Emitted light (em) is collected with a fiber optic cable (Thorlabs, M95L01) angled to avoid scatter from the excitation source.

4.2.4 Single-Shot Transient Absorption

SSTA measurements were performed using a previously described homebuilt instrument[136,212]. A 1 kHz Ti:sapphire laser (Coherent, Astrella) with an 800 nm output was used to pump an optical parametric amplifier (Light Conversion, Topas Prime Plus) to generate 520 nm pump pulses that were compressed to 50 fs using a prism pair. A 2 m focal length mirror focused part of the 800 nm fundamental in a 1.6 m homebuilt gas cell with 1.5 mm quartz windows and containing 0.55 bar differential pressure of argon (PurityPlus, 99.999%) to generate broadband probe pulses. The spectral profiles of both pulses are shown in Figure 22. The pump and probe pulses were optically chopped at 250 and 125 Hz, respectively. The addition of a chopper in the probe line enabled the subtraction of background signals arising from pump induced fluorescence, scatter, stray light, and dark current from the camera[213]. A spatial light modulator (Meadowlark, 1920 x 1152 XY Phase Series SLM) placed after the choppers was used to reshape both beams to a flat-top intensity profile to provide a uniform excitation density across the entire spatially encoded time delay range. The pump pulse energy at the sample was set to 410 nJ to prevent non-linear interactions. The pump and probe beams were focused to lines using cylindrical lenses with focal lengths of 200 mm and 150 mm, respectively, and overlapped on a 20 µm x 22 mm area of the cuvette. While the probe was incident normal to the sample, the pump beam was tilted at an angle of 55.5° to achieve a spatially encoded time delay of 60 ps. The probe beam at the sample plane was imaged onto the slit of a grating spectrograph (Princeton Instruments, Isoplane 160), where it was measured to be 10 nJ. The probe beam was slightly defocused at the sample plane such that the entire measured wavelength range overlaps well onto the slit of the spectrograph with

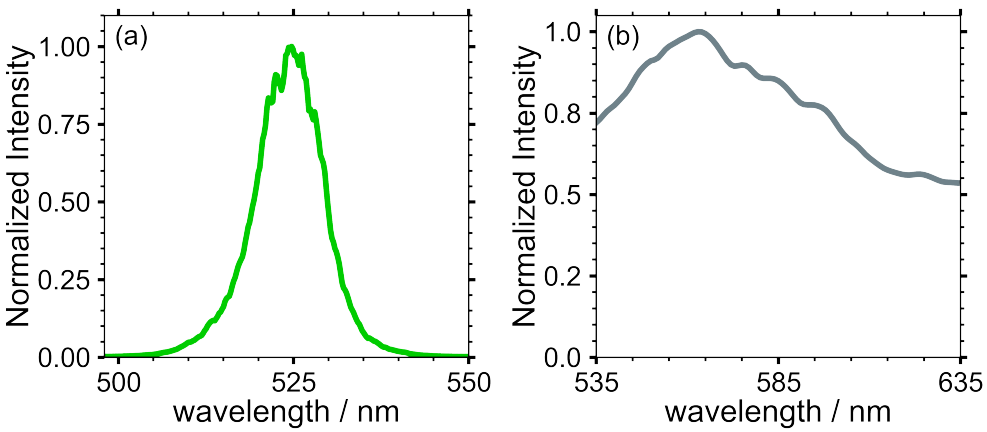

Figure 22. (a) Spectrum of pump pulses used in single-shot transient absorption measurements. (b) Spectrum of broadband probe across the measured wavelength range. © Sadighian, Wilson, Crawford, and Wong.

sufficient intensity. The spectrograph was coupled to a CMOS camera (Andor, Zyla 5.5) with a 1.3 ms exposure time which acquires 180 x 2560 pixel (1.17 mm x 16.6 mm) images, with the signal at each pixel corresponding to a pump-probe time delay of 24 fs. One axis of the pixel array recorded wavelength resolution of the probe and the other captured the spatially encoded time delay. Each SSTA spectrum was recorded for 60 seconds to maximize signal-to-noise ratio while still avoiding sample degradation. The SSTA spectrometer was operated using homebuilt Python software. Spectral calibration was performed using a HgAr calibration source, which accounts for spherical aberrations in the imaging setup through the spectrometer. Calibration of the spatially encoded pump-probe time delay was performed using SSTA measurements of cresyl violet in methanol in the same cuvette used for the NC measurements. This process corrects for chirp in the broadband probe pulse. Both the wavelength and time delay calibrations are discussed in detail elsewhere.[136].

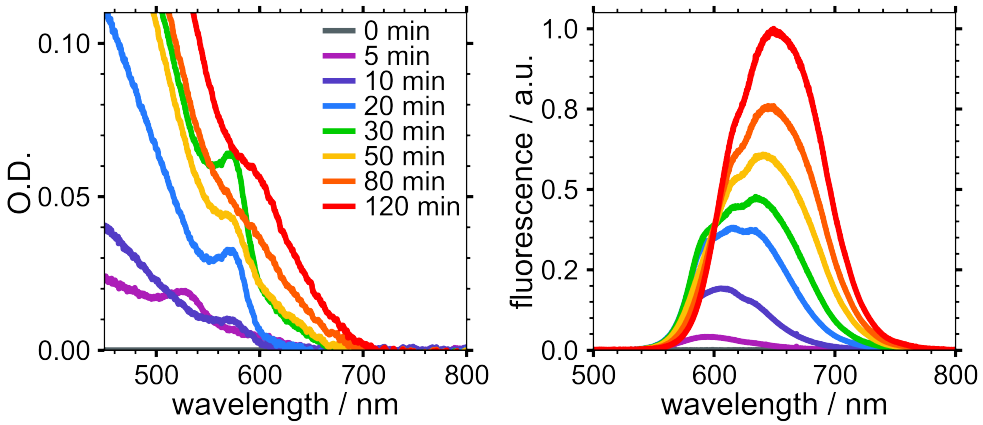

Figure 23. Absorbance (left) and fluorescence (right) of PTFE-filtered reaction mixture sampled at different times during growth. © Sadighian, Wilson, Crawford, and Wong.

4.3 Results and Discussion

Absorbance and fluorescence spectra at various reaction timepoints show the evolving physical and electronic structure of PTFE-filtered NCs over 120 minutes of growth (Figure 23). Nucleation occurred within the first 5 minutes, evidenced by the appearance of a broad, low intensity emission centered around 595 nm and weak absorbance near 525 nm. The fluorescence of the reaction mixture significantly increased in intensity by the 10 minute mark and began to exhibit two distinct peaks. A feature emerged at 575 nm in the absorbance spectrum, which I ascribe to nascent NCs. These absorbance and fluorescence features continued to grow in intensity, reaching a maximum at the 30 minute mark. Following this, the sharp absorbance peak at 575 nm began to disappear and gave rise to a broad shoulder at 610 nm, indicative of the small, nascent NCs growing larger. Likewise, the fluorescence spectrum began to lose intensity at shorter wavelengths while the peak at 635 nm continued to grow and redshift until

the final measured timepoint. The evolution of these spectra are in agreement with previously reported experiments performed under similar conditions[63,187].

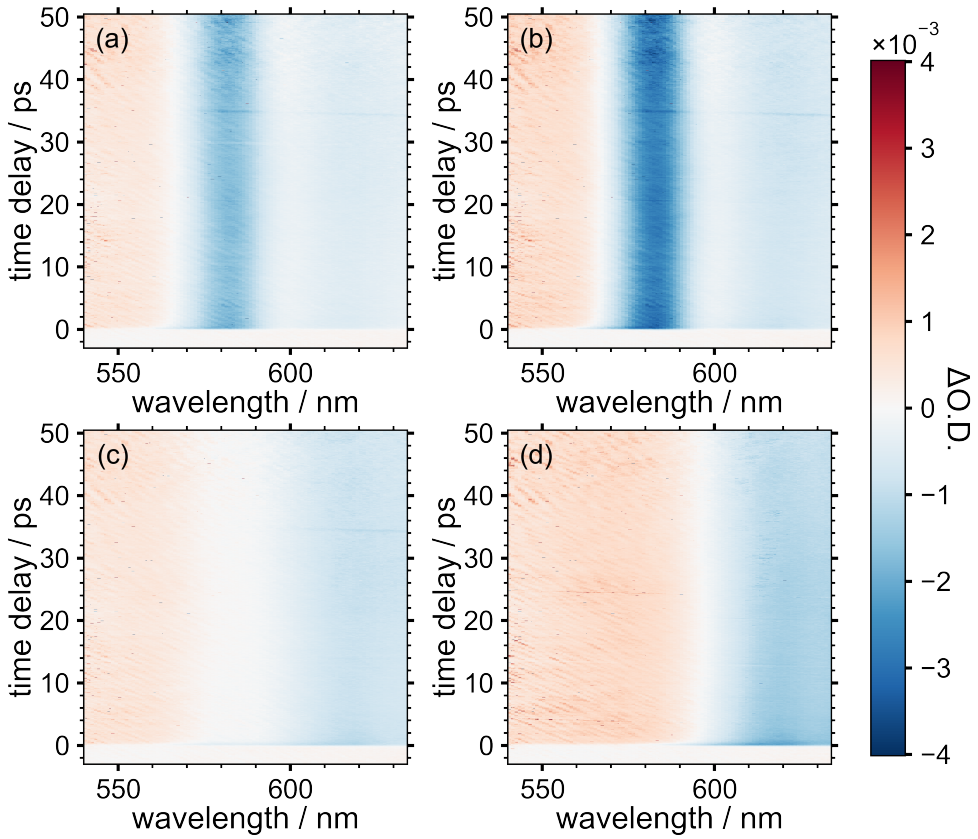

Figure 24. SSTA spectra of NC aliquots measured after (a) 20 minutes, (b) 30 minutes, (c) 50 minutes, and (d) 120 minutes after starting the reaction. © Sadighian, Wilson, Crawford, and Wong.

Select SSTA spectra for NCs at various stages of growth are shown in Figure 24. For each sample, the transient spectrum redshifts approximately 10 nm during the first 500 fs as a result of carrier cooling[214]. The spectra are quite stable for the remainder of the measured 60 ps time window. The spectrum of NCs grown for 120 minutes (Figure 24d) is typical of $MAPbI_3$ perovskite NCs[48]. The negative TA at wavelengths longer than 600 nm overlaps with the band-edge absorbance and the emission spectrum. This feature is typically ascribed to a combination of stimulated

emission (SE) and ground-state bleach (GSB). The signal at shorter wavelengths is broad and positive, indicating a photoinduced absorption (PIA) to higher electronic states. The SSTA spectra of NCs grown for 20, 30, and 50 minutes (Figure 24a-c) show two distinct features not present in the 120 minute spectrum; a strong, narrow, negative TA signal centered at 582 nm and a region of low signal intensity near 600 nm. This signal reached its maximum in the 30 minute sample and had all but disappeared 50 minutes into the reaction. The negative signal at 582 nm does not coincide with the absorbance peak (575 nm) and the fluorescence spectrum has a shoulder at 595 nm, suggesting neither GSB nor SE can explain this signal. First

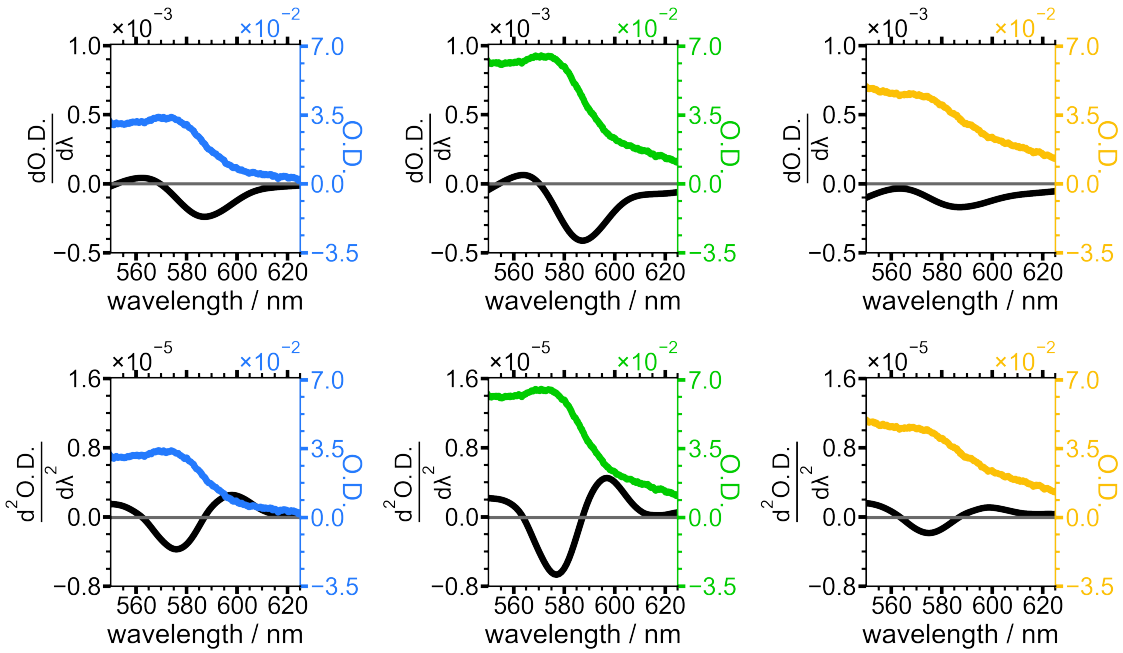

Figure 25. Absorbance spectra of NCs grown for 20 minutes (blue), 30 minutes (green), and 50 minutes (yellow). First (top) and second (bottom) derivative of the absorbance spectrum for each time point is shown in black. © Sadighian, Wilson, Crawford, and Wong.

and second derivatives of the absorbance spectra for the 20, 30, and 50 minute NC samples are shown in Figure 25. The lineshape of the derivatives is similar across

the three selected timepoints, with the magnitude of the derivative traces reaching their maximum in the 30 minute sample when the sharp absorbance peak at 575 nm is most intense. This peak is less intense and broader in width in the 50 minute sample, resulting in smaller derivatives for this timepoint.

In order to elucidate the origin of the TA lineshapes and gain additional insight into the electronic structure of growing NCs, a slice of the TA spectrum, reported in differential optical density (O.D.) and averaged between 5 ps and 10 ps for each growth time, t, was fit using Equation 2.

$$\Delta\text{O.D.}(t,\lambda) = A\frac{d\text{O.D.}(t,\lambda)}{d\lambda} + B\frac{d^2\text{O.D.}(t,\lambda)}{d\lambda^2} + C\Delta\text{O.D.}(120\,\text{min},\lambda) \qquad (4.2)$$

The first two terms represent the first and second derivatives of the absorbance spectrum at the selected growth time and the third term is the analogous TA spectrum of the NC sample after 120 minutes of growth. This term accounts for the contribution of well-passivated NCs to the overall TA spectrum at each timepoint. The resulting fits are overlaid with TA slices in Figure 26. The colored, dashed lines are TA slices for the three time points from Figures 24 and 25, and the fits (solid black lines) show good agreement. These slices reveal the evolution of the electric field induced by electron-hole pairs generated by the pump pulse in the nascent NCs. The negative TA signal at 580 nm was clearly visible after 20 minutes of NC growth and reached a maximum after 30 minutes, indicating the presence of growing, poorly-capped NCs. During the remainder of the reaction this feature lost intensity and by 50 minutes was barely discernible. The values of the three coefficients from Equation 2 are displayed with fit errors in Table 1. Tracking their values during the reaction quantifies the evolving contributions to the TA lineshapes. The first term, A, relates the observed signal to the first derivative of the absorbance, which occurs when the field causes a shift in the transition

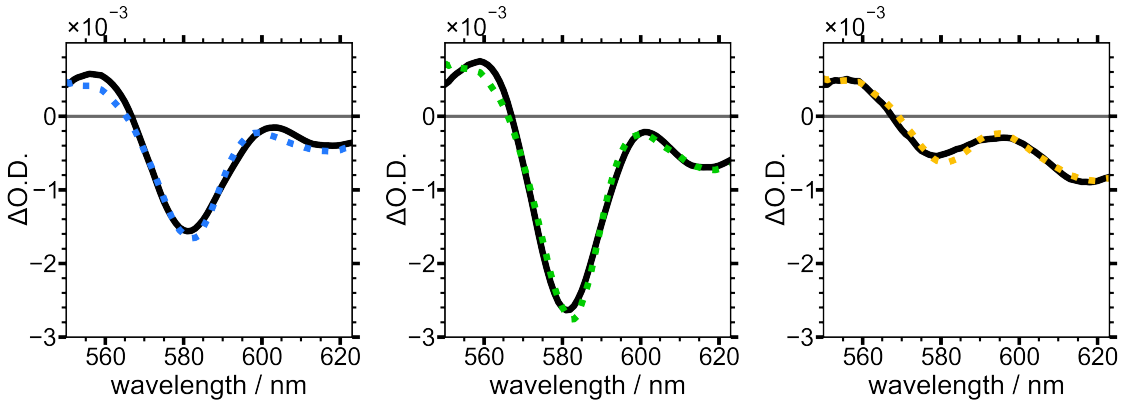

Figure 26. Averaged TA spectra from 5-10 ps for NCs grown for 20 minutes (blue), 30 minutes (green), and 50 minutes (yellow). Black line shows fit to Equation 2. © Sadighian, Wilson, Crawford, and Wong.

energy for the NCs. Here, the presence of spatially separated electrons and holes at surface traps would induce a dipole that could stabilize the excited electronic states, potentially redshifting the optical transition. The second derivative term, B, has the largest contribution to the signal throughout nearly the entire measured range. This term arises from an overall broadening of the absorbance spectrum, suggesting the presence of many randomly oriented dipoles in the sample arising from surface-trapped carriers.

The electric field produced by a trapped carrier should become smaller as a NC grows larger, so the decreasing contribution of the derivative lineshapes during NC growth could be the result of both increasing NC size and improved surface capping, resulting in fewer NCs with internal electric fields. While the contributions from both derivatives decline to zero over the course of the reaction, B shows a brief period of growth between 30 and 70 minutes into the reaction. The electric field strength at any particular time point during NC growth could be estimated from these results if the NC size were known, assuming that one

Table 1. Best-fit values for parameters A, B, and C with one standard deviation error of the fitted variables (σ_X).

Reaction Timepoint (min)	$A \pm \sigma_A$	$B \pm \sigma_B$	$C \pm \sigma_C$
10	5.33 ± 0.12	628 ± 27	0.127 ± .007
15	6.15 ± 0.15	313 ± 14	0.232 ± .015
20	5.49 ± 0.11	232 ± 8	0.241 ± .017
25	5.41 ± .07	227 ± 5	0.235 ± .015
30	5.07 ± .07	217 ± 5	0.253 ± .018
35	4.64 ± .08	204 ± 5	0.337 ± .019
40	4.24 ± .07	208 ± 5	0.413 ± .013
45	4.08 ± .07	245 ± 6	0.513 ± .011
50	3.66 ± .07	259 ± 8	0.514 ± .009
55	3.36 ± .06	277 ± 8	0.533 ± .008
60	2.44 ± .04	310 ± 6	0.548 ± .004
70	1.91 ± .07	396 ± 21	0.539 ± .009
80	1.86 ± .09	262 ± 23	0.604 ± .011
100	0.281 ± .03	46.6 ± 5.6	0.776 ± .006
120	0	0	1

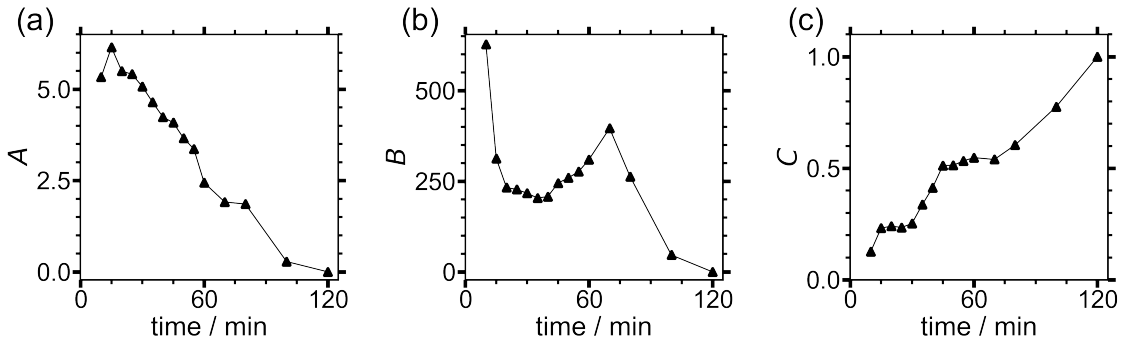

Figure 27. Fit coefficients from Equation 2 for NCs measured at different growth times. Contributions from the (a) first and (b) second derivatives, as well as the (c) 120 minute NC component to the overall fit. © Sadighian, Wilson, Crawford, and Wong.

carrier is surface-trapped while the other is delocalized (i.e. on average centrally located within the NC). Future work will focus on concurrent measurements of NC size during the reaction, which will enable the magnitude of the electric field

caused by a surface-trapped carrier to be modeled during NC growth. This will aid in the interpretation of the rise in B while A continually decreases. C, the contribution of well-passivated NCs, shows a fairly linear growth throughout the entire synthesis. By the end of the reaction the NCs are well-capped with ligands, and surface traps no longer contribute to the TA signal. Thus, our measurements indicate that poorly-capped NCs are dominant during the growth of perovskite NCs, becoming progressively better capped as the growth process continues, similar to the case shown in Figure 19b. Future studies using different filter media of different polarities to separate well- and poorly-capped NCs[63] will seek to test this assumption and further isolate the evolving lineshapes of these sub-populations within the reaction mixture. As demonstrated here by the intriguing trends in the weights of the two derivative features, the ability of SSTA to measure lineshapes during a NC synthesis provides a new avenue to deeper insights into how NCs grow. Further analyses of both the lineshapes and the exciton dynamics hold promise for understanding the evolving nature of carrier traps in nascent NCs.

4.4 Conclusion

A novel, broadband, tilted-pulse SSTA spectrometer with a 60 ps time delay was used to investigate evolving excited state dynamics in NCs grown *via* a solvation-limited synthesis. Growing NCs were found to exhibit a unique TA lineshape indicative of the Stark effect. Fits of these data to a weighted sum of linear absorbance spectrum derivatives show that this lineshape is likely caused by spatially separated charge carriers in surface trap states. This adds to the growing body of evidence that these NCs are poorly capped during most of their growth[62,63]. This work proves the applicability of this technique to the study of non-equilibrium systems such as growing NCs that were previously inaccessible

with non-linear spectroscopies. The development of SSTA and this sampling technique provide powerful tools for understanding how the electronic structure and excited state dynamics of NCs change during their synthesis. These types of experiments may offer new insight into NC growth mechanisms and how reaction parameters can be changed to target desired photophysics.

CHAPTER V

FUTURE DIRECTIONS

5.1 Investigating Ostwald Ripening During Perovskite NC Growth

Spectra of $MAPbI_3$ perovskite NCs taken during growth suggest that the growth mechanism changes after ≈30 minutes. This is more apparent in experiments I have done studying $MAPbI_3$ NCs grown at higher temperature. We see clear redshifts in the GSB peak as it grows in during the first 30 minutes of the reaction. Following this, the peak starts to shift back to high energy as more NCs become fully grown. This coincides with the increase in the contribution of the Stark broadening term. One possible explanation for this observation is that Ostwald ripening starts occurring in the NCs beyond 30 minutes. Ostwald ripening occurs when larger particles grow at the expense of smaller particles. As the solution equilibrium shifts, smaller particles start to break apart and be consumed by the larger, growing NCs. This would also temporarily create smaller, poorly-passivated NCs, blueshifting the excitonic peak in both the linear absorbance and TA spectra. Additional work will monitor how the rate of this process changes as a function of synthetic conditions and how this affects the final NC size distribution.

5.2 Modulating Reaction Parameters

The influence of surface-ligand concentration on NC nucleation and growth kinetics is still poorly understood, particularly with respect to the rate of nucleation and the overall surface passivation in fully grown NCs. Experiments in which initial ligand concentrations are varied show different intensities of the NC intermediate peak in the linear absorbance spectra, along with different Stark shifts in the TA. Monitoring how the amount of initial ligand, as well as different amounts added at various times during growth, changes how the NC surface evolves

during these processes will increase understanding of the mechanisms by which these materials form.

5.3 Growth of Mixed-Halide Perovskite NCs

Tuning the absorbance of LHP NCs through the visible spectrum requires engineering the halide composition. While $MAPbI_3$ NCs are excellent emitters in the red portion of the visible spectrum, emission of the specific red required for RGB displays requires a mixture of iodide and bromide halides in the perovskite crystal structure. A green emission requires pure $MAPbBr_3$ NCs. The growth of $MAPbBr_3$ differs significantly, with immediate formation of a monomodal emission peak that increases in intensity as the reaction progresses. Similar spectral lineshapes are observed during the growth of $MAPbBr_xI_{3-x}$ NCs. As the stability of these mixed halide NCs is of the utmost importance for successful commercialization, continued work on understanding how these NCs form is essential.

5.4 Conclusion

This dissertation has described insights into the mechanism by which $MAPbI_3$ NCs grow and become capped by surface ligands. Chapter 1 presents a brief introduction to perovskite NCs and describes the importance of characterizing the NC surface during growth. The large surface-area-to-volume ratio of NCs means that these surface-ligand interactions dominate NC behavior. The NC surface determines physical stability as well as electronic structure and charge carrier dynamics. In addition, different species of ligands can alter the final morphology of the nanostructure. While many tools exists to characterize NC surfaces, in situ characterization of the surface while NCs nucleate and grow has remained an elusive target.

One factor limiting the investigation of perovskite NC growth is the timescale over which most perovskite NC syntheses are complete. In Chapter 2, I introduce a synthesis for perovskite NCs that slows reaction kinetics through use of a strongly non-polar solvent. This allowed a rapid sampling technique to quickly extract and purify growing NCs for spectroscopic investigation by filtering them through PTFE syringe filters. Absorbance and fluorescence measurements of these nascent NCs revealed a series of unstable intermediates that eventually form fully grown LHP NCs. Chapter 3 builds on this novel synthesis through the use of different syringe filter media for rapid, surface-specific purification of NCs. A polar, nylon syringe filter is shown to produce an NC population with narrow, monomodal emission and strong fluorescence. Evidence is provided that this is due to well-passivated NCs that start to appear later in the reaction.

In Chapter 4, I use a novel SSTA spectrometer to study this perovskite NC synthesis. The short acquisition time required by the SSTA instrument permits collection of multiple TA spectra during the course of the reaction. A unique spectral lineshape is observed to grow in and disappear during the reaction. I show that this lineshape can arise from trapped carriers at the NC surface inducing a Stark shift in the TA spectrum. The success of these experiments opens the door for future studies of excited-state dynamics in growing NCs and provides researchers the ability to tune several reaction parameters while observing, in real time, the resulting changes to NC nucleation and growth. The knowledge gained through these experiments will aid researchers in developing synthetic techniques that permit rational design of materials with targeted properties.

REFERENCES CITED

(1) Katz, E. A. Perovskite: Name Puzzle and German-Russian Odyssey of Discovery. *Helvetica Chimica Acta* **2020**, *103*, e2000061.

(2) Navrotsky, A.; Weidner, D. J. *Perovskite: A Structure of Great Interest to Geophysics and Materials Science*; 1989; Vol. 45; p xi.

(3) Rose, G. Beschreibung einiger neuen Mineralien des Urals. *Annalen der Physik* **1839**, *124*, 551–573.

(4) Rose, G. *Reise nach dem Ural, dem Altai und dem Kaspischen Meere*, 1st ed.; Verlag der Sanderschen Buchhandlung (C. W. Eichhoff): Berlin, 1837.

(5) Rose, G. *Reise nach dem Ural, dem Altai und dem Kaspischen Meere*, 1st ed.; Verlag der Sanderschen Buchhandlung (G. E. Reimer): Berlin, 1842.

(6) Bednorz, J. G.; Müller, K. A. Perovskite-type oxides—The new approach to high-T_c superconductivity. *Reviews of Modern Physics* **1988**, *60*, 585–600.

(7) Snaith, H. J. Perovskites: The Emergence of a New Era for Low-Cost, High-Efficiency Solar Cells. *The Journal of Physical Chemistry Letters* **2013**, *4*, 3623–3630.

(8) Green, M. A.; Ho-Baillie, A.; Snaith, H. J. The emergence of perovskite solar cells. *Nature Photonics* **2014**, *8*, 506–514.

(9) Tan, Z.-K.; Moghaddam, R. S.; Lai, M. L.; Docampo, P.; Higler, R.; Deschler, F.; Price, M.; Sadhanala, A.; Pazos, L. M.; Credgington, D.; Hanusch, F.; Bein, T.; Snaith, H. J.; Friend, R. H. Bright light-emitting diodes based on organometal halide perovskite. *Nature Nanotechnology* **2014**, *9*, 687–692.

(10) Weber, D. $CH_3NH_3SnBr_xI_{3-x}$ (x = 0-3), ein Sn(II)-System mit kubischer Perowskitstruktur / $CH_3NH_3SnBr_xI_{3-x}$(x = 0-3), a Sn(II)-System with Cubic Perovskite Structure. *Zeitschrift für Naturforschung B* **1978**, *33*, 862–865.

(11) Weber, D. $CH_3NH_3PbX_3$, ein Pb(II)-System mit kubischer Perowskitstruktur / $CH_3NH_3PbX_3$, a Pb(II)-System with Cubic Perovskite Structure. *Zeitschrift für Naturforschung B* **1978**, *33*, 1443–1445.

(12) Weber, D. Das Perowskitsystem CH_3NH_3 [$Pb,Sn_{1-n}X_3$] (X = Cl, Br, I) / The Perovskite System CH_3NH_3[$Pb_nSn_{1-n}X_n$] (X = C1, Br, I). *Zeitschrift für Naturforschung B* **1979**, *34*, 939–941.

(13) Kojima, A.; Teshima, K.; Shirai, Y.; Miyasaka, T. Organometal Halide Perovskites as Visible-Light Sensitizers for Photovoltaic Cells. *Journal of the American Chemical Society* **2009**, *131*, 6050–6051.

(14) Jeong, J. et al. Pseudo-halide anion engineering for α-$FAPbI_3$ perovskite solar cells. *Nature* **2021**, *592*, 381–385.

(15) Galkowski, K.; Mitioglu, A.; Miyata, A.; Plochocka, P.; Portugall, O.; Eperon, G. E.; Wang, J. T.-W.; Stergiopoulos, T.; Stranks, S. D.; Snaith, H. J.; Nicholas, R. J. Determination of the exciton binding energy and effective masses for methylammonium and formamidinium lead tri-halide perovskite semiconductors. *Energy & Environmental Science* **2016**, *9*, 962–970.

(16) Herz, L. M. Charge-Carrier Mobilities in Metal Halide Perovskites: Fundamental Mechanisms and Limits. *ACS Energy Letters* **2017**, *2*, 1539–1548.

(17) Schmidt, L. C.; Pertegás, A.; González-Carrero, S.; Malinkiewicz, O.; Agouram, S.; Mínguez Espallargas, G.; Bolink, H. J.; Galian, R. E.; Pérez-Prieto, J. Nontemplate Synthesis of $CH_3NH_3PbBr_3$ Perovskite Nanoparticles. *Journal of the American Chemical Society* **2014**, *136*, 850–853.

(18) Yakunin, S.; Protesescu, L.; Krieg, F.; Bodnarchuk, M. I.; Nedelcu, G.; Humer, M.; Luca, G. D.; Fiebig, M.; Heiss, W.; Kovalenko, M. V. Low-threshold amplified spontaneous emission and lasing from colloidal nanocrystals of caesium lead halide perovskites. *Nature Communications* **2015**, *6*, 1–9.

(19) Li, G.; Rivarola, F. W. R.; Davis, N. J. L. K.; Bai, S.; Jellicoe, T. C.; Peña, F. d. l.; Hou, S.; Ducati, C.; Gao, F.; Friend, R. H.; Greenham, N. C.; Tan, Z.-K. Highly Efficient Perovskite Nanocrystal Light-Emitting Diodes Enabled by a Universal Crosslinking Method. *Advanced Materials* **2016**, *28*, 3528–3534.

(20) Tang, B.; Dong, H.; Sun, L.; Zheng, W.; Wang, Q.; Sun, F.; Jiang, X.; Pan, A.; Zhang, L. Single-Mode Lasers Based on Cesium Lead Halide Perovskite Submicron Spheres. *ACS Nano* **2017**, *11*, 10681–10688.

(21) Rainò, G.; Becker, M. A.; Bodnarchuk, M. I.; Mahrt, R. F.; Kovalenko, M. V.; Stöferle, T. Superfluorescence from lead halide perovskite quantum dot superlattices. *Nature* **2018**, *563*, 671–675.

(22) Dong, Y.; Zhao, Y.; Zhang, S.; Dai, Y.; Liu, L.; Li, Y.; Chen, Q. Recent advances toward practical use of halide perovskite nanocrystals. *Journal of Materials Chemistry A* **2018**, *6*, 21729–21746.

(23) Utzat, H.; Sun, W.; Kaplan, A. E. K.; Krieg, F.; Ginterseder, M.; Spokoyny, B.; Klein, N. D.; Shulenberger, K. E.; Perkinson, C. F.; Kovalenko, M. V.; Bawendi, M. G. Coherent single-photon emission from colloidal lead halide perovskite quantum dots. *Science* **2019**, *363*, 1068–1072.

(24) Bera, S.; Pradhan, N. Perovskite Nanocrystal Heterostructures: Synthesis, Optical Properties, and Applications. *ACS Energy Letters* **2020**, *5*, 2858–2872.

(25) Liu, C.; Zeng, Q.; Wei, H.; Yu, Y.; Zhao, Y.; Feng, T.; Yang, B. Metal Halide Perovskite Nanocrystal Solar Cells: Progress and Challenges. *Small Methods* **2020**, *4*, 2000419.

(26) Schanze, K. S.; Kamat, P. V.; Yang, P.; Bisquert, J. Progress in Perovskite Photocatalysis. *ACS Energy Letters* **2020**, *5*, 2602–2604.

(27) Fu, Y.; Meng, F.; Rowley, M. B.; Thompson, B. J.; Shearer, M. J.; Ma, D.; Hamers, R. J.; Wright, J. C.; Jin, S. Solution Growth of Single Crystal Methylammonium Lead Halide Perovskite Nanostructures for Optoelectronic and Photovoltaic Applications. *Journal of the American Chemical Society* **2015**, *137*, 5810–5818.

(28) Dirin, D. N.; Protesescu, L.; Trummer, D.; Kochetygov, I. V.; Yakunin, S.; Krumeich, F.; Stadie, N. P.; Kovalenko, M. V. Harnessing Defect-Tolerance at the Nanoscale: Highly Luminescent Lead Halide Perovskite Nanocrystals in Mesoporous Silica Matrixes. *Nano Letters* **2016**, *16*, 5866–5874.

(29) Huang, H.; Bodnarchuk, M. I.; Kershaw, S. V.; Kovalenko, M. V.; Rogach, A. L. Lead Halide Perovskite Nanocrystals in the Research Spotlight: Stability and Defect Tolerance. *ACS Energy Letters* **2017**, *2*, 2071–2083.

(30) Hassan, Y.; Ashton, O. J.; Park, J. H.; Li, G.; Sakai, N.; Wenger, B.; Haghighirad, A.-A.; Noel, N. K.; Song, M. H.; Lee, B. R.; Friend, R. H.; Snaith, H. J. Facile Synthesis of Stable and Highly Luminescent Methylammonium Lead Halide Nanocrystals for Efficient Light Emitting Devices. *Journal of the American Chemical Society* **2019**, *141*, 1269–1279.

(31) Protesescu, L.; Yakunin, S.; Bodnarchuk, M. I.; Krieg, F.; Caputo, R.; Hendon, C. H.; Yang, R. X.; Walsh, A.; Kovalenko, M. V. Nanocrystals of Cesium Lead Halide Perovskites ($CsPbX_3$, X = Cl, Br, and I): Novel Optoelectronic Materials Showing Bright Emission with Wide Color Gamut. *Nano Letters* **2015**, *15*, 3692–3696.

(32) Hassan, Y.; Song, Y.; Pensack, R. D.; Abdelrahman, A. I.; Kobayashi, Y.; Winnik, M. A.; Scholes, G. D. Structure-Tuned Lead Halide Perovskite Nanocrystals. *Advanced Materials* **2016**, *28*, 566–573.

(33) Peterson, M. D.; Cass, L. C.; Harris, R. D.; Edme, K.; Sung, K.; Weiss, E. A. The Role of Ligands in Determining the Exciton Relaxation Dynamics in Semiconductor Quantum Dots. *Annual Review of Physical Chemistry* **2014**, *65*, 317–339.

(34) Boles, M. A.; Ling, D.; Hyeon, T.; Talapin, D. V. The surface science of nanocrystals. *Nature Materials* **2016**, *15*, 141.

(35) Sadighian, J. C.; Wong, C. Y. Just Scratching the Surface: In Situ and Surface-Specific Characterization of Perovskite Nanocrystal Growth. *The Journal of Physical Chemistry C* **2021**, *125*, 20772–20782.

(36) Pan, A.; He, B.; Fan, X.; Liu, Z.; Urban, J. J.; Alivisatos, A. P.; He, L.; Liu, Y. Insight into the Ligand-Mediated Synthesis of Colloidal $CsPbBr_3$ Perovskite Nanocrystals: The Role of Organic Acid, Base, and Cesium Precursors. *ACS Nano* **2016**, *10*, 7943–7954.

(37) Shamsi, J.; Dang, Z.; Bianchini, P.; Canale, C.; Di Stasio, F.; Brescia, R.; Prato, M.; Manna, L. Colloidal Synthesis of Quantum Confined Single Crystal $CsPbBr_3$ Nanosheets with Lateral Size Control up to the Micrometer Range. *Journal of the American Chemical Society* **2016**, *138*, 7240–7243.

(38) De, A.; Mondal, N.; Samanta, A. Luminescence tuning and exciton dynamics of Mn-doped $CsPbCl_3$ nanocrystals. *Nanoscale* **2017**, *9*, 16722–16727.

(39) Zhang, F.; Chen, C.; Kershaw, S. V.; Xiao, C.; Han, J.; Zou, B.; Wu, X.; Chang, S.; Dong, Y.; Rogach, A. L.; Zhong, H. Ligand-Controlled Formation and Photoluminescence Properties of $CH_3NH_3PbBr_3$ Nanocubes and Nanowires. *ChemNanoMat* **2017**, *3*, 303–310.

(40) Teunis, M. B.; Johnson, M. A.; Muhoberac, B. B.; Seifert, S.; Sardar, R. Programmable Colloidal Approach to Hierarchical Structures of Methylammonium Lead Bromide Perovskite Nanocrystals with Bright Photoluminescent Properties. *Chemistry of Materials* **2017**, *29*, 3526–3537.

(41) Dutta, A.; Dutta, S. K.; Das Adhikari, S.; Pradhan, N. Tuning the Size of $CsPbBr_3$ Nanocrystals: All at One Constant Temperature. *ACS Energy Letters* **2018**, *3*, 329–334.

(42) Peng, L.; Dutta, A.; Xie, R.; Yang, W.; Pradhan, N. Dot–Wire–Platelet–Cube: Step Growth and Structural Transformations in $CsPbBr_3$ Perovskite Nanocrystals. *ACS Energy Letters* **2018**, *3*, 2014–2020.

(43) Gonzalez-Carrero, S.; Francés-Soriano, L.; González-Béjar, M.; Agouram, S.; Galian, R. E.; Pérez-Prieto, J. The Luminescence of $CH_3NH_3PbBr_3$ Perovskite Nanoparticles Crests the Summit and Their Photostability under Wet Conditions is Enhanced. *Small* **2016**, *12*, 5245–5250.

(44) Brandt, R. E.; Stevanović, V.; Ginley, D. S.; Buonassisi, T. Identifying defect-tolerant semiconductors with high minority-carrier lifetimes: beyond hybrid lead halide perovskites. *MRS Communications* **2015**, *5*, 265–275.

(45) Meggiolaro, D.; G. Motti, S.; Mosconi, E.; J. Barker, A.; Ball, J.; Perini, C. A. R.; Deschler, F.; Petrozza, A.; Angelis, F. D. Iodine chemistry determines the defect tolerance of lead-halide perovskites. *Energy & Environmental Science* **2018**, *11*, 702–713.

(46) Kim, G.-W.; Petrozza, A. Defect Tolerance and Intolerance in Metal-Halide Perovskites. *Advanced Energy Materials* **2020**, *10*, 2001959.

(47) Zhang, F.; Zhong, H.; Chen, C.; Wu, X.-g.; Hu, X.; Huang, H.; Han, J.; Zou, B.; Dong, Y. Brightly Luminescent and Color-Tunable Colloidal $CH_3NH_3PbX_3$ (X = Br, I, Cl) Quantum Dots: Potential Alternatives for Display Technology. *ACS Nano* **2015**, *9*, 4533–4542.

(48) Wang, L.; Williams, N. E.; Malachosky, E. W.; Otto, J. P.; Hayes, D.; Wood, R. E.; Guyot-Sionnest, P.; Engel, G. S. Scalable Ligand-Mediated Transport Synthesis of Organic–Inorganic Hybrid Perovskite Nanocrystals with Resolved Electronic Structure and Ultrafast Dynamics. *ACS Nano* **2017**, *11*, 2689–2696.

(49) Levchuk, I.; Osvet, A.; Tang, X.; Brandl, M.; Perea, J. D.; Hoegl, F.; Matt, G. J.; Hock, R.; Batentschuk, M.; Brabec, C. J. Brightly Luminescent and Color-Tunable Formamidinium Lead Halide Perovskite $FAPbX_3$ (X = Cl, Br, I) Colloidal Nanocrystals. *Nano Letters* **2017**, *17*, 2765–2770.

(50) Mondal, N.; De, A.; Samanta, A. Achieving Near-Unity Photoluminescence Efficiency for Blue-Violet-Emitting Perovskite Nanocrystals. *ACS Energy Letters* **2019**, *4*, 32–39.

(51) Hassan, Y. et al. Ligand-engineered bandgap stability in mixed-halide perovskite LEDs. *Nature* **2021**, *591*, 72–77.

(52) Heo, J. H.; Park, J. K.; Im, S. H. Full-Color Spectrum Coverage by High-Color-Purity Perovskite Nanocrystal Light-Emitting Diodes. *Cell Reports Physical Science* **2020**, *1*, 100177.

(53) Conings, B.; Drijkoningen, J.; Gauquelin, N.; Babayigit, A.; D'Haen, J.; D'Olieslaeger, L.; Ethirajan, A.; Verbeeck, J.; Manca, J.; Mosconi, E.; Angelis, F. D.; Boyen, H.-G. Intrinsic Thermal Instability of Methylammonium Lead Trihalide Perovskite. *Advanced Energy Materials* **2015**, *5*, 1500477.

(54) Juarez-Perez, E. J.; Hawash, Z.; Raga, S. R.; Ono, L. K.; Qi, Y. Thermal degradation of $CH_3NH_3PbI_3$ perovskite into NH_3 and CH_3I gases observed by coupled thermogravimetry–mass spectrometry analysis. *Energy & Environmental Science* **2016**, *9*, 3406–3410.

(55) Samu, G. F.; Balog, ; De Angelis, F.; Meggiolaro, D.; Kamat, P. V.; Janáky, C. Electrochemical Hole Injection Selectively Expels Iodide from Mixed Halide Perovskite Films. *Journal of the American Chemical Society* **2019**, *141*, 10812–10820.

(56) Motti, S. G.; Meggiolaro, D.; Barker, A. J.; Mosconi, E.; Perini, C. A. R.; Ball, J. M.; Gandini, M.; Kim, M.; De Angelis, F.; Petrozza, A. Controlling competing photochemical reactions stabilizes perovskite solar cells. *Nature Photonics* **2019**, *13*, 532–539.

(57) Yang, R. X.; Tan, L. Z. Understanding size dependence of phase stability and band gap in $CsPbI_3$ perovskite nanocrystals. *The Journal of Chemical Physics* **2020**, *152*, 034702.

(58) Protesescu, L.; Yakunin, S.; Kumar, S.; Bär, J.; Bertolotti, F.; Masciocchi, N.; Guagliardi, A.; Grotevent, M.; Shorubalko, I.; Bodnarchuk, M. I.; Shih, C.-J.; Kovalenko, M. V. Dismantling the "Red Wall" of Colloidal Perovskites: Highly Luminescent Formamidinium and Formamidinium–Cesium Lead Iodide Nanocrystals. *ACS Nano* **2017**, *11*, 3119–3134.

(59) De Roo, J.; Ibáñez, M.; Geiregat, P.; Nedelcu, G.; Walravens, W.; Maes, J.; Martins, J. C.; Van Driessche, I.; Kovalenko, M. V.; Hens, Z. Highly Dynamic Ligand Binding and Light Absorption Coefficient of Cesium Lead Bromide Perovskite Nanocrystals. *ACS Nano* **2016**, *10*, 2071–2081.

(60) Green, P. B.; Narayanan, P.; Li, Z.; Sohn, P.; Imperiale, C. J.; Wilson, M. W. Controlling Cluster Intermediates Enables the Synthesis of Small PbS Nanocrystals with Narrow Ensemble Line Widths. *Chemistry of Materials* **2020**, *32*, 4083–4094.

(61) Kazes, M.; Udayabhaskararao, T.; Dey, S.; Oron, D. Effect of Surface Ligands in Perovskite Nanocrystals: Extending in and Reaching out. *Accounts of Chemical Research* **2021**, *54*, 1409–1418.

(62) Teunis, M. B.; Liyanage, T.; Dolai, S.; Muhoberac, B. B.; Sardar, R.; Agarwal, M. Unraveling the Mechanism Underlying Surface Ligand Passivation of Colloidal Semiconductor Nanocrystals: A Route for Preparing Advanced Hybrid Nanomaterials. *Chemistry of Materials* **2017**, *29*, 8838–8849.

(63) Sadighian, J. C.; Crawford, M. L.; Suder, T. W.; Wong, C. Y. Surface ligation stage revealed through polarity-dependent fluorescence during perovskite nanocrystal growth. *Journal of Materials Chemistry C* **2020**, *8*, 7041–7050.

(64) Salzmann, B. B. V.; van der Sluijs, M. M.; Soligno, G.; Vanmaekelbergh, D. Oriented Attachment: From Natural Crystal Growth to a Materials Engineering Tool. *Accounts of Chemical Research* **2021**, *54*, 787–797.

(65) LaMer, V. K.; Dinegar, R. H. Theory, Production and Mechanism of Formation of Monodispersed Hydrosols. *Journal of the American Chemical Society* **1950**, *72*, 4847–4854.

(66) Wang, F.; Richards, V. N.; Shields, S. P.; Buhro, W. E. Kinetics and Mechanisms of Aggregative Nanocrystal Growth. *Chemistry of Materials* **2014**, *26*, 5–21.

(67) Whitehead, C. B.; Özkar, S.; Finke, R. G. LaMer's 1950 Model for Particle Formation of Instantaneous Nucleation and Diffusion-Controlled Growth: A Historical Look at the Model's Origins, Assumptions, Equations, and Underlying Sulfur Sol Formation Kinetics Data. *Chemistry of Materials* **2019**, *31*, 7116–7132.

(68) Li, Y.; Huang, H.; Xiong, Y.; Kershaw, S. V.; Rogach, A. L. Revealing the Formation Mechanism of $CsPbBr_3$ Perovskite Nanocrystals Produced via a Slowed-Down Microwave-Assisted Synthesis. *Angewandte Chemie International Edition* **2018**, *57*, 5833–5837.

(69) Xue, J.; Wang, R.; Yang, Y. The surface of halide perovskites from nano to bulk. *Nature Reviews Materials* **2020**, *5*, 809–827.

(70) Pradhan, N. Why Do Perovskite Nanocrystals Form Nanocubes and How Can Their Facets Be Tuned? A Perspective from Synthetic Prospects. *ACS Energy Letters* **2021**, *6*, 92–99.

(71) Ravi, V. K.; Santra, P. K.; Joshi, N.; Chugh, J.; Singh, S. K.; Rensmo, H.; Ghosh, P.; Nag, A. Origin of the Substitution Mechanism for the Binding of Organic Ligands on the Surface of $CsPbBr_3$ Perovskite Nanocubes. *The Journal of Physical Chemistry Letters* **2017**, *8*, 4988–4994.

(72) Chen, Y.; Smock, S. R.; Flintgruber, A. H.; Perras, F. A.; Brutchey, R. L.; Rossini, A. J. Surface Termination of $CsPbBr_3$ Perovskite Quantum Dots Determined by Solid-State NMR Spectroscopy. *Journal of the American Chemical Society* **2020**, *142*, 6117–6127.

(73) Pradhan, N. Alkylammonium Halides for Facet Reconstruction and Shape Modulation in Lead Halide Perovskite Nanocrystals. *Accounts of Chemical Research* **2021**, *54*, 1200–1208.

(74) Brown, A. A. M.; Vashishtha, P.; Hooper, T. J. N.; Ng, Y. F.; Nutan, G. V.; Fang, Y.; Giovanni, D.; Tey, J. N.; Jiang, L.; Damodaran, B.; Sum, T. C.; Pu, S. H.; Mhaisalkar, S. G.; Mathews, N. Precise Control of $CsPbBr_3$ Perovskite Nanocrystal Growth at Room Temperature: Size Tunability and Synthetic Insights. *Chemistry of Materials* **2021**, *33*, 2387–2397.

(75) Imran, M.; Ijaz, P.; Goldoni, L.; Maggioni, D.; Petralanda, U.; Prato, M.; Almeida, G.; Infante, I.; Manna, L. Simultaneous Cationic and Anionic Ligand Exchange For Colloidally Stable $CsPbBr_3$ Nanocrystals. *ACS Energy Letters* **2019**, *4*, 819–824.

(76) Kirakosyan, A.; Chinh, N. D.; Sihn, M. R.; Jeon, M.-G.; Jeong, J.-R.; Kim, D.; Jang, J. H.; Choi, J. Mechanistic Insight into Surface Defect Control in Perovskite Nanocrystals: Ligands Terminate the Valence Transition from Pb^{2+} to Metallic Pb^0. *The Journal of Physical Chemistry Letters* **2019**, *10*, 4222–4228.

(77) Huang, H.; Raith, J.; Kershaw, S. V.; Kalytchuk, S.; Tomanec, O.; Jing, L.; Susha, A. S.; Zboril, R.; Rogach, A. L. Growth mechanism of strongly emitting $CH_3NH_3PbBr_3$ perovskite nanocrystals with a tunable bandgap. *Nature Communications* **2017**, *8*, 1–8.

(78) Ding, H.; Jiang, H.; Wang, X. How organic ligands affect the phase transition and fluorescent stability of perovskite nanocrystals. *Journal of Materials Chemistry C* **2020**, *8*, 8999–9004.

(79) Zhang, Y.; Shah, T.; Deepak, F. L.; Korgel, B. A. Surface Science and Colloidal Stability of Double-Perovskite $Cs_2AgBiBr_6$ Nanocrystals and Their Superlattices. *Chemistry of Materials* **2019**, *31*, 7962–7969.

(80) Wong, E. M.; Hoertz, P. G.; Liang, C. J.; Shi, B.-M.; Meyer, G. J.; Searson, P. C. Influence of Organic Capping Ligands on the Growth Kinetics of ZnO Nanoparticles. *Langmuir* **2001**, *17*, 8362–8367.

(81) Xu, L.-J.; Worku, M.; He, Q.; Lin, H.; Zhou, C.; Chen, B.; Lin, X.; Xin, Y.; Ma, B. Ligand-Mediated Release of Halides for Color Tuning of Perovskite Nanocrystals with Enhanced Stability. *The Journal of Physical Chemistry Letters* **2019**, *10*, 5836–5840.

(82) Xiao, H.; Wei, Y.; Dang, P.; Liang, S.; Cheng, Z.; Li, G.; Lin, J. Polymer ligands induced remarkable spectral shifts in all-inorganic lead halide perovskite nanocrystals. *Journal of Materials Chemistry C* **2020**, *8*, 9968–9974.

(83) Yazdani, N.; Volk, S.; Yarema, O.; Yarema, M.; Wood, V. Size, Ligand, and Defect-Dependent Electron–Phonon Coupling in Chalcogenide and Perovskite Nanocrystals and Its Impact on Luminescence Line Widths. *ACS Photonics* **2020**, *7*, 1088–1095.

(84) Azzaro, M. S.; Dodin, A.; Zhang, D. Y.; Willard, A. P.; Roberts, S. T. Exciton-Delocalizing Ligands Can Speed Up Energy Migration in Nanocrystal Solids. *Nano Letters* **2018**, *18*, 3259–3270.

(85) Wang, X.; Liu, S.; Zhao, B.; Liu, H.; Li, X. Study on the Ultrafast Process of Perovskite Nanoparticles Modified by Different Alkyl Chains. *Langmuir* **2020**, *36*, 1507–1514.

(86) Shyamal, S.; Dutta, S. K.; Das, T.; Sen, S.; Chakraborty, S.; Pradhan, N. Facets and Defects in Perovskite Nanocrystals for Photocatalytic CO_2 Reduction. *The Journal of Physical Chemistry Letters* **2020**, *11*, 3608–3614.

(87) Shyamal, S.; Pradhan, N. Halide Perovskite Nanocrystal Photocatalysts for CO_2 Reduction: Successes and Challenges. *The Journal of Physical Chemistry Letters* **2020**, *11*, 6921–6934.

(88) Whitfield, P. S.; Herron, N.; Guise, W. E.; Page, K.; Cheng, Y. Q.; Milas, I.; Crawford, M. K. Structures, Phase Transitions and Tricritical Behavior of the Hybrid Perovskite Methyl Ammonium Lead Iodide. *Scientific Reports* **2016**, *6*, 35685.

(89) Aharon, S.; Wierzbowska, M.; Etgar, L. The Effect of the Alkylammonium Ligand's Length on Organic–Inorganic Perovskite Nanoparticles. *ACS Energy Letters* **2018**, *3*, 1387–1393.

(90) Kumar, S.; Jagielski, J.; Marcato, T.; Solari, S. F.; Shih, C.-J. Understanding the Ligand Effects on Photophysical, Optical, and Electroluminescent Characteristics of Hybrid Lead Halide Perovskite Nanocrystal Solids. *The Journal of Physical Chemistry Letters* **2019**, *10*, 7560–7567.

(91) Udayabhaskararao, T.; Houben, L.; Cohen, H.; Menahem, M.; Pinkas, I.; Avram, L.; Wolf, T.; Teitelboim, A.; Leskes, M.; Yaffe, O.; Oron, D.; Kazes, M. A Mechanistic Study of Phase Transformation in Perovskite Nanocrystals Driven by Ligand Passivation. *Chemistry of Materials* **2018**, *30*, 84–93.

(92) Almeida, G.; Goldoni, L.; Akkerman, Q.; Dang, Z.; Khan, A. H.; Marras, S.; Moreels, I.; Manna, L. Role of Acid–Base Equilibria in the Size, Shape, and Phase Control of Cesium Lead Bromide Nanocrystals. *ACS Nano* **2018**, *12*, 1704–1711.

(93) Khan, J.; Zhang, X.; Yuan, J.; Wang, Y.; Shi, G.; Patterson, R.; Shi, J.; Ling, X.; Hu, L.; Wu, T.; Dai, S.; Ma, W. Tuning the Surface-Passivating Ligand Anchoring Position Enables Phase Robustness in $CsPbI_3$ Perovskite Quantum Dot Solar Cells. *ACS Energy Letters* **2020**, *5*, 3322–3329.

(94) Hens, Z.; Martins, J. C. A Solution NMR Toolbox for Characterizing the Surface Chemistry of Colloidal Nanocrystals. *Chemistry of Materials* **2013**, *25*, 1211–1221.

(95) Grisorio, R.; Fanizza, E.; Allegretta, I.; Altamura, D.; Striccoli, M.; Terzano, R.; Giannini, C.; Vergaro, V.; Ciccarella, G.; Margiotta, N.; Paolo Suranna, G. Insights into the role of the lead/surfactant ratio in the formation and passivation of cesium lead bromide perovskite nanocrystals. *Nanoscale* **2020**, *12*, 623–637.

(96) Grisorio, R.; Clemente, M. E. D.; Fanizza, E.; Allegretta, I.; Altamura, D.; Striccoli, M.; Terzano, R.; Giannini, C.; Irimia-Vladu, M.; Paolo Suranna, G. Exploring the surface chemistry of cesium lead halide perovskite nanocrystals. *Nanoscale* **2019**, *11*, 986–999.

(97) Haw, J. F. *In-Situ Spectroscopy in Heterogeneous Catalysis*; John Wiley & Sons, Ltd, 2002; pp 53–85.

(98) Qiao, W.-C.; Liang, J.; Dong, W.; Ma, K.; Wang, X. L.; Yao, Y.-F. Illumination-Induced Changes in Methylammonium Lead Bromine Perovskites. An In Situ ^{2}H NMR Study. *The Journal of Physical Chemistry C* **2021**, *125*, 9908–9915.

(99) Mashiach, R.; Weissman, H.; Avram, L.; Houben, L.; Brontvein, O.; Lavie, A.; Arunachalam, V.; Leskes, M.; Rybtchinski, B.; Bar-Shir, A. In situ NMR reveals real-time nanocrystal growth evolution via monomer-attachment or particle-coalescence. *Nature Communications* **2021**, *12*, 229.

(100) Zhou, Y.; Sternlicht, H.; Padture, N. P. Transmission Electron Microscopy of Halide Perovskite Materials and Devices. *Joule* **2019**, *3*, 641–661.

(101) Ran, J.; Dyck, O.; Wang, X.; Yang, B.; Geohegan, D. B.; Xiao, K. Electron-Beam-Related Studies of Halide Perovskites: Challenges and Opportunities. *Advanced Energy Materials* **2020**, *10*, 1903191.

(102) Panthani, M. G.; Hessel, C. M.; Reid, D.; Casillas, G.; José-Yacamán, M.; Korgel, B. A. Graphene-Supported High-Resolution TEM and STEM Imaging of Silicon Nanocrystals and their Capping Ligands. *The Journal of Physical Chemistry C* **2012**, *116*, 22463–22468.

(103) Dang, Z.; Shamsi, J.; Palazon, F.; Imran, M.; Akkerman, Q. A.; Park, S.; Bertoni, G.; Prato, M.; Brescia, R.; Manna, L. In Situ Transmission Electron Microscopy Study of Electron Beam-Induced Transformations in Colloidal Cesium Lead Halide Perovskite Nanocrystals. *ACS Nano* **2017**, *11*, 2124–2132.

(104) Chen, S.; Gao, P. Challenges, myths, and opportunities of electron microscopy on halide perovskites. *Journal of Applied Physics* **2020**, *128*, 010901.

(105) VandenBussche, E. J.; Clark, C. P.; Holmes, R. J.; Flannigan, D. J. Mitigating Damage to Hybrid Perovskites Using Pulsed-Beam TEM. *ACS Omega* **2020**, *5*, 31867–31871.

(106) Wang, T.; Yang, Z.; Yang, L.; Yu, X.; Sun, L.; Qiu, J.; Zhou, D.; Lu, W.; Yu, S. F.; Lin, Y.; Xu, X. Atomic-Scale Insights into the Dynamics of Growth and Degradation of All-Inorganic Perovskite Nanocrystals. *The Journal of Physical Chemistry Letters* **2020**, *11*, 4618–4624.

(107) Zhang, D.; Zhu, Y.; Liu, L.; Ying, X.; Hsiung, C.-E.; Sougrat, R.; Li, K.; Han, Y. Atomic-resolution transmission electron microscopy of electron beam–sensitive crystalline materials. *Science* **2018**, *359*, 675–679.

(108) Zhu, C.; Liang, S.; Song, E.; Zhou, Y.; Wang, W.; Shan, F.; Shi, Y.; Hao, C.; Yin, K.; Zhang, T.; Liu, J.; Zheng, H.; Sun, L. In-situ liquid cell transmission electron microscopy investigation on oriented attachment of gold nanoparticles. *Nature Communications* **2018**, *9*, 421.

(109) Qin, F.; Wang, Z.; Wang, Z. L. Anomalous Growth and Coalescence Dynamics of Hybrid Perovskite Nanoparticles Observed by Liquid-Cell Transmission Electron Microscopy. *ACS Nano* **2016**, *10*, 9787–9793.

(110) Woehl, T. J. Metal Nanocrystal Formation during Liquid Phase Transmission Electron Microscopy: Thermodynamics and Kinetics of Precursor Conversion, Nucleation, and Growth. *Chemistry of Materials* **2020**, *32*, 7569–7581.

(111) Arramel, et al. Molecular functionalization of all-inorganic perovskite $CsPbBr_3$ thin films. *Journal of Materials Chemistry C* **2020**, *8*, 12587–12598.

(112) Clark, P. C. J. et al. The passivating effect of cadmium in PbS/CdS colloidal quantum dots probed by nm-scale depth profiling. *Nanoscale* **2017**, *9*, 6056–6067.

(113) Clark, P. C. J.; Flavell, W. R. Surface and Interface Chemistry in Colloidal Quantum Dots for Solar Applications Studied by X-Ray Photoelectron Spectroscopy. *The Chemical Record* **2019**, *19*, 1233–1243.

(114) Ding, H.; Li, B.; Zareen, S.; Li, G.; Tu, Y.; Zhang, D.; Cao, X.; Xu, Q.; Yang, S.; Tait, S. L.; Zhu, J. In Situ Investigations of Al/Perovskite Interfacial Structures. *ACS Applied Materials & Interfaces* **2020**, *12*, 28861–28868.

(115) Sadighian, J. C.; Wilson, K. S.; Crawford, M. L.; Wong, C. Y. Evolving Stark Effect During Growth of Perovskite Nanocrystals Measured Using Transient Absorption. *Frontiers in Chemistry* **2020**, *8*, 897.

(116) Sutter-Fella, C. M. The Value of Watching How Materials Grow: A Multimodal Case Study on Halide Perovskites. *Advanced Energy Materials* **2021**, *11*, 2003534.

(117) Song, T.-B.; Yuan, Z.; Mori, M.; Motiwala, F.; Segev, G.; Masquelier, E.; Stan, C. V.; Slack, J. L.; Tamura, N.; Sutter-Fella, C. M. Revealing the Dynamics of Hybrid Metal Halide Perovskite Formation via Multimodal In Situ Probes. *Advanced Functional Materials* **2020**, *30*, 1908337.

(118) Darmawan, Y. A.; Yamauchi, M.; Masuo, S. In Situ Observation of a Photodegradation-Induced Blueshift in Perovskite Nanocrystals Using Single-Particle Spectroscopy Combined with Atomic Force Microscopy. *The Journal of Physical Chemistry C* **2020**, *124*, 18770–18776.

(119) Masuo, S.; Kanetaka, K.; Sato, R.; Teranishi, T. Direct Observation of Multiphoton Emission Enhancement from a Single Quantum Dot Using AFM Manipulation of a Cubic Gold Nanoparticle. *ACS Photonics* **2016**, *3*, 109–116.

(120) Weber, M.; Westendorf, S.; Märker, B.; Braun, K.; Scheele, M. Opportunities and challenges for electrochemistry in studying the electronic structure of nanocrystals. *Physical Chemistry Chemical Physics* **2019**, *21*, 8992–9001.

(121) Huang, H.; Feil, M. W.; Fuchs, S.; Debnath, T.; Richter, A. F.; Tong, Y.; Wu, L.; Wang, Y.; Döblinger, M.; Nickel, B. Growth of Perovskite $CsPbBr_3$ Nanocrystals and Their Formed Superstructures Revealed by In Situ Spectroscopy. *Chemistry of Materials* **2020**, *32*, 8877–8884.

(122) Lai, R.; Wu, K. Picosecond electron trapping limits the emissivity of $CsPbCl_3$ perovskite nanocrystals. *The Journal of Chemical Physics* **2019**, *151*, 194701.

(123) Xiao, M.; Lu, T.; Lin, T.; Andre, J. S.; Chen, Z. Understanding Molecular Structures of Buried Interfaces in Halide Perovskite Photovoltaic Devices Nondestructively with Sub-Monolayer Sensitivity Using Sum Frequency Generation Vibrational Spectroscopy. *Advanced Energy Materials* **2020**, *10*, 1903053.

(124) Roke, S.; Gonella, G. Nonlinear Light Scattering and Spectroscopy of Particles and Droplets in Liquids. *Annual Review of Physical Chemistry* **2012**, *63*, 353–378.

(125) Wang, H.-F.; Velarde, L.; Gan, W.; Fu, L. Quantitative Sum-Frequency Generation Vibrational Spectroscopy of Molecular Surfaces and Interfaces: Lineshape, Polarization, and Orientation. *Annual Review of Physical Chemistry* **2015**, *66*, 189–216.

(126) Wei, X.; Hong, S.-C.; Lvovsky, A. I.; Held, H.; Shen, Y. R. Evaluation of Surface vs Bulk Contributions in Sum-Frequency Vibrational Spectroscopy Using Reflection and Transmission Geometries. *The Journal of Physical Chemistry B* **2000**, *104*, 3349–3354.

(127) Shen, Y. R. Basic Theory of Surface Sum-Frequency Generation. *The Journal of Physical Chemistry C* **2012**, *116*, 15505–15509.

(128) Sung, W.; Müller, C.; Hietzschold, S.; Lovrinčić, R.; Gallop, N. P.; Bakulin, A. A.; Nihonyanagi, S.; Tahara, T. Preferred orientations of organic cations at lead-halide perovskite interfaces revealed using vibrational sum-frequency spectroscopy. *Materials Horizons* **2020**, *7*, 1348–1357.

(129) Watson, B. R.; Ma, Y.-Z.; Cahill, J. F.; Doughty, B.; Calhoun, T. R. Probing ligand removal and ordering at quantum dot surfaces using vibrational sum frequency generation spectroscopy. *Journal of Colloid and Interface Science* **2019**, *537*, 389–395.

(130) Watson, B. R.; Doughty, B.; Calhoun, T. R. Energetics at the Surface: Direct Optical Mapping of Core and Surface Electronic Structure in CdSe Quantum Dots Using Broadband Electronic Sum Frequency Generation Microspectroscopy. *Nano Letters* **2019**, *19*, 6157–6165.

(131) Han, H. L.; Horowitz, Y.; Somorjai, G. A. In *Encyclopedia of Interfacial Chemistry*; Wandelt, K., Ed.; Elsevier: Oxford, 2018; pp 1–12.

(132) Liu, W.-T.; Shen, Y. R. In situ sum-frequency vibrational spectroscopy of electrochemical interfaces with surface plasmon resonance. *Proceedings of the National Academy of Sciences* **2014**, *111*, 1293–1297.

(133) Cotton, D. E.; Roberts, S. T. Sensitivity of sum frequency generation experimental conditions to thin film interference effects. *The Journal of Chemical Physics* **2021**, *154*, 114704.

(134) Berera, R.; Grondelle, R. v.; Kennis, J. T. M. Ultrafast transient absorption spectroscopy: principles and application to photosynthetic systems. *Photosynthesis Research* **2009**, *101*, 105–118.

(135) Wilson, K. S.; Wong, C. Y. Single-shot transient absorption spectroscopy with a 45 ps pump-probe time delay range. *Optics Letters* **2018**, *43*, 371–374.

(136) Wilson, K. S.; Mapile, A. N.; Wong, C. Y. Broadband single-shot transient absorption spectroscopy. *Optics Express* **2020**, *28*, 11339–11355.

(137) Qu, L.; Yu, W. W.; Peng, X. In Situ Observation of the Nucleation and Growth of CdSe Nanocrystals. *Nano Letters* **2004**, *4*, 465–469.

(138) Abécassis, B.; Testard, F.; Spalla, O.; Barboux, P. Probing in situ the Nucleation and Growth of Gold Nanoparticles by Small-Angle X-ray Scattering. *Nano Letters* **2007**, *7*, 1723–1727.

(139) Yoon, S. J.; Draguta, S.; Manser, J. S.; Sharia, O.; Schneider, W. F.; Kuno, M.; Kamat, P. V. Tracking Iodide and Bromide Ion Segregation in Mixed Halide Lead Perovskites during Photoirradiation. *ACS Energy Letters* **2016**, *1*, 290–296.

(140) Yoon, S. J.; Kuno, M.; Kamat, P. V. Shift Happens. How Halide Ion Defects Influence Photoinduced Segregation in Mixed Halide Perovskites. *ACS Energy Letters* **2017**, *2*, 1507–1514.

(141) Samu, G. F.; Janáky, C.; Kamat, P. V. A Victim of Halide Ion Segregation. How Light Soaking Affects Solar Cell Performance of Mixed Halide Lead Perovskites. *ACS Energy Letters* **2017**, *2*, 1860–1861.

(142) Murray, C. B.; Norris, D. J.; Bawendi, M. G. Synthesis and characterization of nearly monodisperse CdE (E = sulfur, selenium, tellurium) semiconductor nanocrystallites. *Journal of the American Chemical Society* **1993**, *115*, 8706–8715.

(143) Stamplecoskie, K. G.; Manser, J. S.; Kamat, P. V. Dual nature of the excited state in organic–inorganic lead halide perovskites. *Energy & Environmental Science* **2014**, *8*, 208–215.

(144) Thanh, N. T. K.; Maclean, N.; Mahiddine, S. Mechanisms of Nucleation and Growth of Nanoparticles in Solution. *Chemical Reviews* **2014**, *114*, 7610–7630.

(145) Peng, X.; Wickham, J.; Alivisatos, A. P. Kinetics of II-VI and III-V Colloidal Semiconductor Nanocrystal Growth: "Focusing" of Size Distributions. *Journal of the American Chemical Society* **1998**, *120*, 5343–5344.

(146) Yin, Y.; Alivisatos, A. P. Colloidal nanocrystal synthesis and the organic–inorganic interface. *Nature* **2005**, *437*, 664–670.

(147) Sugimoto, T. Underlying mechanisms in size control of uniform nanoparticles. *Journal of Colloid and Interface Science* **2007**, *309*, 106–118.

(148) Lu, Y. H.; Lin, W. H.; Yang, C. Y.; Chiu, Y. H.; Pu, Y. C.; Lee, M. H.; Tseng, Y. C.; Hsu, Y. J. A facile green antisolvent approach to Cu_{2+}-doped ZnO nanocrystals with visible-light-responsive photoactivities. *Nanoscale* **2014**, *6*, 8796–8803.

(149) Akkerman, Q. A.; Motti, S. G.; Srimath Kandada, A. R.; Mosconi, E.; D'Innocenzo, V.; Bertoni, G.; Marras, S.; Kamino, B. A.; Miranda, L.; De Angelis, F.; Petrozza, A.; Prato, M.; Manna, L. Solution Synthesis Approach to Colloidal Cesium Lead Halide Perovskite Nanoplatelets with Monolayer-Level Thickness Control. *Journal of the American Chemical Society* **2016**, *138*, 1010–1016.

(150) Seth, S.; Samanta, A. A Facile Methodology for Engineering the Morphology of $CsPbX_3$ Perovskite Nanocrystals under Ambient Condition. *Scientific Reports* **2016**, *6*, 37693.

(151) Pu, Y.; Cai, F.; Wang, D.; Wang, J.-X.; Chen, J.-F. Colloidal Synthesis of Semiconductor Quantum Dots toward Large-Scale Production: A Review. *Industrial & Engineering Chemistry Research* **2018**, *57*, 1790–1802.

(152) Tong, Y.; Bladt, E.; Aygüler, M. F.; Manzi, A.; Milowska, K. Z.; Hintermayr, V. A.; Docampo, P.; Bals, S.; Urban, A. S.; Polavarapu, L.; Feldmann, J. Highly Luminescent Cesium Lead Halide Perovskite Nanocrystals with Tunable Composition and Thickness by Ultrasonication. *Angewandte Chemie International Edition* **2016**, *55*, 13887–13892.

(153) Li, F.; Cao, L.; Shi, S.; Gao, H.; Song, L.; Geng, C.; Bi, W.; Xu, S. Controlled Growth of $CH_3NH_3PbBr_3$ Perovskite Nanocrystals via a Water–Oil Interfacial Synthesis Method. *Angewandte Chemie International Edition* **2019**, *58*, 17631–17635.

(154) Ostwald, W. Über die vermeintliche Isomerie des roten und gelben Quecksilberoxyds und die Oberflächenspannung fester Körper. *Zeitschrift für Physikalische Chemie* **1900**, *34U*, 495–503.

(155) Lifshitz, I. M.; Slyozov, V. V. The kinetics of precipitation from supersaturated solid solutions. *Journal of Physics and Chemistry of Solids* **1961**, *19*, 35–50.

(156) Wagner, C. Theorie der Alterung von Niederschlägen durch Umlösen (Ostwald-Reifung). *Zeitschrift für Elektrochemie, Berichte der Bunsengesellschaft für physikalische Chemie* **1961**, *65*, 581–591.

(157) Voorhees, P. W. The theory of Ostwald ripening. *Journal of Statistical Physics* **1985**, *38*, 231–252.

(158) Pradhan, N.; Reifsnyder, D.; Xie, R.; Aldana, J.; Peng, X. Surface Ligand Dynamics in Growth of Nanocrystals. *Journal of the American Chemical Society* **2007**, *129*, 9500–9509.

(159) Xia, Y.; Xiong, Y.; Lim, B.; Skrabalak, S. E. Shape-Controlled Synthesis of Metal Nanocrystals: Simple Chemistry Meets Complex Physics? *Angewandte Chemie International Edition* **2009**, *48*, 60–103.

(160) Bealing, C. R.; Baumgardner, W. J.; Choi, J. J.; Hanrath, T.; Hennig, R. G. Predicting Nanocrystal Shape through Consideration of Surface-Ligand Interactions. *ACS Nano* **2012**, *6*, 2118–2127.

(161) Xia, X.; Xie, S.; Liu, M.; Peng, H.-C.; Lu, N.; Wang, J.; Kim, M. J.; Xia, Y. On the role of surface diffusion in determining the shape or morphology of noble-metal nanocrystals. *Proceedings of the National Academy of Sciences* **2013**, *110*, 6669–6673.

(162) Yang, D.; Li, X.; Zeng, H. Surface Chemistry of All Inorganic Halide Perovskite Nanocrystals: Passivation Mechanism and Stability. *Advanced Materials Interfaces* **2018**, *5*, 1701662.

(163) Steckel, J. S.; Yen, B. K. H.; Oertel, D. C.; Bawendi, M. G. On the Mechanism of Lead Chalcogenide Nanocrystal Formation. *Journal of the American Chemical Society* **2006**, *128*, 13032–13033.

(164) Liu, H.; Owen, J. S.; Alivisatos, A. P. Mechanistic Study of Precursor Evolution in Colloidal Group II–VI Semiconductor Nanocrystal Synthesis. *Journal of the American Chemical Society* **2007**, *129*, 305–312.

(165) Yu, K.; Hu, M. Z.; Wang, R.; Piolet, M. L.; Frotey, M.; Zaman, M. B.; Wu, X.; Leek, D. M.; Tao, Y.; Wilkinson, D.; Li, C. Thermodynamic Equilibrium-Driven Formation of Single-Sized Nanocrystals: Reaction Media Tuning CdSe Magic-Sized versus Regular Quantum Dots. *The Journal of Physical Chemistry C* **2010**, *114*, 3329–3339.

(166) Owen, J. S.; Chan, E. M.; Liu, H.; Alivisatos, A. P. Precursor Conversion Kinetics and the Nucleation of Cadmium Selenide Nanocrystals. *Journal of the American Chemical Society* **2010**, *132*, 18206–18213.

(167) Yu, K. CdSe Magic-Sized Nuclei, Magic-Sized Nanoclusters and Regular Nanocrystals: Monomer Effects on Nucleation and Growth. *Advanced Materials* **2012**, *24*, 1123–1132.

(168) De Nolf, K.; Capek, R. K.; Abe, S.; Sluydts, M.; Jang, Y.; Martins, J. C.; Cottenier, S.; Lifshitz, E.; Hens, Z. Controlling the Size of Hot Injection Made Nanocrystals by Manipulating the Diffusion Coefficient of the Solute. *Journal of the American Chemical Society* **2015**, *137*, 2495–2505.

(169) Li, J.; Wang, H.; Lin, L.; Fang, Q.; Peng, X. Quantitative Identification of Basic Growth Channels for Formation of Monodisperse Nanocrystals. *Journal of the American Chemical Society* **2018**, *140*, 5474–5484.

(170) Turkevich, J.; Stevenson, P. C.; Hillier, J. A study of the nucleation and growth processes in the synthesis of colloidal gold. *Discussions of the Faraday Society* **1951**, *11*, 55–75.

(171) Sugimoto, T.; Shiba, F.; Sekiguchi, T.; Itoh, H. Spontaneous nucleation of monodisperse silver halide particles from homogeneous gelatin solution I: silver chloride. *Colloids and Surfaces A: Physicochemical and Engineering Aspects* **2000**, *164*, 183–203.

(172) Sugimoto, T.; Shiba, F. Spontaneous nucleation of monodisperse silver halide particles from homogeneous gelatin solution II: silver bromide. *Colloids and Surfaces A: Physicochemical and Engineering Aspects* **2000**, *164*, 205–215.

(173) Wang, J.; Boelens, H. F. M.; Thathagar, M. B.; Rothenberg, G. In Situ Spectroscopic Analysis of Nanocluster Formation. *ChemPhysChem* **2004**, *5*, 93–98.

(174) Li, D.; Nielsen, M. H.; Lee, J. R. I.; Frandsen, C.; Banfield, J. F.; Yoreo, J. J. D. Direction-Specific Interactions Control Crystal Growth by Oriented Attachment. *Science* **2012**, *336*, 1014–1018.

(175) Kalyuzhny, G.; Murray, R. W. Ligand Effects on Optical Properties of CdSe Nanocrystals. *The Journal of Physical Chemistry B* **2005**, *109*, 7012–7021.

(176) Luo, B.; Pu, Y.-C.; Lindley, S. A.; Yang, Y.; Lu, L.; Li, Y.; Li, X.; Zhang, J. Z. Organolead Halide Perovskite Nanocrystals: Branched Capping Ligands Control Crystal Size and Stability. *Angewandte Chemie International Edition* **2016**, *55*, 8864–8868.

(177) Zheng, X.; Hou, Y.; Sun, H.-T.; Mohammed, O. F.; Sargent, E. H.; Bakr, O. M. Reducing Defects in Halide Perovskite Nanocrystals for Light-Emitting Applications. *The Journal of Physical Chemistry Letters* **2019**, *10*, 2629–2640.

(178) Huang, H.; Xue, Q.; Chen, B.; Xiong, Y.; Schneider, J.; Zhi, C.; Zhong, H.; Rogach, A. L. Top-Down Fabrication of Stable Methylammonium Lead Halide Perovskite Nanocrystals by Employing a Mixture of Ligands as Coordinating Solvents. *Angewandte Chemie International Edition* **2017**, *56*, 9571–9576.

(179) Tong, Y.; Ehrat, F.; Vanderlinden, W.; Cardenas-Daw, C.; Stolarczyk, J. K.; Polavarapu, L.; Urban, A. S. Dilution-Induced Formation of Hybrid Perovskite Nanoplatelets. *ACS Nano* **2016**, *10*, 10936–10944.

(180) Klein-Kedem, N.; Cahen, D.; Hodes, G. Effects of Light and Electron Beam Irradiation on Halide Perovskites and Their Solar Cells. *Accounts of Chemical Research* **2016**, *49*, 347–354.

(181) Dang, Z.; Shamsi, J.; Akkerman, Q. A.; Imran, M.; Bertoni, G.; Brescia, R.; Manna, L. Low-Temperature Electron Beam-Induced Transformations of Cesium Lead Halide Perovskite Nanocrystals. *ACS Omega* **2017**, *2*, 5660–5665.

(182) Lignos, I.; Stavrakis, S.; Nedelcu, G.; Protesescu, L.; deMello, A. J.; Kovalenko, M. V. Synthesis of Cesium Lead Halide Perovskite Nanocrystals in a Droplet-Based Microfluidic Platform: Fast Parametric Space Mapping. *Nano Letters* **2016**, *16*, 1869–1877.

(183) Lignos, I.; Maceiczyk, R.; deMello, A. J. Microfluidic Technology: Uncovering the Mechanisms of Nanocrystal Nucleation and Growth. *Accounts of Chemical Research* **2017**, *50*, 1248–1257.

(184) Maceiczyk, R. M.; Dümbgen, K.; Lignos, I.; Protesescu, L.; Kovalenko, M. V.; deMello, A. J. Microfluidic Reactors Provide Preparative and Mechanistic Insights into the Synthesis of Formamidinium Lead Halide Perovskite Nanocrystals. *Chemistry of Materials* **2017**, *29*, 8433–8439.

(185) Reiss, H. The Growth of Uniform Colloidal Dispersions. *The Journal of Chemical Physics* **1951**, *19*, 482–487.

(186) Chu, D. B. K.; Owen, J. S.; Peters, B. Nucleation and Growth Kinetics from LaMer Burst Data. *The Journal of Physical Chemistry A* **2017**, *121*, 7511–7517.

(187) Sadighian, J. C.; Crawford, M. L.; Wong, C. Y. Rapid sampling during synthesis of lead halide perovskite nanocrystals for spectroscopic measurement. *MRS Advances* **2019**, *4*, 1957–1964.

(188) Chiba, T.; Hoshi, K.; Pu, Y.-J.; Takeda, Y.; Hayashi, Y.; Ohisa, S.; Kawata, S.; Kido, J. High-Efficiency Perovskite Quantum-Dot Light-Emitting Devices by Effective Washing Process and Interfacial Energy Level Alignment. *ACS Applied Materials & Interfaces* **2017**, *9*, 18054–18060.

(189) Xiao, C.; Li, Z.; Guthrey, H.; Moseley, J.; Yang, Y.; Wozny, S.; Moutinho, H.; To, B.; Berry, J. J.; Gorman, B.; Yan, Y.; Zhu, K.; Al-Jassim, M. Mechanisms of Electron-Beam-Induced Damage in Perovskite Thin Films Revealed by Cathodoluminescence Spectroscopy. *The Journal of Physical Chemistry C* **2015**, *119*, 26904–26911.

(190) Milosavljević, A. R.; Huang, W.; Sadhu, S.; Ptasinska, S. Low-Energy Electron-Induced Transformations in Organolead Halide Perovskite. *Angewandte Chemie International Edition* **2016**, *55*, 10083–10087.

(191) Philippe, B.; Park, B.-W.; Lindblad, R.; Oscarsson, J.; Ahmadi, S.; Johansson, E. M. J.; Rensmo, H. Chemical and Electronic Structure Characterization of Lead Halide Perovskites and Stability Behavior under Different Exposures—A Photoelectron Spectroscopy Investigation. *Chemistry of Materials* **2015**, *27*, 1720–1731.

(192) Yuan, H.; Debroye, E.; Janssen, K.; Naiki, H.; Steuwe, C.; Lu, G.; Moris, M.; Orgiu, E.; Uji-i, H.; De Schryver, F.; Samorì, P.; Hofkens, J.; Roeffaers, M. Degradation of Methylammonium Lead Iodide Perovskite Structures through Light and Electron Beam Driven Ion Migration. *The Journal of Physical Chemistry Letters* **2016**, *7*, 561–566.

(193) Katari, J. E. B.; Colvin, V. L.; Alivisatos, A. P. X-ray Photoelectron Spectroscopy of CdSe Nanocrystals with Applications to Studies of the Nanocrystal Surface. *The Journal of Physical Chemistry* **1994**, *98*, 4109–4117.

(194) Wang, Z. L.; Harfenist, S. A.; Whetten, R. L.; Bentley, J.; Evans, N. D. Bundling and Interdigitation of Adsorbed Thiolate Groups in Self-Assembled Nanocrystal Superlattices. *The Journal of Physical Chemistry B* **1998**, *102*, 3068–3072.

(195) Mattoussi, H.; Cumming, A. W.; Murray, C. B.; Bawendi, M. G.; Ober, R. Properties of CdSe nanocrystal dispersions in the dilute regime: Structure and interparticle interactions. *Physical Review B* **1998**, *58*, 7850–7863.

(196) Colvin, V. L.; Alivisatos, A. P. CdSe nanocrystals with a dipole moment in the first excited state. *The Journal of Chemical Physics* **1992**, *97*, 730–733.

(197) Colvin, V. L.; Cunningham, K. L.; Alivisatos, A. P. Electric field modulation studies of optical absorption in CdSe nanocrystals: Dipolar character of the excited state. *The Journal of Chemical Physics* **1994**, *101*, 7122–7138.

(198) Klimov, V. I. Optical Nonlinearities and Ultrafast Carrier Dynamics in Semiconductor Nanocrystals. *The Journal of Physical Chemistry B* **2000**, *104*, 6112–6123.

(199) Sharma, D. K.; Hirata, S.; Biju, V.; Vacha, M. Stark Effect and Environment-Induced Modulation of Emission in Single Halide Perovskite Nanocrystals. *ACS Nano* **2019**, *13*, 624–632.

(200) Bublitz, G. U.; Boxer, S. G. STARK SPECTROSCOPY: Applications in Chemistry, Biology, and Materials Science. *Annual Review of Physical Chemistry* **1997**, *48*, 213–242.

(201) Walters, G.; Wei, M.; Voznyy, O.; Quintero-Bermudez, R.; Kiani, A.; Smilgies, D.-M.; Munir, R.; Amassian, A.; Hoogland, S.; Sargent, E. The quantum-confined Stark effect in layered hybrid perovskites mediated by orientational polarizability of confined dipoles. *Nature Communications* **2018**, *9*, 4214.

(202) Tanaka, K.; Kondo, T. Bandgap and exciton binding energies in lead-iodide-based natural quantum-well crystals. *Science and Technology of Advanced Materials* **2003**, *4*, 599–604.

(203) Queloz, V. I. E.; Bouduban, M. E. F.; García-Benito, I.; Fedorovskiy, A.; Orlandi, S.; Cavazzini, M.; Pozzi, G.; Trivedi, H.; Lupascu, D. C.; Beljonne, D.; Moser, J.-E.; Nazeeruddin, M. K.; Quarti, C.; Grancini, G. Spatial Charge Separation as the Origin of Anomalous Stark Effect in Fluorous 2D Hybrid Perovskites. *Advanced Functional Materials* **2020**, *30*, 2000228.

(204) Klimov, V. I.; McBranch, D. W. Femtosecond 1P-to-1S Electron Relaxation in Strongly Confined Semiconductor Nanocrystals. *Physical Review Letters* **1998**, *80*, 4028–4031.

(205) Guyot-Sionnest, P.; Shim, M.; Matranga, C.; Hines, M. Intraband relaxation in CdSe quantum dots. *Physical Review B* **1999**, *60*, R2181–R2184.

(206) Urayama, J.; Norris, T. B.; Singh, J.; Bhattacharya, P. Observation of Phonon Bottleneck in Quantum Dot Electronic Relaxation. *Physical Review Letters* **2001**, *86*, 4930–4933.

(207) Guyot-Sionnest, P.; Wehrenberg, B.; Yu, D. Intraband relaxation in CdSe nanocrystals and the strong influence of the surface ligands. *The Journal of Chemical Physics* **2005**, *123*, 074709.

(208) Li, Y.; Lai, R.; Luo, X.; Liu, X.; Ding, T.; Lu, X.; Wu, K. On the absence of a phonon bottleneck in strongly confined $CsPbBr_3$ perovskite nanocrystals. *Chemical Science* **2019**, *10*, 5983–5989.

(209) Mondal, N.; Samanta, A. Complete ultrafast charge carrier dynamics in photo-excited all-inorganic perovskite nanocrystals ($CsPbX_3$). *Nanoscale* **2017**, *9*, 1878–1885.

(210) Fourkas, J. T.; Dhar, L.; Nelson, K. A.; Trebino, R. Spatially encoded, single-shot ultrafast spectroscopies. *Journal of the Optical Society of America B* **1995**, *12*, 155–165.

(211) Makishima, Y.; Furukawa, N.; Ishida, A.; Takeda, J. Femtosecond Real-Time Pump-Probe Imaging Spectroscopy Implemented on a Single Shot Basis. *Japanese Journal of Applied Physics* **2006**, *45*, 5986.

(212) Wilson, K. S.; Scott, M. N.; Wong, C. Y. Single-shot transient absorption spectroscopy of an organic film. *MRS Advances* **2018**, *3*, 3453–3457.

(213) Wilson, K. S.; Scott, M. N.; Wong, C. Y. Excited state dynamics of organic semiconductors measured with shot-to-shot correction of scatter and photoluminescence. *Synthetic Metals* **2019**, *250*, 115–120.

(214) Righetto, M.; Lim, S. S.; Giovanni, D.; Lim, J. W. M.; Zhang, Q.; Ramesh, S.; Tay, Y. K. E.; Sum, T. C. Hot carriers perspective on the nature of traps in perovskites. *Nature Communications* **2020**, *11*, 2712.